



School of Physics and Astronomy בית הספר לפיזיקה ולאסטרונומיה
The Raymond and Beverly Sackler הפקולטה למדעים מדויקים
Faculty of Exact Sciences ע"ש ריימונד ובברלי סאקלר
Tel Aviv University אוניברסיטת תל אביב

Research Thesis for a Degree “Doctor of Philosophy”

COLLECTIVE LINEAR AND NONLINEAR COHERENT INTERACTION IN PLASMONIC NANOPARTICLE ARRAYS

Submitted to the Senate of Tel Aviv University by

Lior Michaeli

The work was carried out under the supervision of
Prof. Tal Ellenbogen & Prof. Haim Suchowski

January 2021

The work was carried out under the supervision of
Prof. Tal Ellenbogen & Prof. Haim Suchowski

ACKNOWLEDGEMENTS

Over the course of my PhD, I was privileged to be surrounded by supportive people, who substantially contributed to this thesis. First, I would like to express my deep and sincere gratitude to my PhD supervisors Prof. Tal Ellenbogen and Prof. Haim Suchowski.

Tal, thanks for all the wonderful years being a part of your group, during both my Master and PhD. The accurate balance between your professional guidance and advise, the freedom you gave me to learn and explore, and the friendly atmosphere have all painted this period with vivid colors. Your profound expertise in various areas, remarkable creativity to find solutions to seemingly unsolvable problems, the good advises you give even in subjects unrelated to the research, and keeping me focused towards achieving my own goals have helped my professional and personal growth and made these years of working with you very fertile and enjoyable. I especially acknowledge the unique atmosphere that you generated and preserved in the group over the years by your positive leadership, pleasurable group events and retreats, and occasional toasts. Deep Thanks.

Haim, I am very grateful for our years of working together. You believed in me from the first moment, gave me the opportunity to prove myself, and kept on encouraging me all along. I warmly thank you for your uncompromised professional guidance. Your ambitious attitude, inspirational motivation and enormously broad range of activities, have greatly inspired me over the years. Your advices and consultant have always guided me toward looking at the bigger picture, which can be a challenging task sometimes in the day-to-day life. Thanks for always being there for me in every subject varying from professional to personal.

Second, I would like to genuinely thank my past and present fellow lab mates, at the Nanoscale Electro-Optics (NEO) lab. With you I spent thousands of hours, consulted on research related and non-related issues. You are a truly special and talented group of people, which I had a great pleasure working with. Each one of you taught me a lot. Specifically, I would like to mention my colleagues which collaborated with me in research and contributed directly to this PhD thesis: Dr. Shay Keren-Zur, Dr. Ori Avayu, Ofer Doron, Dr. Mukesh Kumar Sharma, Danielle Ben Haim and Mai Tal. As well for the rest of the stars of the NEO lab: Dr. Elad Eizner, Dr. Rani Ditcovski, Sharon Karepov, Dr. Barak Gilboa, Tsafir Abir, Nadia Lapshina, Nadav Fain, Simos Sideris, Eviatar Minerbi, Dr. Cormac McDonnell, Yotam Ater, Dr. Guy Lazovski, Itay Langstadter and Nathalie Roterman.

I was fortunate of being a member also of the Femto-Nano lab. I would like to especially thank Dr. Michael Mrejen, Dr. Assaf Levanon, Hadar Greener, Uri Arieli, Eyal Bahar, Erga Lifshitz and Omri Meron.

Tel Aviv University has provided me a fruitful ground to work on and preform my research. I would like to mention specifically the staffs of the School of Physics & Astronomy, the School of Electrical Engineering and the Center of Light-Matter interaction.

Additional faculty members I acknowledge their consultation and contribution are Dr. Alon Bahabad, Dr. Yoav Lahini Dr. Alon Ron, Dr. Yakir Hadad and Prof. Ady Arie.

In addition, very valuable part of my PhD is attributed to my collaboration with Dr. Patrice Genevet. First and foremost, you are an extremely enjoyable personality. Your appreciation to good life, happiness and optimism make it fun to work with you. Second, I acknowledge our professional conversations, as it left me with many directions of future scientific thoughts. *Merci beaucoup*.

Last but certainly not least, my deepest gratitude goes to my family that have supported me all along the way. To my parents Avi and Michal, for introducing me to the fascinating world of science and nature, for nurturing my curiosity, and for the unconditional love from day one. Dad, thanks for enormous amount of knowledge and explanations you gave me on numerous scientific and technological subjects. Many thanks to my brother Prof. Tomer Michaeli and my sister Orit Michaeli for supporting me and challenging me. Tomer, a sincere thanks for over 20 years of teaching and tutoring me with endless patience, advising and supporting in numerous fronts and for paving the way and making me believe it is possible.

Above all, I would like to thank Linor, my love, for being there at every step of the way during my academic period and beyond. Linor, I was blessed with a life partner that not only shows constant love and support, but also shares the same academic discipline with me. At the beginning of my academic journey, I was fortunate to meet you and to see that pursuing my passions lead to wonderful things in unexpected directions. As time advanced, along with our exciting voyage as a couple, you were always pushing me forward professionally. This occurred by critically reviewing my research results, giving tips to improve my presentations, advising how to approach different problems, listening to my rough thoughts and most important, believing in me. Above all, I wholeheartedly thank you for the best two outcomes of my PhD, Erez and Geffen, my beloved children, the brightest light source of my life.

ABSTRACT

The last decades have witnessed enormous progress in our ability to control and shape light using two-dimensional artificial optical materials, also known as metasurfaces. These materials are typically made from arrays of either metallic or dielectric sub-wavelength nanoparticles. By judicious design of the nanoparticles' morphology, composite materials and position in the array, local control over the amplitude, phase and polarization of light can be achieved. Therefore, metasurfaces offer the possibility of miniaturizing traditional optical elements and realizing new functionalities. Furthermore, the great degree of freedom in their design provides the means to comprehensively explore a plethora of novel physical phenomena.

The optical response of a metasurface essentially stems from each individual nanoparticle's response, in addition to the interaction between all nanoparticles. In recent years, it has been shown that collective coherent interaction of the nanoparticles in the array can play an essential role in the total response, giving rise to numerous intriguing physical phenomena with great applicative potential.

In this thesis, we theoretically and experimentally explore fundamental aspects of the collective coherent interactions within arrays of metallic nanoparticles. Specifically, we focus on three novel aspects of these interactions: (i) Extension to the nonlinear optical regime. (ii) Temporal control and slow light effects. (iii) Their broadband amplitude and phase characterization.

We start by a comprehensive introduction in Chapter 1 that serves as the foundation for the original research presented in this thesis. The introduction presents the subjects of linear (section 1.1) and nonlinear (section 1.2) metasurfaces, slow light effects (section 1.3), spectral interferometry (section 1.4), and the various experimental, numerical and fabrication methods used for the presented research (section 1.5). In Chapter 2, which is the body of this article-based thesis, we present three peer-reviewed publications, each focused on different aspect of the collective interaction. In the first paper, in section 2.1, we introduce a study of the collective interactions within nanoparticle arrays in the nonlinear regime. We demonstrate a new resonant condition for enhanced nonlinear conversion that originates from coupling of nonlinear localized and distributed modes. The localized modes are associated with coherent electron oscillations at each particle, known as plasmons, while the distributed modes correspond to surface waves supported by coherent diffraction. In addition, we present a theoretical framework to model the role of the interaction on the nonlinear response of the array in general, and specifically for predicting the emergence of the demonstrated effect. Thereafter, in section 2.2, we show how collective scattering at the array may induce tunable transparency and slow light windows. Finally, in section 2.3, we present an original characterization method to dynamically and accurately obtain the spectral phase of a microscopic sample, either in reflection or

transmission. The method enables flexible illumination conditions, and therefore is particularly advantageous for characterization of metasurfaces supporting collective coherent effects. The findings and developments of this thesis will pave the way to new and exciting applications in nanophotonics.

TABLE OF CONTENTS

Acknowledgements	3
Abstract	5
List of Figures	8
List of acronyms	9
Chapter 1 Introduction	10
1.1 Optical metasurfaces	11
1.1.1 Single nanoparticle optical response.....	12
1.1.2 Collective array response	17
1.2 Nonlinear metasurfaces.....	23
1.2.1 Quadratic nonlinear interactions.....	24
1.2.2 Nonlinear plasmonic metasurfaces	26
1.3 Slow light.....	30
1.4 Spectral interferometry	32
1.4.1 Common path interferometry.....	34
1.5 Methods.....	35
1.5.1 Experimental methods	35
1.5.2 Numerical simulations	36
1.5.3 Fabrication techniques	40
Chapter 2 Published Manuscripts	41
2.1 Nonlinear Surface Lattice Resonance in Plasmonic Nanoparticle Arrays	43
2.2 Near-Infrared Tunable Surface Lattice Induced Transparency in a Plasmonic Metasurface	51
2.3 Spectral Interferometric Microscopy for Fast and Broadband Phase Characterization	64
Chapter 3 Summary and Outlook.....	84
List of Publications.....	88
References	89
תקציר	102

LIST OF FIGURES

Figure 1.1 Resonance behavior of plasmonic nanoparticles.	14
Figure 1.2 Typical trend of the array's structural factor.	22
Figure 1.3 Generation and far-field emission of SH in symmetric vs. asymmetric nanoparticles	29
Figure 1.4 Michelson interferometer.....	34
Figure 1.5 Spectroscopy microscope setup used throughout this thesis.....	35
Figure 1.6 Typical FDTD simulation configuration of infinite plasmonic nanoparticle array.	39
Figure 1.7 Metasurface fabrication.....	40

LIST OF ACRONYMS

CDA	Coupled dipole approximation
DFG	Difference-frequency generation
FDTD	Finite-difference time-domain
FF	Fundamental frequency
IS	Imaging spectrometer
ITO	Indium-Tin oxide
LSP	Localized surface plasmon
LSPR	Localized surface plasmon resonance
NL-SLR	Nonlinear surface lattice resonance
OPO	Optical parametric oscillator
OR	Optical rectification
PMMA	Polymethyl methacrylate
RA	Rayleigh anomaly
SFG	Sum-frequency generation
SH	Second harmonic
SHG	Second-harmonic generation
SLR	Surface lattice resonance
SRR	Split-ring resonator
TWM	Three-wave mixing

Chapter 1 **INTRODUCTION**

1.1 Optical metasurfaces

Over the past couple of decades, there have been immense advancements in the ability to control light using two-dimensional optical materials, called metasurfaces. These are optically thin structured materials made from subwavelength nanostructures, also referred to as meta-atoms, which allow control over the properties of light interacting with them. Metasurfaces enable the manipulation of waves in the optical far field and can be used as optical elements for beam shaping and holography. Moreover, metasurfaces also enable the control of light in the intermediate and near-field zones. By tuning the propagation of waves in the intermediate regime, also known as the Fresnel zone, it is possible, for example, to focus beams or engineer desired point-spread functions. At shorter distances, at which the behavior of light is governed by its near-field characteristics, judicious manipulation of the energy distribution can be beneficial for various processes, such as nonlinear generation of new frequencies [1–6], surface-enhanced Raman scattering [7–9], enhancement of Purcell factors [10–12], and enhancement of the chirality of molecules [13–15].

Metasurfaces can be used to efficiently and locally control the amplitude, phase and polarization of transmitted and reflected light. Therefore, they offer the possibility of miniaturizing traditional optical elements and realizing new functionalities. Over the past two decades, a wide variety of optical elements have already been realized by using metasurfaces, including wave plates [16,17], polarization switches [18,19], holograms [20,21], diffractive gratings [22,23], wavelength-selective surfaces [24], and lenses [25–27]. Along with their applicative potential, metasurfaces have been shown to support intriguing physical phenomena. Some examples include generation of hybrid light-matter states [28,29], electron wave function tunneling [30,31], interaction with single molecules [32,33], negative refraction [34] and room temperature Bose-Einstein condensation [35]. Moreover, thanks to the great flexibility in design and control over their optical and physical properties, metasurfaces provide a testbed for exploration of fundamental physical phenomena, which appear in completely different physical systems. Specifically, analogies between the photonic nature of metasurfaces and electronic states in condensed matter, have been extensively studied. Some of these analogies, for example, concern with photonic (electronic) band structures and band gaps [36–38], Anderson localization [39,40], topological states [36,41] and spin-orbit coupling [42].

Numerous types of metasurfaces have been studied, spanning from metasurfaces composed of either metallic or high-index dielectric planar assemblies of nanoparticles to metasurfaces with designs based on holes in metallic or dielectric films.

Focusing on metasurfaces composed of nanoparticle arrays, their net optical response depends on the individual nanoparticle response, defined by its material and morphology, the geometry

of the array and the surrounding media. Therefore, in section 1.1.1, we first describe the underlying physical mechanisms and modelling methods for the single nanoparticle optical response. We focus on the case in which the nanoparticles are metallic and thus support resonances associated with free electron oscillations, called localized surface plasmon resonances (LSPRs). These resonances lead to enhancement and localization of the electromagnetic field in the vicinity of a metallic nanoparticle, along with enhanced scattering cross sections. Second, in section 1.1.2 we present a comprehensive formalism to account for the response of a nanoparticle array, while considering mutual influence between the nanoparticles. Under this formalism, the distinct role of the individual nanoparticle response, the entire array arrangement and the properties of the applied electromagnetic field, to the net optical response become evident. Specifically, special attention is given to diffractive coupling of the nanoparticles composing the array, which may lead to new hybridized resonances, called surface lattice resonances (SLRs). While this thesis surveys several aspects of linear metasurfaces, comprehensive reviews of this subject are available [43–55].

1.1.1 Single nanoparticle optical response

The optical response of a nanoparticle to an applied electromagnetic field is essential for determining its coupling properties to other electromagnetic scatterers, its performance as a basic element for beam shaping applications and even for predicting its optical nonlinearities. To characterize this optical response, several properties are crucial as, for example, the charge density and currents distributions, near-electromagnetic-field distributions and the radiation pattern. All of these are frequency dependent and strongly connected to the polarization of the nanoparticle in response to an applied electromagnetic field. The parameter that quantifies it is the frequency-dependent polarizability $\vec{\alpha}(\omega)$, which relates the local electric field $\mathbf{E}_{loc}(\omega)$ to the induced polarization $\mathbf{P}(\omega)$ through the relation¹ $\mathbf{P}(\omega) = \vec{\alpha}(\omega)\mathbf{E}_{loc}(\omega)$. Due to the vectorial nature of the electric field and polarization, $\vec{\alpha}(\omega)$ is a 3×3 tensor. In most cases however, and specifically in the cases treated in this thesis, the off-diagonal terms of $\vec{\alpha}(\omega)$ are vanishingly

¹ We emphasize the distinct use throughout this document of α and χ , the polarizability and susceptibility, respectively. When considering the single nanoparticle optical response, we account for the polarization P of the nanoparticle, mediated by α . In contrast, in the review of nonlinear metasurfaces in section 1.2, we account for the polarization P stimulated by χ . While in atomic physics there is a clear distinction between macroscopic and microscopic descriptions of the polarization by P and p respectively, in nanophotonic systems, which are much bigger than a single atom but still smaller than the wavelength, the parametrization is more complex. Specifically, in the context of the CDA, most studies in the literature use capital P , instead of the dipole moment p . Therefore, to stay consistent with the literature our notation follows this distinction.

small. Therefore, most of the discussions will treat the polarizability as a scalar $\alpha(\omega)$, referring only to a specific diagonal term.

Several mechanisms can determine the resonant properties of $\alpha(\omega)$ in nanoparticles, depending mainly on their composing material. Two of the most common mechanisms are the collective electron oscillations in metallic nanoparticles, called localized surface plasmons (LSP), and the bound electrons mediated optical modes in dielectric nanoparticles, called Mie resonances. This thesis focuses on collective interactions within arrays composed of metallic nanoparticles supporting plasmonic resonances. Yet, it should be noted that the novel phenomena explored in this dissertation, along with the characterization method developed correspondingly, are relevant also for other resonant particles as those supporting dielectric Mie resonances. The following sub-section reviews the fundamentals of the LSPRs.

Metallic nanoparticles - localized surface plasmon resonances

Surface plasmons are coherent modes of collective oscillations of the free electrons on a metal-dielectric interface. This electron motion is associated with planar-propagating electromagnetic field with a dispersion relation of [56]:

$$k_{sp} = \frac{\omega}{c} \sqrt{\frac{\epsilon_m(\omega)\epsilon_d}{\epsilon_m(\omega) + \epsilon_d}} \quad (1.1)$$

Where k_{sp} is the magnitude of the wave vector of the surface plasmons, $\epsilon_m(\omega)$ and ϵ_d are the dielectric constants of the metal and dielectric material, respectively, ω is the angular frequency of light and c is the speed of light in vacuum. When a metal-dielectric interface is confined into small areas compared to the wavelength, such as in metallic nanostructures, the electrons' oscillations are non-propagating, and can be localized down to volumes smaller than the diffraction limit $\left(\frac{\lambda_0}{2n}\right)^3$, where λ_0 is the free-space wavelength and n is the refractive index of the surrounding medium. These localized electron oscillations, called LSP, can give rise to enhanced electromagnetic near fields and scattering amplitudes, through a resonance known as LSPR. Illustrative analysis that captures important features of the LSPR is based on a driven harmonic oscillator model [44], which results in a Lorentzian solution for the polarizability:

$$\alpha(\omega) = \frac{A_0}{\omega_0^2 - \omega^2 + i\gamma\omega} \quad (1.2)$$

Where A_0 is the amplitude, ω_0 is the resonance angular frequency and γ is the damping constant. Typical values of γ for resonances in the visible to near-infrared spectral range are in

the order of 100 THz , corresponding to a resonance width of tens of nanometers. These values are for typical metals used for plasmonic nanoparticles, such as gold, silver and aluminum. The metals are chosen such that at their desired frequency of operation they will be below the plasma frequency and with high electrical conductivity. In the driven harmonic oscillator model, a restoring force is exerted by the positive ions in the metal, which attract the electrons displaced by the electric field. The phase of the electron cloud motion relative to the phase of the electrical driving force determines the relative phase and amplitude of the scattered light. At resonance, the motion of the electrons' displacement lags with respect to the electrical driving force by a phase of $\pi/2$, whereas the full spectral width extends from in-phase motion, for frequencies lower than the resonant frequency, to out-of-phase motion, for frequencies higher than the resonant frequency (Figure 1.1). This phase trend around the resonance is essential for the coupling properties of plasmonic nanoparticles.

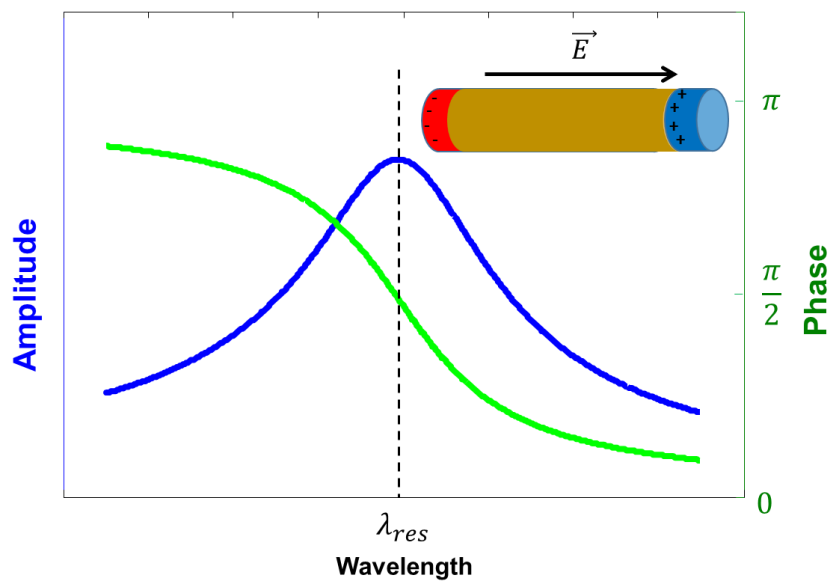


Figure 1.1. Resonance response of plasmonic nanoparticles [57]. The amplitude and phase of the free electron cloud motion vs. the wavelength are shown, based on the harmonic oscillator model. Inset: A sketch of a plasmonic nanorod whose electron cloud has been displaced. The displacement behavior of the free electrons at a nanostructure caused by an oscillating electromagnetic field can be treated as a driven damped harmonic oscillator. In the vicinity of the resonance wavelength, the phase of the electron motion relative to the driven field changes significantly.

The above description depicts the mechanism of plasmonic resonances only qualitatively; however, one must often consider the exact spectral positions of these resonances to design metasurfaces with the required interactions and coupling properties. To achieve this goal, one should choose between performing a rigorous analysis to solve the exact electromagnetic problem or perform numerical calculations using electromagnetic simulation tools or

approximate methods. An exact solution to the scattering problem exists only for spheroids [58] and ellipsoids [59], whereas in the general case, the polarizability of a nanoparticle can be found by using the quasi-static approximation. This approximation assumes that the phase of the applied field is constant over the entire particle volume; therefore, the particle size along the i^{th} axis D_i , must be much smaller than the wavelength in the surrounding medium, i.e., $D_i \ll \lambda_{med}$. An important result of the quasi-static approximation is the polarizabilities along the principal axes for an ellipsoid with semiaxes a_1 , a_2 and a_3 and volume $V = \frac{4\pi}{3} a_1 a_2 a_3$ [60]²:

$$\alpha_i^{static}(\omega) = V \frac{\epsilon(\omega) - \epsilon_{med}}{\epsilon_{med} + L_i(\epsilon(\omega) - \epsilon_{med})} \quad (1.3)$$

where $\epsilon(\omega)$ and ϵ_{med} are the dielectric constants of the particle and the surrounding medium, respectively, and the L_i , which satisfy $L_1 + L_2 + L_3 = 1$, are geometric factors given by $L_i = \frac{a_1 a_2 a_3}{2} \int_0^\infty \frac{dq}{(a_i^2 + q)f(q)}$, where $f(q) = \sqrt{(q + a_1^2)(q + a_2^2)(q + a_3^2)}$.

For a qualitative discussion of the outcomes of the polarizability expression and the conditions under which the real part of its denominator vanishes and a resonance condition is fulfilled, one can consider the simplified dielectric constant of a Drude metal below its plasma frequency ω_p with a collision angular frequency γ , $\epsilon_{Drude}(\omega) = 1 - \frac{\omega_p^2}{\omega^2 + i\gamma\omega}$. The simple Drude model cannot describe interband transition effects, which typically occur in the visible regime for noble metals.

Although the above polarizability result was formulated for small particles in the quasi-static regime, it can typically be applied for particles with dimensions on the order of tens of nanometers [56,61]. Moreover, it captures some of the most important features of plasmonic resonances, as described below. First, the different on-diagonal components of the polarizability described in Eq. (1.3) correspond to spectrally separated resonances, which depend on the semi-axes' lengths. Second, in an elongated plasmonic nanoparticle, the resonance along the direction of elongation redshifts as the corresponding semi-axes' length increases. Third, the plasmonic resonances redshift as the dielectric constant of the surrounding medium increases. The polarizability of an ellipsoid, with adequate corrections to account for dynamic depolarization and radiative damping [62], can be used to calculate the spectral

² The polarizability has volume units according to the modified SI system used throughout this thesis [167,168]. The relevant quantities are summarized in the following table:

Quantity	Symbol	Relation to SI
Electric field	E	$E^{(SI)}$
Polarization	P	$P^{(SI)}/(4\pi\epsilon)$
Polarizability	α	$\alpha^{(SI)}/(4\pi\epsilon)$

Exception of this notation is the standard SI system used in sections 1.2.1 and 1.5.2. The units' notation was chosen to be consistent with most literature on the discussed subject and to keep the presented subject elegance.

positions and line shapes of the resonances for various geometries, such as nanorods, nanoplates and nanospheres.

For larger particles, i.e. bigger than a few tens of nanometers, corrections to the static approximation are required to account for dynamical effects. These corrections for the polarizability are known as the modified long wavelength approximation [62], and take the following form:

$$\alpha_i^{MLWA}(\omega) = \frac{\alpha_i^{static}(\omega)}{1 - \frac{2}{3}ik^3\alpha_i^{static}(\omega) - \frac{k^2}{D_i}\alpha_i^{static}(\omega)} \quad (1.4)$$

The two terms at the denominator that depends on k^2 and k^3 are associated with dynamic depolarization and radiative damping, correspondingly.

An additional method to calculate the LSPR spectral location, is by modeling a nanostructure as an effective Fabry–Pérot cavity for surface plasmons. This treatment is justified when the characteristic dimension of the structure is comparable to or larger than half the effective surface plasmon wavelength, and it permits the determination of multiple resonance frequencies. For example, in a nanorod, the resonant frequencies can be derived by requiring one round trip of the guided mode to result in a phase accumulation of an integer multiple of 2π , as follows:

$$m\lambda_{eff} = 2L + 2\phi_r \quad (1.5)$$

where L is the length of the nanorod, ϕ_r is the effective length of the extended field outside the ends of the rod, that can be related to the reflection phase, and λ_{eff} is the effective plasmon wavelength, which has been shown to obey the following empirical relation [63]:

$$\lambda_{eff} = n_1 + n_2 \left(\frac{\lambda}{\lambda_p} \right) \quad (1.6)$$

where n_1 and n_2 are constants related to the geometry and the dielectric environment, respectively, and λ_p is the plasma wavelength. The conditions for LSPRs now becomes dependent on the effective wavelength λ_{eff} rather than the free-space wavelength. Typical ratios of λ/λ_{eff} are approximately 2-3 in the visible and near-infrared regimes, thus permitting deep subwavelength sizes for the nanoresonators. Using this simplified model, it is possible to gain valuable insight into the antenna responses of different metallic shapes, such as nanodisks [64–67], nanorods [63,68,69], split-ring resonators (SRRs) [70,71], and V-shaped antennas [72–74].

From the particle's polarizability, the extinction and scattering cross sections can be calculated according to [60]:

$$\sigma_{ext} = 4\pi k \Im\{\alpha\} \quad (1.7)$$

$$\sigma_{sca} = \frac{8\pi}{3} k^4 |\alpha|^2 \quad (1.8)$$

Where \Im denotes the imaginary part.

1.1.2 Collective array response

The optical response of a nanoparticle array stems from the contribution of all individual nanoparticles. However, each nanoparticle is affected not only by the applied field, but also by the scattered fields from all additional nanoparticles. Therefore, the fields scattered by each nanoparticle depend on the fields scattered on it by all the other nanoparticles, which gives rise to a system of coupled equations that need to be solved self-consistently in order to obtain each nanoparticle polarization. Though the resulting polarization is understood to stem from each nanoparticle polarizability α and the multiple scattering processes at the array, it is often convenient to ascribe an effective polarizability α_{eff} , which accounts for the presence of the array. Namely, α_{eff} describes the nanoparticle response to the applied field accounting for all interparticle interactions. The mutual interaction of the nanoparticles can lead to intriguing collective response that is substantially different from that expected by accounting for each nanoparticle individual response. Depending on the interplay between the nanoparticles' morphology, the array geometry and the properties of the applied electromagnetic field, intriguing physical phenomena can emerge. Some examples are hybridized localized-distributed modes, substantial narrowing of the spectral line-shapes [75], photonic stop bands [38], slow light generation [76], enhanced optical nonlinearity [5], and Bose-Einstein condensation at room temperature [35].

To study the optical response of a nanoparticle array, with capability for predicting and analyzing the aforementioned phenomena, the coupled dipole approximation (CDA) is often used [77,78]. This model serves to find the polarization vector \mathbf{P}_i of each of the N nanoparticles in the array ($i = 1, \dots, N$) by solving a system of $3N$ coupled equations, which accounts for the mutual influence of all nanoparticles. We denote the 3×3 polarizability tensor of the particle located at \mathbf{r}_i , by $\vec{\alpha}_{s,i}$, and express the polarization at the i^{th} location as:

$$\mathbf{P}_i = \mathbf{P}(\mathbf{r}_i) = \vec{\alpha}_{s,i} \mathbf{E}_{loc,i} \quad (1.9)$$

Where $\mathbf{E}_{loc,i} = \mathbf{E}_{loc}(\mathbf{r}_i)$ is the local electric field at \mathbf{r}_i . This field is composed of the applied field $\mathbf{E}_{app,i}$, and the retarded scattered fields from all other particles $\mathbf{E}_{sca,i}$, at that location:

$$\mathbf{E}_{loc,i} = \mathbf{E}_{app,i} + \mathbf{E}_{sca,i} = \mathbf{E}_{app,i} + \sum_{j \neq i} \vec{\mathbf{A}}_{ij} \mathbf{P}_j \quad (1.10)$$

$\vec{\mathbf{A}}_{ij}$ is the dyadic Green's function of a dipole, that describes the interaction between the i^{th} and j^{th} dipoles. For a homogeneous refractive index $n(\lambda)$ surrounding the nanoparticles, $\vec{\mathbf{A}}_{ij}$ has the following form:

$$\vec{\mathbf{A}}_{ij} = \vec{\mathbf{A}}(\mathbf{r}_i, \mathbf{r}_j) = [k^2 + \nabla \otimes \nabla] A_{0,ij} \quad , \quad A_{0,ij} = \frac{e^{ikR_{ij}}}{R_{ij}} \quad (1.11)$$

Where $k = |\mathbf{k}| = \frac{2\pi n(\lambda)}{\lambda}$ is the magnitude of the wave vector \mathbf{k} , \otimes denotes the outer product of two vectors, $\mathbf{R}_{ij} = \mathbf{r}_i - \mathbf{r}_j$ with magnitude $R_{ij} = |\mathbf{R}_{ij}|$, and $A_{0,ij}$ is the scalar Green's function that describes a spherical wave. In Cartesian coordinate system $\vec{\mathbf{A}}_{ij}$ can be explicitly expressed as [79]:

$$\vec{\mathbf{A}}_{ij} = e^{ikR_{ij}} \frac{k^2}{R_{ij}} \left[\left(1 + \frac{ikR_{ij} - 1}{k^2 R_{ij}^2} \right) \mathbb{I} + \frac{3 - 3ikR_{ij} - k^2 R_{ij}^2}{k^2 R_{ij}^2} \frac{\mathbf{R}_{ij} \otimes \mathbf{R}_{ij}}{R_{ij}^2} \right] \quad (1.12)$$

Where \mathbb{I} is the 3×3 identity matrix. This equation accounts for the full electromagnetic interaction between the two particles, with terms depending on $(kR_{ij})^{-3}$, $(kR_{ij})^{-2}$ and $(kR_{ij})^{-1}$ associated with the near-, intermediate-, and far-field interactions, correspondingly. Additionally, the off-diagonal terms in $\vec{\mathbf{A}}_{ij}$ enable inter-polarization influence. From Eqs. (1.9) and (1.10) a set of $3N$ linear equations can be obtained:

$$\mathbf{A}' \mathbf{P} = \mathbf{E}_{app} \quad (1.13)$$

Where \mathbf{P} and \mathbf{E}_{app} are $3N$ -dimensional vectors composed of the 3 components of polarization and applied electric field for each of the particles in the array, respectively. \mathbf{A}' is a $3N \times 3N$ interaction block matrix, that contains all the information about the coupling properties of the system, regardless of the applied field. It is composed of 3×3 blocks, where the N diagonal blocks corresponds to $\vec{\alpha}_{s,i}^{-1}$ and the off-diagonal blocks are according to $\vec{\mathbf{A}}_{ij}$ from Eq. (1.12). By

numerically inverting the matrix \mathbf{A}' Eq. (1.13) can be solved to obtain the polarization at each array site: $\mathbf{P} = \mathbf{A}'^{-1}\mathbf{E}_{app}$.

From the polarization vectors, the extinction cross section of the array can be calculated by summing over the extinction of all individual particles [80]:

$$\sigma_{ext} = 4\pi k \sum_{i=1}^N \frac{\Im\{E_{app,i}^* P_i\}}{|E_{app,i}|^2} \quad (1.14)$$

Infinite periodic arrays

In the case of an infinite periodic array of identical particles a simplification to the above derivation can be done, which results in an insightful analytical expression that reveals the fundamentals of the hybridized resonances studied at this thesis. The simplification is performed by considering an applied plane wave of the form $\mathbf{E}_{app,i} = \mathbf{E}_0 e^{-i\mathbf{k}_{\parallel} r_i}$ and presenting an effective polarizability for each particle in the presence of the array, $\vec{\alpha}_{eff}$, that fulfills the relation $\mathbf{P}_i = \vec{\alpha}_{eff} \mathbf{E}_{app}$. According to Bloch's theorem, the polarization of each particle can differ only by the phase factor associated with the incident field, i.e. $\mathbf{P}_i = \mathbf{P}_0 e^{-i\mathbf{k}_{\parallel} r_i}$. By choosing $r_0 = 0$ and defining the array's incident angle-dependent structural factor as $\vec{S}(\mathbf{k}_{\parallel}) \equiv \sum_{j \neq 0} \vec{A}_{0j} e^{-i\mathbf{k}_{\parallel} r_j}$, where \mathbf{k}_{\parallel} is the parallel to the surface component of the incident wave vector, the effective polarizability can be obtained from Eqs. (1.9) and (1.10):

$$\vec{\alpha}_{eff} = (1 - \vec{\alpha}_s \vec{S}(\mathbf{k}_{\parallel}))^{-1} \vec{\alpha}_s \quad (1.15)$$

This equation enables calculating $\vec{\alpha}_{eff}$ directly from $\vec{\alpha}_s$ and \vec{A}_{ij} , without the need to solve a system of coupled linear equations. We note that the matrix inversion required for solving Eq. (1.15) is only for a 3×3 matrix, rather than the inversion of $3N \times 3N$ matrix required to solve Eq. (1.13). For further exploration of this important result, it is convenient to look at the scalar case, i.e. studying specific polarization component, and accounting for scalar quantities of \mathbf{E}_{app} , \mathbf{E}_{loc} , \mathbf{E}_{sca} , $\vec{\alpha}_s$, $\vec{\alpha}_{eff}$, \vec{A}_{ij} and \vec{S} . This approximation is valid in many configurations, specifically in most cases where the nanoparticles has dominant isotropic response, i.e. with vanishingly small off-diagonal terms in $\vec{\alpha}_s$. In these cases, even if the applied field has more than one component of polarization, each component of the problem can be treated separately within the scalar framework. Yet, it is worth mentioning that \vec{A}_{ij} and therefore also \vec{S} always have off-diagonal terms. These terms, for judiciously engineered surfaces, may cause substantial anisotropic response of $\vec{\alpha}_{eff}$, even for purely diagonal $\vec{\alpha}_s$. A common case in which

the scalar approximation is fully exact, is when $\vec{\alpha}_s$ has only a single non-vanishing term on its diagonal. In this case, the fields radiating at the array at different polarization than the applied field, resulting from the non-diagonal terms of \vec{A}_{ij} , cannot give rise to change in the polarization of the nanoparticles. Overall, the validity of the scalar approximation needs to be considered for each specific configuration. Under this approximation, Eq. (1.15) takes the following form:

$$\alpha_{eff} = \frac{\alpha_s}{1 - S(\mathbf{k}_{||})\alpha_s} \quad (1.16)$$

From this equation it is possible to obtain insights on the interplay between the single particle and the entire array response, manifested by α_s and $S(\mathbf{k}_{||})$ accordingly. To fully understand the outcomes of this result it is essential to take a close look at the properties of α_s and S . As discussed in section 1.1.1, α_s is associated with localized modes, which in the case of metallic nanoparticle origins from the plasmonic response. On the contrary, the array's structural factor $S(\mathbf{k}_{||})$ accounts for the light scattering at the array, and therefore its resonant response is associated with distributed photonic modes. Further exploration of $S(\mathbf{k}_{||})$ and its resonance properties in periodic arrays appears in the following sub-section. Following the discussion on the properties of $S(\mathbf{k}_{||})$, the new resonances that emerge from Eq. (1.16), i.e. the SLRs, will be discussed.

Diffraction directions and coherent scattering at the Rayleigh anomalies

In nanoparticle arrays two main regimes of operation can be distinguished by the lattice spacing of the array. The first is the sub-diffraction regime, where the lattice spacing is sufficiently small to allow only zero-order forward and backward scattering. In this regime, the net optical response stems predominantly from the single nanoparticle scattering, with near field influenced variations due to the coupling between adjacent nanoparticles. The second is the diffractive regime, where the lattice spacing allows higher order diffraction, and richer manipulation of the forward and backward scattering light can be achieved [4,81]. In-between the two regimes exist the diffraction edge where light diffracts on the surface and long-range collective interactions play a vital role in the optical response. While this description holds for the first order of diffraction, higher orders will also satisfy the surface diffraction condition well inside the photonic regime.

To examine these regimes, it is insightful to express the directions of diffraction from the array by means of the quasi-momentum conservation condition:

$$\mathbf{k}_{\parallel} + \mathbf{G}_{\langle m_1, m_2 \rangle} = \mathbf{k}_{\parallel, \langle m_1, m_2 \rangle}^{t/r} \quad (1.17)$$

Here $\mathbf{k}_{\parallel, \langle m_1, m_2 \rangle}^{t/r}$ is the parallel component of the transmitted/reflected wave vector of order $\langle m_1, m_2 \rangle$, and $\vec{G}_{\langle m_1, m_2 \rangle} = m_1 \vec{b}_1 + m_2 \vec{b}_2$ is a general reciprocal lattice vector which is a linear combination of the primitive lattice vectors (b_1, b_2). The $\langle m_1, m_2 \rangle$ order will diffract to the far field only if the magnitude of $\mathbf{k}_{\parallel, \langle m_1, m_2 \rangle}^{t/r}$ is smaller than k . When this magnitude exactly equals k , a spatial diffraction order radiates at a grazing angle to the surface, causing redistribution of the energy between the diffractive channels, a condition that is known as the Rayleigh anomaly (RA) [82]:

$$\mathbf{k}_{\parallel} + \mathbf{G}_{\langle m_1, m_2 \rangle} = \mathbf{k}_s \quad (1.18)$$

Where $\mathbf{k}_s = k \hat{\mathbf{k}}_s$ is the surface scattered wave and the vector $\hat{\mathbf{k}}_s$ is a unit vector specifying the direction of the scattered surface wave vector.

To obtain further insight on the origin and meaning of the RA condition, we will examine its emergence through the array's incident angle-dependent structural factor $S(\mathbf{k}_{\parallel})$. This factor is a complex parameter that is calculated by summing the Green's functions of the entire array, according to Eq. (1.12). One can simplify $S(\mathbf{k}_{\parallel})$ for the scalar case by accounting only for the relevant term in the 3×3 tensor \vec{A}_{ij} . We note that each column vector in \vec{A}_{ij} specifies the electric field emitted from a dipole that is aligned with the associated axis. Therefore, for the case where the polarization of the applied field is parallel to the plane of the array, $S(\mathbf{k}_{\parallel})$ can be expressed as follows:

$$S(\mathbf{k}_{\parallel}) = \sum_{j \neq 0} e^{-i(k_{\parallel} - k)r_j} \left[\frac{(1 - ikr_j)(3 \cos^2 \theta_j - 1)}{r_j^3} + \frac{k^2 \sin^2 \theta_j}{r_j} \right] \quad (1.19)$$

Where θ_j is the angle between the vectors \mathbf{E}_{inc} and \mathbf{r}_j . The sum over the complex terms, associated with the scattered fields from all particles, coherently builds-up exactly at the RA condition. A typical example of the structural factor $S(\mathbf{k}_{\parallel})$ is shown in Figure 1.2 for 1D array at normal incidence. The parameters taken are: wavelength $\lambda \in [900 \text{ nm}, 2100 \text{ nm}]$, lattice spacing $d = 1000 \text{ nm}$ and surrounding refractive index $n = 1.5$. It can be seen that the magnitude of $S(\mathbf{k}_{\parallel})$ significantly increases in the vicinity of the RA at $\lambda = nd = 1500 \text{ nm}$, with phase response varying over the entire 2π range. The width of the peak of $S(\mathbf{k}_{\parallel})$ is much narrower than the width of the resonance of α_s of the single nanoparticle.

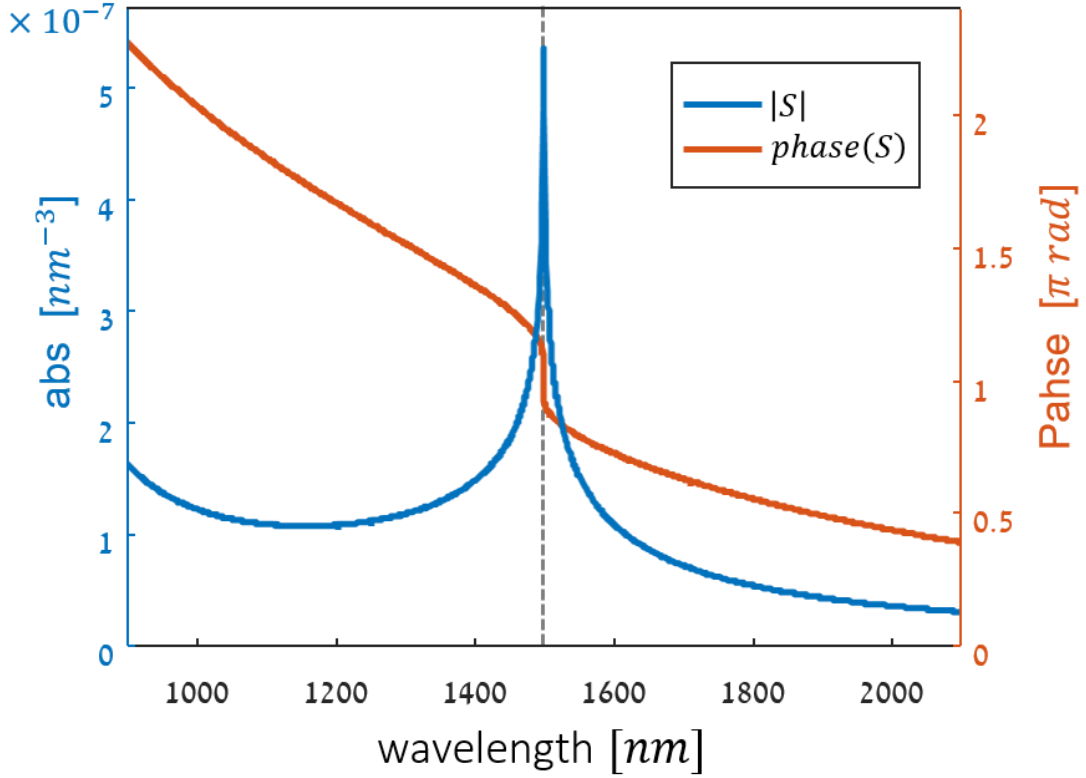


Figure 1.2. Typical trend of the array's structural factor $S(\mathbf{k}_{||})$. The calculation corresponds to 1D array at normal incidence, with lattice spacing $d = 1000 \text{ nm}$ and surrounding refractive index $n = 1.5$. It can be seen that the magnitude of $S(\mathbf{k}_{||})$ significantly increases in the vicinity of the RA at $\lambda = nd = 1500 \text{ nm}$, indicated by the gray dashed line. The associated phase varies over the entire 2π range. The width of the peak of $S(\mathbf{k}_{||})$ is much narrower than the width of the resonance of α_S .

Surface lattice resonance

When the single nanoparticle resonance and the lattice RA are tuned to the same spectral range, coupling between the modes can play an essential role in the optical response of the array. This coupling gives rise to new resonances associated with surface waves that coherently mediate the interaction between the array components. In the case of plasmonic nanoparticles, these new formed resonances result from a photonic-plasmonic mode hybridization and are often termed SLRs. These hybridized resonances exhibit sharp spectral features and enable a variety of phenomena to take place [75].

The condition for appearance of a SLR can be obtained by rewriting Eq. (1.16) while explicitly separating $1/\alpha$ and S to their real and imaginary parts. For convenience we define $\Delta \equiv$

$\Re\{\alpha_s^{-1} - S\}$ and $\Gamma \equiv \Im\{\alpha_s^{-1} - S\}$, where \Re and \Im denote the real and imaginary parts, and obtain the following relation:

$$\alpha_{eff} = \frac{1}{\Delta + i\Gamma} \quad (1.20)$$

From here, when Δ vanishes the SLR condition is met, with dissipation determined by Γ . Furthermore, two types of SLRs can be distinguished [83]; Type 1: occurs when the minimum of Δ is positive and then a single narrow Fano-type resonance appears at the RA condition. Type 2: occurs when the minimum of Δ is negative, and then the curve of $\Re\{\alpha_s^{-1}\}$ intersects twice the curve of $\Re\{S\}$. At this case two unequal collective resonances of α_{eff} are observed, while in between these resonances, at the RA, reduced extinction gap may form.

1.2 Nonlinear metasurfaces

Whereas linear optics and the manipulation of light have been studied since ancient times, the field of nonlinear optics emerged in 1960s with the seminal work of Armstrong and Bloembergen [84], following the invention of the laser. In the field of nanophotonics, the great success in the development of linear metasurfaces with unique optical properties [16,17,22–27,72,85–87], naturally led to the flourishing research front of nonlinear metasurfaces. By judiciously nanostructuring the metasurfaces, while leveraging the field confinement and enhancement associated with their resonances, unprecedented control over the nonlinear interaction is obtain. Specifically, great research strides with prominent success deal with the generation efficiency of the nonlinear processes [2,5,88–90], and the manipulation of spatial distribution of radiated fields in new frequencies [4,57,81,91–93]. The generation efficiency has surpassed that of naturally existing materials of the same dimensions [6,94], and nonlinear metasurface beam shaping, has reached impressive achievements of nonlinear wave control. By controlling the amplitude, phase, and polarization of the local nonlinear response, numerous manipulation schemes were demonstrated. Some examples include manifestation of a nonlinear Fresnel zone plate that focuses the generated nonlinear light [4], far-field generation of second harmonic (SH) Airy and vortex beams [81], generation of third-harmonic holograms from multilayer metasurfaces [91], novel cryptography technique based on nonlinear holography [92] and simultaneous control of spin and orbital angular momentum in second-harmonic generation [93].

In sub-section 1.2.1, we shortly review the basics of quadratic nonlinear interactions. Then, in sub-section 1.2.2 we focus specifically on these interactions in plasmonic metasurfaces.

1.2.1 Quadratic nonlinear interactions

Fundamental for the nonlinear interaction of light with matter is the governing wave equation and the existence of nonlinear polarization terms. In the following, we introduce these concepts and the basics of the generation of light at new frequencies, specifically by quadratic nonlinear processes.

The interaction of light, i.e. electromagnetic waves, and matter can be described generally by the wave equation³:

$$\nabla^2 \mathbf{E} - \frac{1}{c^2} \frac{\partial^2 \mathbf{E}}{\partial t^2} = \frac{1}{\epsilon_0 c^2} \frac{\partial^2 \mathbf{P}}{\partial t^2} \quad (1.21)$$

Where \mathbf{E} is the electric field representing the light, \mathbf{P} is the polarization in the material, which acts as the source for electromagnetic waves, and ϵ_0 is the vacuum permittivity. The polarization is induced by the external field, which is the light itself. The relation between the induced polarization of a material and the applied electric field is, in general, nonlinear. Their dependence, in the perturbative regime, can be described by a Taylor expansion:

$$\mathbf{P}(\mathbf{E}) = \epsilon_0 (\chi^{(1)} \mathbf{E} + \chi^{(2)} \mathbf{E}^2 + \chi^{(3)} \mathbf{E}^3 + \dots) \equiv \mathbf{P}^{(L)} + \mathbf{P}^{(NL)} \quad (1.22)$$

Where $\chi^{(1)}$, $\chi^{(2)}$ and $\chi^{(3)}$ are the linear, quadratic, and cubic susceptibilities, respectively, and higher-order susceptibilities are not shown. The linear and nonlinear terms of polarization, $\mathbf{P}^{(L)}$ and $\mathbf{P}^{(NL)}$ respectively, are in accordance to the partition in Eq. (1.22) and the equation $\mathbf{P}^{(L)} \equiv \epsilon_0 \chi^{(1)} \mathbf{E}$. It is important to note that the susceptibility is of a tensorial form, and depends on the interaction type and participating frequencies [95]. The nonlinear terms in this expansion allow for the description of the generation of light at new frequencies and additional nonlinear phenomena that emerge from photon-photon interactions.

Plugging Eq. (1.22) into the wave equation, we get

$$\nabla^2 \mathbf{E} - \frac{n^2}{c^2} \frac{\partial^2 \mathbf{E}}{\partial t^2} = \frac{1}{\epsilon_0 c^2} \frac{\partial^2 \mathbf{P}^{(NL)}}{\partial t^2} \quad (1.23)$$

with $n = 1 + \chi^{(1)}$ and $\mathbf{P}^{(NL)}$ as the nonlinear term of the polarization. The case of quadratic nonlinearity can be demonstrated with a general fundamental field composed of two different frequencies, ω_1 and ω_2 :

$$\mathbf{E}(t) = \mathbf{E}_1 e^{-i\omega_1 t} + \mathbf{E}_2 e^{-i\omega_2 t} + c.c \quad (1.24)$$

³ Section 1.2.1 is written in SI system of units.

This kind of field induces a quadratic polarization of the form:

$$\begin{aligned}
\mathbf{P}^{(2)} = & \epsilon_0(\overleftrightarrow{\chi}_{SHG}^{(2)} \mathbf{E}_1 \mathbf{E}_1 e^{-i(2\omega_1)t} + \overleftrightarrow{\chi}_{SHG}^{(2)} \mathbf{E}_2 \mathbf{E}_2 e^{-i(2\omega_2)t} \\
& + \overleftrightarrow{\chi}_{SFG}^{(2)} \mathbf{E}_1 \mathbf{E}_2 e^{-i(\omega_1+\omega_2)t} + \overleftrightarrow{\chi}_{DFG}^{(2)} \mathbf{E}_1 \mathbf{E}_2^* e^{-i(\omega_1-\omega_2)t} \\
& + \overleftrightarrow{\chi}_{OR}^{(2)} \mathbf{E}_1 \mathbf{E}_1^* + \overleftrightarrow{\chi}_{OR}^{(2)} \mathbf{E}_2 \mathbf{E}_2^* + c. c.) \quad (1.25)
\end{aligned}$$

Here we explicitly wrote the susceptibilities as tensors. The quadratic nonlinearity induces oscillating polarization at new frequencies, and as a result new waves are generated. The generation of waves at $2\omega_1$ and $2\omega_2$, is known as second-harmonic generation (SHG), the waves at $\omega_1 + \omega_2$ and $\omega_1 - \omega_2$ are referred to as sum-frequency and difference-frequency generation (SFG and DFG), respectively. In addition, a DC polarization is induced in a process named optical rectification (OR). All these processes, where fields at frequencies ω_1 and ω_2 , are generating field at a new frequency, are called three-waves mixing (TWM).

The quadratic nonlinear response of material with light is the fundamental interaction of many nonlinear phenomena including the mentioned TWM processes, Pockels effect and spontaneous parametric down conversion. These interactions and more provide the foundation for many applicative devices such as optical parametric oscillators (OPOs), optical parametric amplifiers, optical switches by photon-photon interactions, Pockels cells, entangled photons generation and more.

One of the fundamental characteristics of quadratic nonlinear susceptibility is the requirement of local symmetry breaking. For centrosymmetric materials, Eq. (1.21) gives the condition that locally $P(E) = -P(-E)$. Consequently, as can be seen from Eq. (1.22), all of the even-order terms in the expansion for centrosymmetric materials must disappear. Therefore, quadratic interactions, for example, cannot be observed in bulk centrosymmetric materials. Yet, at the boundaries between materials the symmetry is broken, and even-order interactions are allowed. In section 1.2.2 we will reexamine this idea in the context of plasmonic nanoparticles, and see that the surface contribution to the SHG can result in substantial conversion efficiencies even when centrosymmetric materials, as gold, are considered.

An important phenomenon that is relevant for all wave mixing effects in bulk nonlinear materials is phase mismatch. In general, due to chromatic dispersion in materials, each of the participating waves accumulates different phase along the propagation in the nonlinear medium. This results eventually in a phase between the interacting wave and in inefficient interaction. Therefore, for efficient nonlinear conversion, it is required that these phases will be matched [95]. For example, in collinear sum-frequency generation, the phase mismatch is given by $\Delta kL = (k_3 - k_1 - k_2)L$ where k indicates the momentum of each participating waves and L is the interaction length. The phase mismatch can be controlled and reduced to zero by several methods, including critical phase matching and quasi phase matching [95]. In the latter, the

nonlinear coefficient is periodically modulated thus introducing a lattice momentum that can be exploited for phase compensation.

1.2.2 Nonlinear plasmonic metasurfaces

The emergence of nonlinear plasmonic metasurfaces is commonly attributed to the paper by Klein et al. [2] in 2006, following the predictions of Sir John Pendry et al. [1]. In the work by Klein et al., SH emission was measured from metasurface composed of SRRs. It was shown that the linear resonances, both in the fundamental frequency (FF) and SH, were crucial for efficient emission of the SH. In addition, relevant to this work and to all other works of nonlinear metasurfaces, phase-mismatch concerns that usually exist in nonlinear interactions in bulk materials were removed thanks to the short interaction length. Since Klein's paper, the field of nonlinear metasurfaces is exponentially growing. The source of the nonlinear interaction was theoretically studied and several models were suggested and tested [3,89,96–99]. In parallel, different types of metasurfaces were investigated, in order to better understand the phenomena and expand their capabilities. Prior to the work presented in section 2.1, some pioneering works have suggested that, similar to the linear regime, the collective nonlinear interaction over the array may influence the overall nonlinear optical response of the metasurface [100,101]. Further related insights are brought rigorously in section 2.1, along with short survey of more recent works in Chapter 3 .

Quadratic nonlinear response of a single plasmonic nanoparticle

On the level of the single plasmonic nanoparticle, several considerations were shown to be crucial for efficient quadratic nonlinearity. These include local symmetry breaking on the interface of the nanostructure, field enhancement due to excitation of LSPRs, asymmetry of the nanostructure which leads to efficient generation of nonlinear currents in a bright emission mode at the nonlinear output, and good spatial overlap between the localized modes participating in the nonlinear interaction. In the following we shortly review these concepts.

The significant role of field enhancement in the efficiency of the nonlinear processes can be appreciated from the super-linear dependence of the nonlinear polarization on the electric field, as seen from Eq. (1.22). Specifically, the influence of linear resonances on the generation efficiency of the nonlinear fields is often treated qualitatively by the outcomes of the Miller's rule [95,102]. This rule was introduced in 1964 by R. C. Miller, as an empirical rule that enables predicting the magnitude of the nonlinear second-order susceptibility in terms of the linear susceptibility. Later, it was shown that anharmonic oscillator model for the source of the

nonlinearity yields the same result of Miller [95]. Today, though it is understood that Miller's rule cannot capture the full dynamics of nonlinear generation in metasurfaces, when correctly applied, it still gives valuable insights and enables fast calculations of the nonlinear outcomes from metasurfaces. By describing the linear susceptibility in the form of a Lorentzian,

$$\chi^{(1)}(\omega) \propto \frac{1}{D(\omega)} , \quad (1.26)$$

with $D(\omega) \equiv \omega_0^2 - \omega^2 - i\gamma\omega$, Miller's rule states that the nonlinear second-order susceptibility will be

$$\chi^{(2)}(2\omega; \omega, \omega) \propto [\chi^{(1)}(\omega)]^2 \chi^{(1)}(2\omega) \propto \frac{1}{[D(\omega)]^2 D(2\omega)} \quad (1.27)$$

Thus, the linear resonances, manifested by the conditions $\Re\{D(\omega_i)\} = 0$ ($i = 1, 2$, $\omega_1 = \omega$ and $\omega_2 = 2\omega$), are crucial for determining the nonlinear response. As Eq. (1.27) can be obtained analytically by relying on anharmonic oscillator model, it is possible to extend this result to the general case of TWM, in-addition to nonlinear processes of higher orders. Under this model, local symmetry breaking should take place in order to obtain the even-order nonlinear response, as expected from the discussion in section 1.2.1. This naturally occurs at interfaces, and therefore the high surface-to-volume ratio of small particles make them highly attractive candidates for strong quadratic interaction.

The above description enables predicting strong nonlinear interactions of plasmonic nanoparticles when excited at resonance. Nevertheless, in order to apply this model to describe the generation efficiency in plasmonic nanoparticles, one should note that $D(\omega_i)$ in Eq. (1.27) cannot simply describe the LSPRs condition. Qualitatively, the reason for that can be described as follows: Eq. (1.27) has the potential only to describe the local response at a certain point, much smaller than the optical wavelength, on the nanoparticle. The generation of nonlinear fields at all single points on the nanoparticle will determine the nonlinear currents and charge distribution on the nanoparticle. In turn, these will define the radiation patterns at the new generated frequencies. Therefore, in order to obtain bright emission of the generated nonlinear mode, the linear spatial field distribution at the participating modes should be considered. This concept is described more rigorously through the framework of nonlinear scattering theories, which enable quantitative calculation of the emitted nonlinear signal. For example, for SHG in a metal nanoparticle, one obtains:

$$\chi^{(2)}(2\omega; \omega, \omega) \propto \int_S \chi_{\perp\perp\perp}^{(2)} E_{\perp}^2(\omega, \mathbf{r}) E_{\perp}(2\omega, \mathbf{r}) dS \quad (1.28)$$

The susceptibility $\chi^{(2)}(2\omega; \omega, \omega)$ is proportional to the mode mixing integrated over the surface of the nanoresonator. Here, $\chi_{\perp\perp\perp}^{(2)}$ denotes the nonlinear tensor element that mixes the normal field components, $E_{\perp}(\omega)$ and $E_{\perp}(2\omega)$, which correspond to the FF and SH mode fields, respectively. The integration is done only on the surface due to the intrinsic symmetry of the considered metal, which cause the local quadratic susceptibility to vanish in the bulk. Eq. (1.28) implies that good spatial mode matching is required for efficient SHG. Additional leading approach for simulating the nonlinearity in plasmonic nanoparticles, which served for performing the simulations in Figure 1.3(b), is based on the nonlinear hydro-dynamical model for electron gas [96].

An important outcome of the above descriptions, which is captured by the different methods for simulating the nonlinearity, is that particles with centro-symmetric shapes, though having SH at the near field, will not radiate SH to the far field along the illumination direction. This is shown in Figure 1.3(a).

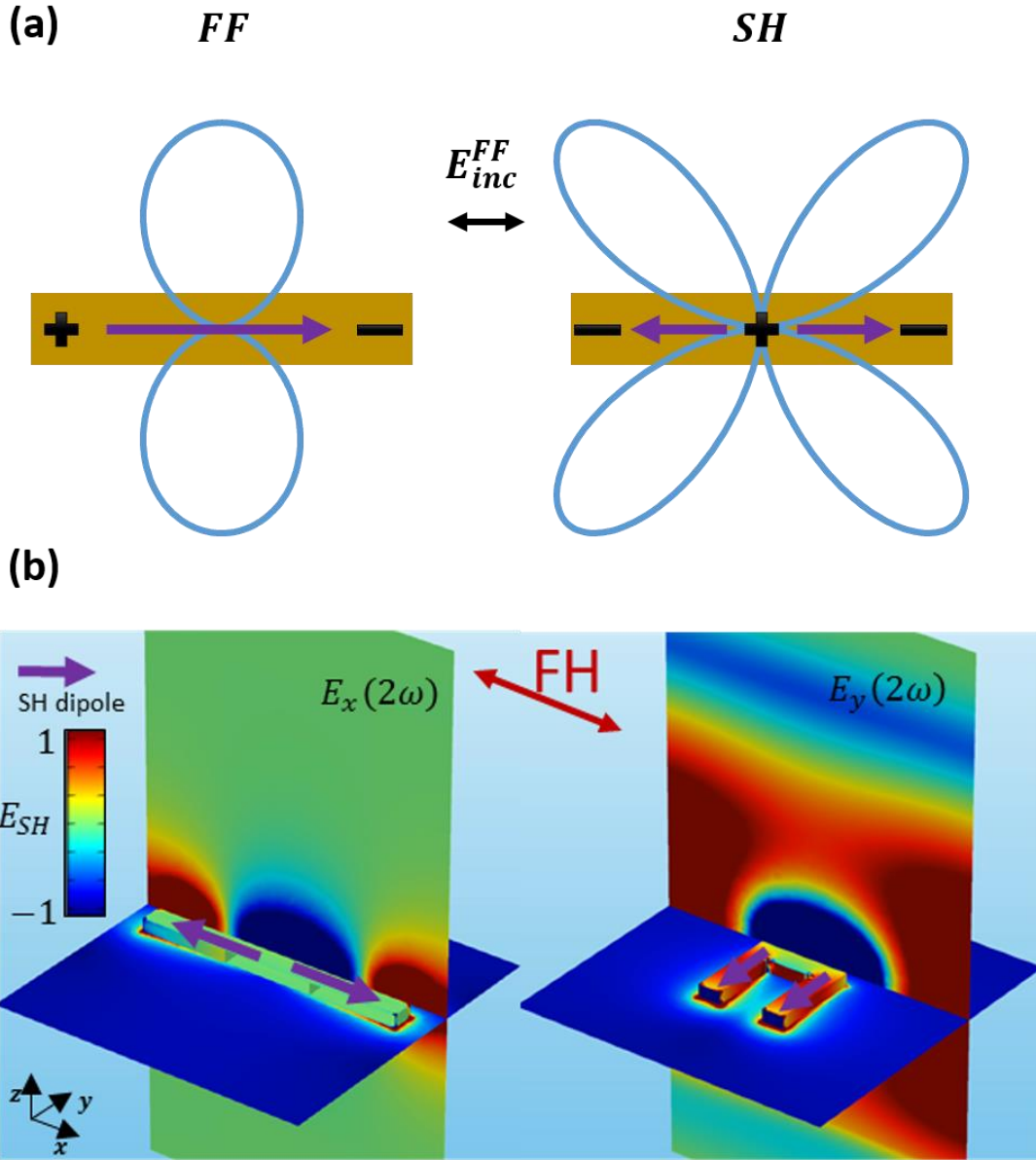


Figure 1.3. Generation and far-field emission of SH in symmetric vs. asymmetric nanoparticles. (a) Schematic illustrations of a rod illuminated at its FF dipole mode. The left and the right figures show the FF and SH response, respectively. The induced currents, charge distributions and far-field radiation pattern are shown. While the charge distribution and currents of the SH (right figure) indicate existence of SHG in the near field, the associated quadrupole radiation pattern will result in zero net emission to the forward direction. If the array periodicity does not support diffraction orders to the directions of the quadrupole emission, there will be no emission of the SH to the far field. This is shown in (b). (b) Simulations of the SH emission from a rod and a SRR, within an infinite array. The simulations, based on the nonlinear hydro-dynamic model, shows a single unit cell of an array. The field generated by the nonlinear currents, propagates away from the SRR and vanishes away from the rod [57].

Directions of nonlinear diffraction from a nanoparticle array

The coherent buildup of nonlinear fields generated at different spatial points, dictates the directions of emitted radiation from two-dimensional nanoparticle array. This, so called spatial

nonlinear diffraction orders, can be found via quasi-momentum conservation considerations, and are given by the nonlinear Raman-Nath relations [103]. For example, for SHG:

$$2(\mathbf{k}_1)_{\parallel} + \mathbf{G}_{\langle m_1, m_2 \rangle} = (\mathbf{k}_2^{t/r})_{\parallel, \langle m_1, m_2 \rangle} \quad (1.29)$$

Where \mathbf{k}_1 and \mathbf{k}_2 denotes the FF and SH wave vector, respectively. $(\mathbf{k}_2^{t/r})_{\parallel, \langle m_1, m_2 \rangle}$ is the parallel component of the transmitted/reflected wave vector of order $\langle m_1, m_2 \rangle$ of the SH. Similar to the linear case, the $\langle m_1, m_2 \rangle$ order will diffract to the far field only if the magnitude of $(\mathbf{k}_2^{t/r})_{\parallel, \langle m_1, m_2 \rangle}$ is smaller than k_2 .

Collective nonlinear response of a nanoparticle array

Despite increasing interest in nonlinear effects, not much work was devoted to study collective nonlinear interactions. Linden et al. found that arrays of SRRs emit SH with varying efficiency according to different array spacing in the sub-diffraction regime [100]. These variations can be attributed to short-range interactions. In 2016, Czaplicki et al. showed that long-range interactions, causing a linear SLR, can result in ten-fold emission enhancement of the SH fields [101]. Further understandings regarding the influence of the interplay between the single particle and the collective array response in the nonlinear regime are presented in the Chapter 2 , section 2.1, and in Chapter 3 , containing the summary and outlook of this thesis. The presented results extend the existing body of theoretical and experimental research in nonlinear plasmonics, and introduce a new framework to understand variations in the nonlinear optical response caused by both short- and long-range interactions.

1.3 Slow light

As will be seen in section 2.2, my research involves manipulation of the velocity of light via control over the collective interaction in metasurfaces. Therefore, this section presents the basics of slow light and time domain description of short pulses, necessary for the understanding of section 2.2.

The velocity of light propagating at free space is $c_0 = 299,792,458 \text{ ms}^{-1}$, fast enough to make 7.5 round-the-world trips in a single second. In dielectric media this velocity is reduced by a factor of approximately the refractive index, which is typically between 1 to 4, to $\sim c_0/n$. This ultra-high velocity is advantageous for communication applications and ultra-fast transmission of visual data. However, the possibility to reduce and control the light's velocity is beneficial for wide-range applications. A wide variety of application belong to all optical

time-domain signal processing [104,105], but it is also beneficial for enhancing nonlinear effects and miniaturizing numerous optical devices such as amplifiers, detectors, absorption modulators and wavelength converters [106,107]. In the last decades, mechanisms to reduce light velocity have been extensively explored, resulting in the flourishing research area of slow light [106,108,109]. This term refers to reduction of the group velocity of light. Though the motivation for slowing down the light stems mainly from its potential for advanced technological devices, the related mechanisms revealed exciting physics. For example, the intriguing quantum coherent effect of electromagnetic induced transparency (EIT) from atomic physics [110], which was proven attractive for implementing slow light devices, has found counterparts in nanophotonics [111–113], optomechanics [114–116] and condensed matter systems [117–119] supporting coupled resonances.

The quantification of how slow the light is, often refers to the associated group velocity $v_g = d\omega/dk$, which describes the speed at which the pulse envelope propagates. Alternatively, one can examine the light's group delay $\tau_g = -d\phi/d\omega$, in comparison to the group delay of the same configuration without the interaction producing the slow light. Here, ϕ is the accumulated phase of the light through the device. Using the group delay expression relaxes the hidden assumption of a homogeneous medium composed of sub-wavelength separated inclusions, which might exist when using the group velocity terminology. Therefore, in this thesis, while examining the slow light behavior of wavelength-scale spaced nanoparticle array, the related group delay will be calculated.

The group delay can be quantified by measuring the spectral phase. This, in turn, is possible with spectral interferometric methods, as described in section 1.4. The challenges in performing phase measurements for metasurfaces in general, and specifically when flexible illumination conditions are required, is addressed in Chapter 2. Here, in order to elucidate the relation between the group delay definition in the spectral domain to its manifestation in the time domain, we will examine its role in describing a pulse that passes through a dispersive linear optical device. Assume a device that can be characterized by a complex transfer function, in the frequency domain, of the general form:

$$H(\omega) = R(\omega)e^{-i\phi(\omega)} \quad (1.30)$$

The functions $R(\omega)$ and $\phi(\omega)$ are the amplitude and phase of $H(\omega)$, respectively. If we denote the field at the input of the device $E_{in}(\omega)$, then at the output the field will be:

$$E_{out}(\omega) = E_{in}(\omega)H(\omega) = E_{in}(\omega)R(\omega)e^{-i\phi(\omega)} \quad (1.31)$$

To get an insight of how the phase imparted by the device affects the light pulse, we assume $R(\omega) = R$, and transform Fourier the output pulse to the time domain:

$$E_{out}(t) = \frac{1}{2\pi} \int_{-\infty}^{\infty} E_{out}(\omega) e^{i\omega t} d\omega = \frac{1}{2\pi} R \int_{-\infty}^{\infty} E_{in}(\omega) e^{-i\phi(\omega)} e^{i\omega t} d\omega \quad (1.32)$$

By replacing $\phi(\omega)$ by its Taylor expansion around the carrier frequency ω_c of the incident pulse, we get:

$$\phi(\omega) = \sum_{n=0}^{\infty} b_n (\omega - \omega_c)^n \quad (1.33)$$

Where the expansion coefficients are:

$$b_n = \frac{1}{n!} \left. \frac{d^n \phi}{d\omega^n} \right|_{\omega_c} \quad (1.34)$$

Plugging Eq. (1.33) into Eq. (1.32) we obtain for the pulse:

$$E_{out}(t) = \frac{1}{2\pi} R \cdot e^{-ib_0} e^{i\omega_c t} \int_{-\infty}^{\infty} E_{in}(\omega) e^{-i(\sum_{n=2}^{\infty} b_n (\omega - \omega_c)^n)} e^{i(\omega - \omega_c)(t - b_1)} d\omega \quad (1.35)$$

From this equation we can interpret the effect of the various expansion coefficients b_n . Specifically, $b_1 \equiv -\tau_g = d\phi/d\omega$, leads solely to a shift of the pulse on the time axis t , without any deformations to the shape of its envelope. It is interesting to note the effect of other coefficients. The term e^{-ib_0} is a constant phase shift (phase delay) having no effect on the pulse envelope, while the b_n terms with $n > 1$ produce a nonlinear behavior of the spectral phase, which changes the pulse envelope and chirp.

1.4 Spectral interferometry

The information carried by a light beam can be encoded in its various properties as amplitude, phase, spatial distribution and polarization. Conventional light detectors are sensitive only to the light intensity, due to response times much longer than the optical cycle. Therefore, the amplitude, spatial distribution and polarization of light can be easily measured, while **characterization** of the phase of light is typically a much more challenging task. This task is treated in the framework of the interferometry field. Specifically, spectral interferometry enables quantification of the frequency-dependent phase of light. This, in turn, enables determination of the phase term from Eq. (1.30), of the complex transmission (or reflection) transfer function of an optical element under inspection. In this section we shortly describe the basics of interferometry. That will serve as the background to my research on spectral interferometric microscopy, described in detail in section 2.3. For further reading on

interferometry, with specific emphasis on spectral interferometry, there are multiple relevant textbooks and papers [120–124].

The basic operation principle of interferometric methods is to convert the phase information, which cannot be directly measured, to amplitude information. This is done by interfering several light beams and measuring the resulting amplitude. Most commonly, two light beams are interfered, as done in the instructive example of Michelson interferometer (see Figure 1.4). Light emanating from a source is divided by a beam splitter into two beams, E_1 and E_2 . Concentrating, for example, on measuring the complex transmission transfer function of a sample, the interferometer is set such that in one path the light passes twice through the sample. After being reflected from the mirrors, the two beams are recombined by the beam splitter to an intensity-sensitive detector. If we decompose the fields at the detector to amplitude and phase terms, i.e. $E_1 = A_1 e^{-i\phi_1}$ and $E_2 = A_2 e^{-i\phi_2}$, we can express the intensity measured by the detector as:

$$I = |E_1 + E_2|^2 = |E_1|^2 + |E_2|^2 + E_1^* E_2 + E_2^* E_1 = A_1^2 + A_2^2 + 2A_1 A_2 \cos(\Delta\phi) \quad (1.36)$$

Where $\Delta\phi = \phi_2 - \phi_1$. The interferometer can be set such that, when arriving to the detector, the beams E_1 and E_2 differ only due to the interaction with the sample, which has a complex transmission transfer function $H = R e^{i\phi}$. Therefore, we can express the beams as $E_1 = A_1 e^{-i\phi_1}$, $E_2 = E_1 H^2$, and obtain the intensity as function of the transfer function parameters:

$$I = A_1^2 [1 + R^4 + 2R^2 \cos(2\phi)] \quad (1.37)$$

The measured intensity is directly influenced by the phase of the sample. Using the Michelson interferometer the spectral phase of the sample, i.e. $\phi(\omega)$, can be obtained either by performing multiple measurements of the intensity for varying displacements of the movable mirror or, without any moving mechanical parts, by placing a spectrometer instead of the simple intensity detector [123]. The first method results in a time-resolved interferogram, while the second results in a spectrally resolved interferogram.

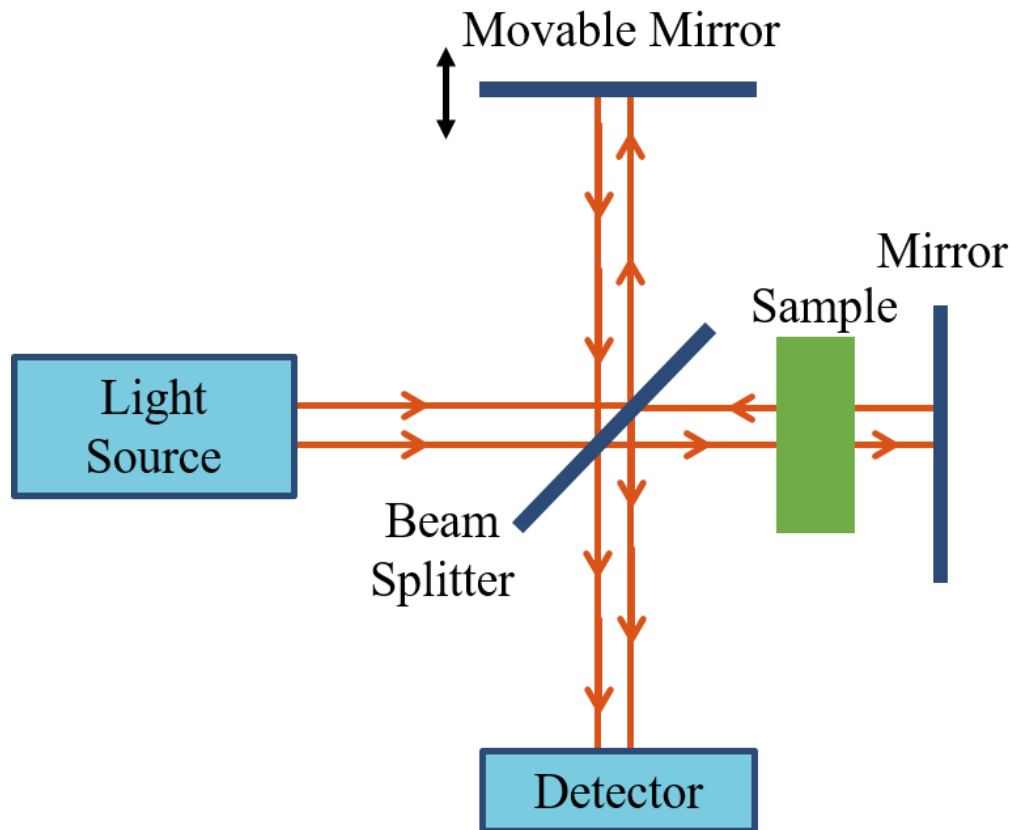


Figure 1.4. Michelson interferometer. Light emanating from a source is divided by a beam splitter into two separate paths. In one path the light passes twice through a sample with a complex transmission amplitude $H = Re^{i\phi}$. After being reflected from the mirrors, the two beams are recombined by the beam splitter to an intensity-sensitive detector. By performing multiple measurements of the intensity for varying displacements of the movable mirror, the spectral phase of the light, induced by the sample under inspection, can be extracted.

1.4.1 Common path interferometry

Interferometers are highly sensitive to environmental noise. When this noise is affecting differently the paths of the interferometer its performances are greatly decreased. That problem is largely suppressed in common-path interferometers, which are made such that the interfering beams travel along essentially the same paths. To do this, sophisticated optical manipulation schemes are required. Examples include the Sagnac interferometer [125], Zernike phase-contrast interferometer [126], the point diffraction interferometer [127], and various schemes for quantitative phase imaging [128].

1.5 Methods

1.5.1 Experimental methods

Microscopic spectroscopy

For linear characterization of the metasurfaces studied at this thesis, a microscopic spectroscopy setup was used, as depicted in Figure 1.5. The setup comprised a supercontinuum illumination source (NKT Photonics, SuperK compact), half-wave plate ($\lambda/2$) and a polarizer (P) to control the beam power and polarization, sample on a motorized rotational stage (Thorlabs PRM1Z8), objective lens (Obj.), tube lens (TL), iris at the image plane, $4f$ system, polarizer (P) and an imaging spectrometer (IS) with a cooled back-illuminated EMCCD detector (Andor Shamrock 303i, Newton 970).

The measurements procedure started with obtaining a focused and clear magnified image of the studied sample. The image was taken with the IS in a standard camera mode and with an open iris. Then, the iris was adjusted to transmit only light passing through the studied sample, and the IS was used in a spectrometer mode. For measurements that exceeded the spectral range of the IS ($\sim 200 - 1050 \text{ nm}$), fiber coupled spectrometer for the near-infrared (Ocean Optics NIRQ512, spectral range $900 - 1700 \text{ nm}$) was used. Transmission measurements were calculated according to $T = \frac{I_{\text{sample}} - I_{\text{background}}}{I_{\text{reference}} - I_{\text{background}}}$, where I_{sample} , $I_{\text{reference}}$ and $I_{\text{background}}$ are the spectrometer counts for light passing through the sample, reference, and with no light, respectively. The reference measurements were performed on the substrate without the metasurface. The background counts were reduced by cooling the detector of the spectrometer. Measurements with good signal to noise ratios were achieved by adjusting the acquisition rates, source power, and the spectrometer temperature to assure negligible influence of $I_{\text{background}}$.

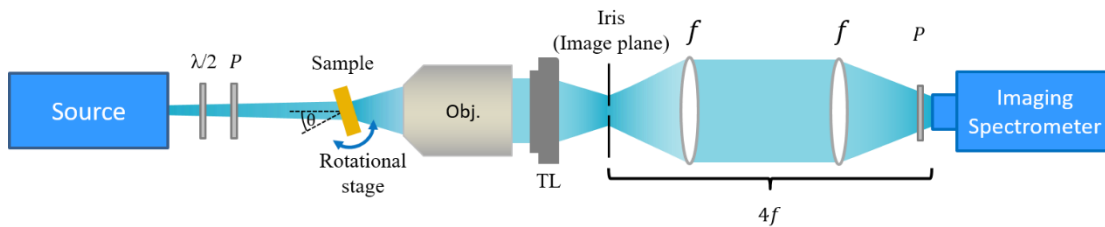


Figure 1.5. Spectroscopy microscope setup used throughout this thesis. The setup comprised illumination source, half-wave plate ($\lambda/2$) and a polarizer (P) to control the beam intensity and polarization, sample on a rotational stage, objective lens (Obj.), tube lens (TL), iris at the image plane, $4f$ system, polarizer (P) and an imaging spectrometer.

Second harmonic generation measurements

The SHG measurements were performed in the setup shown in Figure 1.5, with few modifications. First, long-pass and short-pass filters were placed prior to the sample and between the tube lens and $4f$ system, respectively. The spectral range operation of the filters was adjusted to block residual SH on the incident beam, and FF from entering the spectrometer. Second, a lens of $f = 200 \text{ mm}$ was used to slightly focus the incident beam on the sample. In addition, the FF source for the SHG measurements was a tunable pulsed femtosecond OPO pumped by a Titanium Sapphire laser (Chameleon OPO VIS, pulse width $\sim 140 \text{ fs}$, repetition rate 80 MHz , spectral range $1000 - 1600 \text{ nm}$). The incident beam waist was focused down to minimal spot size of $\sim 50 \mu\text{m}$ with an average power going up to $\sim 200 \text{ mW}$. The short pulses, and therefore the high peak power, used for excitation (up to $\sim 20 \text{ kW}$), ensured strong SH signal from the metasurfaces.

1.5.2 Numerical simulations

In this thesis, mainly two types of numerical electromagnetic simulations were used: CDA in the frequency domain and finite-difference time-domain (FDTD). Together, these simulation tools enabled detailed exploration of the studied dynamics. For example, in the CDA it is natural to separately investigate the role of the single particle and the array response, and to differentiate between the applied and scattered fields. On the other hand, full-wave FDTD simulations enable also studying the complex field distributions on each particle and relaxing the dipole-like response assumption of the CDA. Detailed description of the CDA method is brought in section 0. Here, we shortly review the working principle of the FDTD, along with specific implementations used to capture the collective response of the studied plasmonic metasurfaces. Thorough description and analysis of the FDTD method can be found in several textbooks [129–131].

The FDTD full-wave electromagnetic simulations were performed by a commercially available softer package (Lumerical FDTD). They enabled analyzing the near- and far-fields optical response of the studied resonant geometries over a broadband range, within reasonable simulation times. The idea of the FDTD algorithm is to solve the time-dependent Maxwell equations iteratively by discretizing time and space and replacing the associated derivatives by their central difference approximations. The basic operation principle can be demonstrated by considering the simplifying 1D case. Considering a dielectric medium described by permittivity ϵ and permeability μ , we start with Faraday's and Ampere's equations⁴:

⁴ Section 1.5.2 is written in SI system of units.

$$\begin{aligned}
-\mu\partial_t\mathbf{H} &= \nabla \times \mathbf{E} \\
\epsilon\partial_t\mathbf{E} &= \nabla \times \mathbf{H}
\end{aligned}
\tag{1.38}$$

The notation ∂ indicates a partial derivative. Considering a 1D space with variations only in the x direction, and assuming electric and magnetic fields only with y and z components, respectively, Eqs. (1.38) become:

$$\begin{aligned}
\mu\partial_t H_y &= \partial_x E_z \\
\epsilon\partial_t E_z &= \partial_x H_y
\end{aligned}
\tag{1.39}$$

Next, we discretize time and space of the sampled fields according to the following notations:

$$\begin{aligned}
E_z(x, t) &= E_z(m\Delta x, q\Delta t) = E_z^q[m] \\
H_y(x, t) &= H_y(m\Delta x, q\Delta t) = H_y^q[m]
\end{aligned}
\tag{1.40}$$

Where Δx and Δt are the spatial and temporal steps size, respectively. Accordingly, the indices m and q are integers that indicate the spatial and temporal location. The spatial and temporal steps satisfy $\Delta t \leq \frac{\Delta x}{\sqrt{d}c_0}$, with d being the number of dimensions, according to Courant Condition [129–131], to ensure numerical stability of the algorithm. Next, the derivatives in Eqs. (1.39) are replaced by their central differences. The points in which these derivatives are estimated are chosen on a staggered grid to enable iterative solution. In the 3D case, the Yee grid is commonly used [132]. In the 1D case, this step results in the following approximations to Eqs. (1.39):

$$\begin{aligned}
\mu \frac{H_y^{q+\frac{1}{2}}[m+\frac{1}{2}] - H_y^{q-\frac{1}{2}}[m+\frac{1}{2}]}{\Delta t} &= \frac{E_z^q[m+1] - E_z^q[m]}{\Delta x} \\
\epsilon \frac{E_z^{q+1}[m] - E_z^q[m]}{\Delta t} &= \frac{H_y^{q+\frac{1}{2}}[m+\frac{1}{2}] - H_y^{q+\frac{1}{2}}[m-\frac{1}{2}]}{\Delta x}
\end{aligned}
\tag{1.41}$$

By rearranging terms, we obtain the update equations of the FDTD:

$$\begin{aligned}
H_y^{q+\frac{1}{2}}[m+\frac{1}{2}] &= H_y^{q-\frac{1}{2}}[m+\frac{1}{2}] + \frac{\Delta t}{\mu\Delta x} (E_z^q[m+1] - E_z^q[m]) \\
E_z^{q+1}[m] &= E_z^q[m] + \frac{\Delta t}{\epsilon\Delta x} \left(H_y^{q+\frac{1}{2}}[m+\frac{1}{2}] - H_y^{q+\frac{1}{2}}[m-\frac{1}{2}] \right)
\end{aligned}
\tag{1.42}$$

These equations show the interleaved calculation in space and time of the FDTD method. By solving first the top equation in (1.42) for every magnetic-field node, and then the bottom one for every electric-field node, and repeating this scheme iteratively, the fields can be calculated over space and time.

The above derivation shows the fundamental working principle of FDTD. In order to perform full 3D FDTD simulation of complex materials, many other issues should be addressed. Some important examples are the method in which energy is inserted to the simulation region, the perfectly matched layers (PMLs) or periodic boundary conditions, and oblique excitation source for broadband illumination. The commercial software used in this thesis implements advanced FDTD techniques and enables performing complex simulations with a graphical user's interface and additional user written scripts. Typical FDTD simulation configuration used throughout this thesis is shown in Figure 1.6. The orange frame indicates the box shaped FDTD region, in which the electromagnetic fields are solved. The top and bottom faces of this cube consist of PMLs, for finite boundary condition along the z direction. The four side faces of the cube consist of periodic boundary conditions, corresponding to the infinite extent of the simulated array along the x and y directions. Inside the FDTD region a source, reflection monitor, the nanoparticle, and transmission monitor are ordered as depicted with approximated locations as indicated on the left. Additional monitors, as near field monitor, were added when necessary. The blue and purple arrows of the source indicate the polarization and direction of excitation, respectively. In order to analyze specifically the zero-order reflection and transmission of the array the fields at the corresponding monitors were decomposed to plane waves and filtered accordingly.

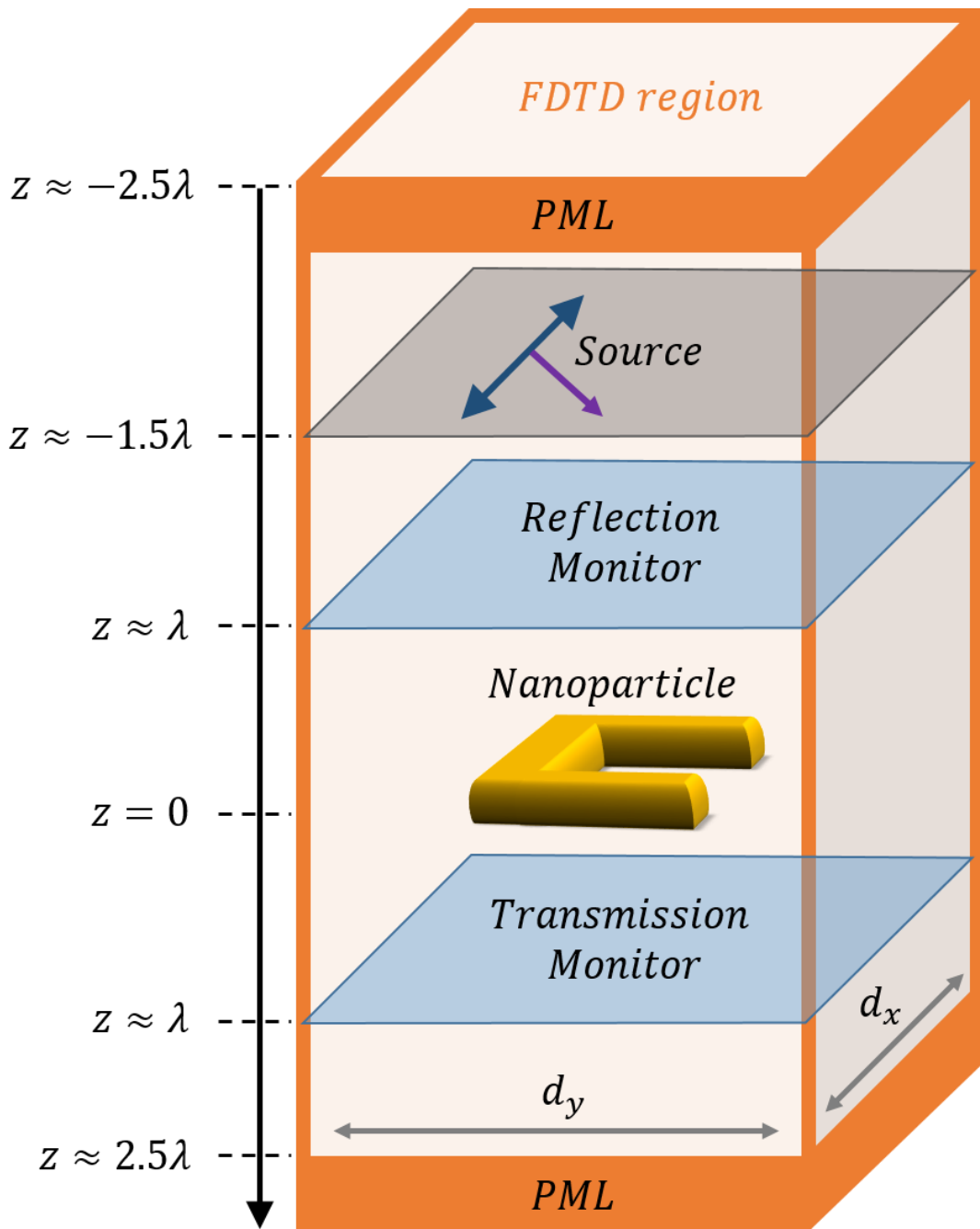


Figure 1.6. Typical FDTD simulation configuration of infinite plasmonic nanoparticle array. The orange frame indicates the cube shaped FDTD region, in which the electromagnetic fields are solved. The top and bottom faces of this cube consist of PMLs for finite boundary condition along the z direction. The four side faces of the cube consist of periodic boundary conditions, corresponding to the infinite extent of the array along the x and y directions. Inside the FDTD region, a source, reflection monitor, the nanoparticle and transmission monitor are ordered as depicted with approximated locations as indicated on the left. Additional monitors, as near field monitor, were added when necessary. The blue and purple arrows of the source indicate the polarization and direction of excitation, respectively. The refractive index of the simulation region was uniform.

1.5.3 Fabrication techniques

The metasurfaces that are used throughout this work, were fabricated using standard electron beam lithography as depicted in Figure 1.7(a). The substrates that were used are commercially available 1mm thick glass, coated with ~20nm Indium-Tin oxide (ITO). The substrates were cleaned by immersion and sonication in Acetone, followed by immersion and sonication in isopropyl alcohol (IPA) and drying under N₂ flow. The clean substrates were spin-coated with polymethyl methacrylate (PMMA) A4 at 7000 RPM for 1 minute and baked at 180°C for 1 minute. The PMMA layer acts as photoresist in the lithography process. The PMMA changes its molecular structure when exposed to electron beam. Using E-beam writer, Raith 150 Two, the desired two-dimensional structure of the metasurface was patterned on the PMMA layer. We use 20kV acceleration voltage and 20 μ m size aperture to achieve the required resolution. The samples were developed in MIBK:IPA solution for 1 minute, in which the exposed PMMA is dissolved, and holes with the desired pattern remains in the resist layer. Thereafter, the metal layers are evaporated using an e-beam evaporator. The first 3 nm Titanium layer which acts as an adhesion layer is followed by a 37 nm layer of gold. The remaining resist is then dissolved in acetone, removing the metallic layers in the un-patterned regions. Figure 1.7(b) shows a scanning electron microscope image of a typical fabrication result.

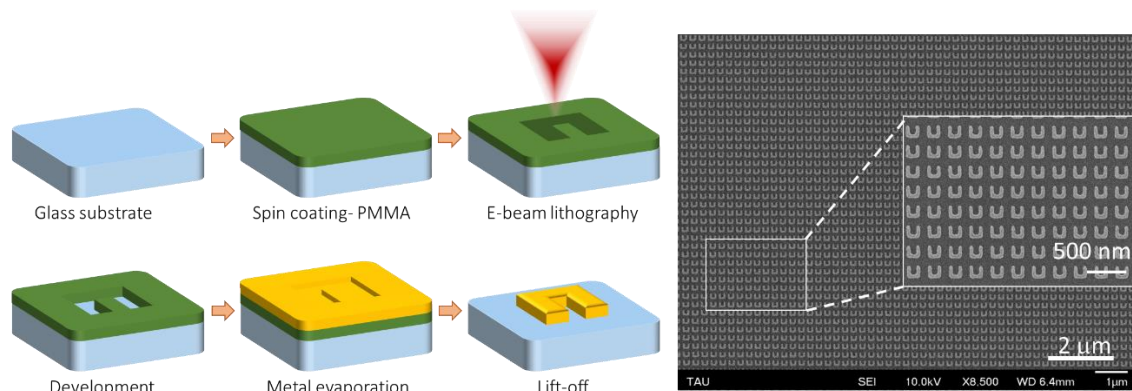


Figure 1.7. Metasurface fabrication [133]. (a) Fabrication technique. (b) Scanning electron microscope image of a fabricated SRR based nonlinear metasurface.

Following the described fabrication process, the samples were covered by immersion oil ($n = 1.51$), in order to obtain symmetric refractive index that enables the collective coherent effects to arise stronger. The covering was done by dropping type-F immersion oil on the sample and covering it with high-performance cover slip made from Schott D263 M glass.

Chapter 2 **PUBLISHED MANUSCRIPTS**

In this chapter, we present key results that were obtained over the course of the current PhD work, in the form of three peer-reviewed scientific papers. In the first paper, in section 2.1, we demonstrate a new resonant condition in the nonlinear regime supported by collective coherent interaction. In addition, we present a general theoretical framework to calculate the optical response of nanoparticle arrays, while accounting for the inter-particle interactions. In the second paper, in section 2.2, we show how collective scattering at the array may induce tunable transparency and slow light windows. Finally, in section 2.3, we present an original characterization method to dynamically and accurately obtain the spectral phase of a microscopic sample, either in reflection or transmission. The method enables flexible illumination conditions, and therefore is particularly advantageous for characterization of metasurfaces supporting collective coherent effects. The findings and developments presented in this chapter promote the understanding of collective effects in nanophotonics platforms and will potentially lead to new and exciting developments.

2.1 Nonlinear Surface Lattice Resonance in Plasmonic Nanoparticle Arrays



Nonlinear Surface Lattice Resonance in Plasmonic Nanoparticle Arrays

Lior Michaeli,^{1,2,*} Shay Keren-Zur,¹ Ori Avayu,¹ Haim Suchowski,^{2,3} and Tal Ellenbogen^{1,3}

¹*Department of Physical Electronics, Faculty of Engineering, Tel-Aviv University, Tel-Aviv 6779801, Israel*

²*Raymond and Beverly Sackler School of Physics & Astronomy, Tel-Aviv University, Tel-Aviv 6779801, Israel*

³*Center for Light-Matter Interaction, Tel-Aviv University, Tel-Aviv 6779801, Israel*

(Received 7 February 2017; published 16 June 2017)

We study experimentally second-harmonic generation from arrays of split-ring resonators at oblique incidence and find conditions of more than 30-fold enhancement of the emitted second harmonic with respect to normal incidence. We show that these conditions agree well with a nonlinear Rayleigh-Wood anomaly relation and the existence of a surface lattice resonance at the second harmonic. The existence of a nonlinear surface lattice resonance is theoretically confirmed by extending the coupled dipole approximation to the nonlinear case. We further show that the localized surface plasmon modes that collectively contribute to the surface lattice resonance are inherently dark modes that become highly bright due to the collective interaction.

DOI: 10.1103/PhysRevLett.118.243904

The artificial structural nonlinearity of metallic nanoparticles has been shown recently to enable nonlinear optical conversion with large effective nonlinear coefficients and in a variety of light manipulation schemes [1–10]. The interest in this field was stimulated by Sir John Pendry's prediction of high nonlinearities of structured materials [11]. The ability to obtain controlled nonlinearity by modifying the geometry of nanostructured materials opens the door to new fundamental studies in the realm of nonlinear optics. Several studies have been performed in recent years on trying to unveil the fundamental mechanisms for the measured artificial nonlinearity, mainly focusing on the single plasmonic nanoparticle [1,12,13]. It was shown that the strong quadratic nonlinearity originates from a combination of several effects [12–16], including local symmetry breaking on the interface of the nanostructure, the field enhancement due to excitation of localized surface plasmons resonances (LSPRs), asymmetry of the nanostructure which leads to efficient generation of nonlinear currents in a bright emission mode at the nonlinear output, and good spatial overlap between the localized modes participating in the nonlinear interaction.

It was also shown that the single nanostructure second-harmonic (SH) emission can be substantially modified when placed at an array of similar particles, with dependence on the lattice symmetry, orientation, and spacing [2,3,17]. In the subdiffraction regime, where the lattice spacing is sufficiently small to allow only zero-order forward and backward scattering of the fundamental frequency (FF) and the generated nonlinear beams, the net nonlinear optical response stems predominantly from the single particle nonlinearity, with near-field influenced variations due to the coupling between adjacent nanoparticles. Richer control of the optical response due to lattice structure can be achieved at the photonic regime of the SH, i.e., for lattice spacing that allows higher order diffraction of the SH wavelength [6]. While both regimes were much explored, the boundary in between, where the

SH light diffracts on the surface and long range collective interactions play a vital role in the optical response, has received less attention to date.

In the linear case, the condition of diffraction into a surface wave is known as the Rayleigh anomaly (RA) [18]. It was shown that arrays of metallic nanoparticles show sharp spectral features when the RA condition crosses a LSPR condition due to hybridization of the surface and localized resonances, which results in a so-called surface lattice resonance (SLR) [19–21]. In the past decade linear dynamics of SLRs have been explored extensively in lattices made out of different shapes of the constituent metallic nanostructures [19–25], different lattice symmetries [26], and at different frequency ranges from the visible and near infrared [19–27] to the THz frequencies [28,29]. They have also shown a potential in various fields including sensing [30], generation of coherent light sources [31], nonlocal coupling of the magneto-optical response of magnetic nanoparticles [32,33], and for solid-state lighting [34]. The case of nonlinear diffraction from metallic gratings has also been studied extensively [35–37]. However, the effect of SLRs on the nonlinear optical response of nanostructured materials has been studied only in a minute amount of works. In a recent work by Kauranen's group, tenfold enhancement of second-harmonic generation (SHG) was measured due to the existence of SLR at the FF [38]. Yet, the dynamics of the nonlinear response due to nonlinear collective interactions, i.e., SLR at the generated nonlinear mode, has remained unexplored.

In this study we experimentally demonstrate, for the first time to our knowledge, nonlinear SLR (NL-SLR) as a result of nonlinear RA (NL-RA) coupled to a localized mode in rectangular arrays of split-ring resonators (SRRs). We derive a theoretical expression for the NL-SLR condition by extending the coupled dipole approximation to the nonlinear case. The resulting extension for the collective nonlinear quadratic response takes a similar form to Miller's rule.

We also show analogy between our nonlinear results and the famous Wood's anomalies observed in 1902 for linear diffraction from metallic gratings [39]. Specifically, we observe sharp resonant response due to the nonlinear excitation of the surface lattice waves. This results in more than 30-fold enhancement of the SHG with respect to normal incidence, due to the coherent nonlinear interaction between the isolated nanoparticles as the condition of the NL-SLR is satisfied. In addition we observe abrupt change in the collected nonlinear light from both spectral sides of the calculated NL-RA condition. Finally, we show that the NL-SLR and its corresponding linear SLR rise from hybridization of a lattice mode and a dark localized surface plasmon (LSP) mode, in contrast to most of the previous reports of SLRs [19–23,26–28], showing that the plasmonic mode that contributes to the SLR is a bright dipole mode.

To study the optical response associated with SLRs on nanoparticles arrays the coupled dipole approximation (CDA) [40,41] method is often used. This model aims to find the collective optical response through the presentation of effective polarizability of each of the particles in the presence of the array, α_{eff} , which is a function of the single particle polarizability α_s , its radiation pattern, and the array geometry. The polarization at the i th nanoparticle is

$$P_i = \alpha_s E_{\text{loc},i}, \quad (1)$$

where $E_{\text{loc},i}$ is the local electric field at the i th particle location, which is composed of the applied field, E_{app} , and the scattered field from all other dipoles,

$$E_{\text{loc},i} = E_{\text{app}} + \sum_{j \neq i} A_{ij} \alpha_s E_{\text{loc},j}. \quad (2)$$

A_{ij} is the dipole interaction matrix that depends on geometrical parameters and on the wave vector and describes the interaction between the i th and j th dipoles. Considering higher multipole interactions can be done by modifying A_{ij} accordingly. By substituting Eq. (2) into Eq. (1) a set of linear equations can be attained, which can be solved numerically to obtain the polarization at each array site. At the specific case of normal incidence, the above relations can be simplified by assuming that the

local electric fields at all array sites are the same, $E_{\text{loc},i} = E_{\text{loc},j} \equiv E_{\text{loc}}$. Then by defining the retarded dipole sum as $S \equiv \sum_{j \neq i} A_{ij}$, the expression for the local field is obtained:

$$E_{\text{loc}} = \frac{E_{\text{app}}}{1 - S\alpha_s}, \quad (3)$$

where S is a complex parameter that has a resonance in the vicinity of the RAs condition. By requiring that the interparticle influence will be taken into account through effective polarizability, i.e., fulfilling the relation $P_i = \alpha_{\text{eff}} E_{\text{app}}$, we get

$$\alpha_{\text{eff}} = \frac{\alpha_s}{1 - S\alpha_s}. \quad (4)$$

From this formula it is possible to obtain insights on the SLR condition. We expect a strong response at the vicinity of the LSPR as a result of the proportionality of the array polarizability to the single particle polarizability. In addition, when the real part of $1/\alpha_s - S$ vanishes we expect resonance due to the lattice effect.

Here, we extend the above linear derivation to the nonlinear case of three-wave mixing (TWM) and introduce an expression for the effective second-order nonlinear polarizability, β_{eff} , which accounts for the array effect. For an array being irradiated with two light beams of frequencies ω_1 and ω_2 the polarization at $\omega_3 = \omega_1 \pm \omega_2$ of the i th nanoparticle can be expressed as

$$P_i(\omega_3) = \frac{1}{2} \beta_s E_{\text{loc},i}(\omega_1) E_{\text{loc},i}(\omega_2) + \alpha_s E_{\text{loc},i}(\omega_3), \quad (5)$$

where, β_s is the single particle second-order nonlinear polarizability. $E_{\text{loc},i}(\omega_k)$ for $k = 1, 2$ follows the same relation as in Eq. (2) and $E_{\text{loc},i}(\omega_3)$ is composed of the scattered light at ω_3 from all the $j \neq i$ lattice sites,

$$E_{\text{loc},i}(\omega_3) = \sum_{j \neq i} A_{ij}(\omega_3) p_j(\omega_3). \quad (6)$$

Considering again the case of normal incidence and requiring that the array effect will be manifested through the presentation of effective quadratic polarizability, we get

$$\beta_{\text{eff}}(\omega_3; \omega_1, \omega_2) = \frac{\beta_s(\omega_3; \omega_1, \omega_2)}{[1 - S(\omega_1)\alpha_s(\omega_1)][1 - S(\omega_2)\alpha_s(\omega_2)][1 - S(\omega_3)\alpha_s(\omega_3)]}. \quad (7)$$

This result for the nonlinear polarizability β_{eff} takes a similar form to that of the quadratic susceptibility described by the local Miller's rule [42,43], whereas the localized resonances that give rise to the enhanced $\chi^{(2)}$ in Miller's rule are replaced by the linear and nonlinear SLR conditions, $\text{Re}\{S(\omega_k)\alpha_s(\omega_k)\} = 1$ and $\text{Re}\{S(\omega_3)\alpha_s(\omega_3)\} = 1$, respectively. Therefore, this result accounts for a more general case where, in addition to local resonances, there

can also be collective lattice resonances. When the lattice spacing affords only diffraction at ω_3 we expect $S(\omega_k) \approx 0$ and enhancement of the nonlinear polarizability will be when the LSPR at ω_3 and the NL-RA, manifested by $\alpha_s(\omega_3)$ and by $S(\omega_3)$, respectively, will get into close proximity.

To find the condition of NL-RA that describes the nonlinear generation of waves traveling at a grazing angle

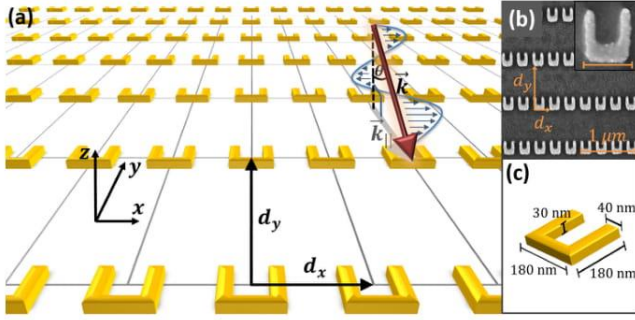


FIG. 1. (a) Illustration of the studied SRRs array, incident angle, and polarization. The incident light wave vector lies in the y - z plane at an angle θ relative to the normal to the surface. (b) Scanning electron microscope image of the fabricated sample. The inset shows a single SRR. (c) Illustration of the physical dimensions of each SRR.

to the surface, the linear RA condition can be generalized to the nonlinear case. The linear condition stated in terms of momentum conservation is given by

$$\vec{k}_{\parallel} + \vec{G}_{m_1, m_2} = \vec{k}_s, \quad (8)$$

where \vec{k}_{\parallel} is parallel to the surface component of the incident wave vector $\vec{k} = [2\pi \cdot n(\lambda)/\lambda]\hat{k}$, $n(\lambda)$ is the refractive index, $\vec{G}_{m_1, m_2} = m_1\vec{b}_1 + m_2\vec{b}_2$ is a general reciprocal lattice vector that is a linear combination of the primitive lattice vectors, and $\vec{k}_s = |\vec{k}|\hat{k}_s$ is the surface scattered wave. The vectors \hat{k} and \hat{k}_s are unit vectors specifying the directions of the incident wave vector and the scattered surface wave vector.

Extending the RA momentum conservation requirement to the nonlinear Raman-Nath diffraction regime [44] for TWM gives

$$(\vec{k}_1)_{\parallel} + (\vec{k}_2)_{\parallel} + \vec{G}_{m_1, m_2} = \vec{k}_{3, s}, \quad (9)$$

where k_i ($i = 1, 2, 3$) corresponds to the beam at ω_i .

In the particular case of SHG studied here $\omega_1 = \omega_2 = \omega$ and $\omega_3 = 2\omega$. In addition, the incident angle θ varies only in the y - z plane [Fig. 1(a)], and $m_1 = 0$, which sets $\vec{G}_{m_1, m_2} = m_2(2\pi/d_y)\hat{y}$, where d_y is the y spacing of the lattice. In this case the wavelengths satisfying the linear RAs condition of spatial order $\langle 0, m_2 \rangle$ are

$$\lambda^{(0, m_2)} = \frac{n(\lambda)d_y}{|m_2|} [1 - \text{sgn}(m_2) \sin(\theta)]. \quad (10)$$

Relating to the same configuration the FF wavelengths that satisfy the NL-RA condition are

$$\lambda_{\text{FF}}^{(0, m_2)} = \frac{2d_y}{|m_2|} [n(\lambda_2) - n(\lambda_1) \text{sgn}(m_2) \sin(\theta)]. \quad (11)$$

In order to experimentally examine the nonlinear interaction due to NL-RA and NL-SLR we fabricated a

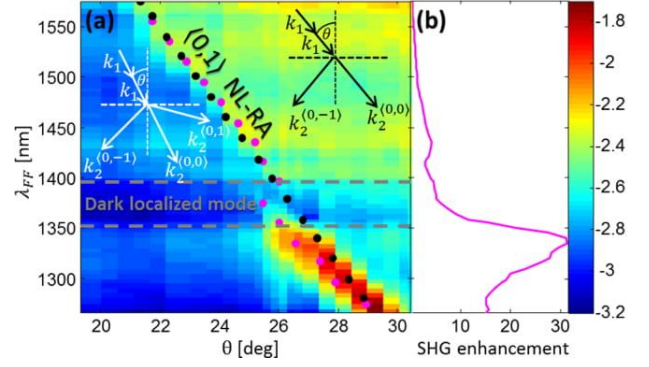


FIG. 2. Second-harmonic emission, NL-RA and NL-SLR. (a) Log scale of the measured zero-order SHG emission vs the FF wavelengths and the incident angle. The black dots indicate the NL-RA of $\langle 0, 1 \rangle$ order calculated according to Eq. (11), and the magenta dots indicate the strongest measured response at each wavelength. The arrows diagrams demonstrate the existing diffraction modes in both sides of the NL-RA. (b) SHG enhancement along the position of strongest measured emission relative to normal incidence.

$50 \mu\text{m} \times 50 \mu\text{m}$ rectangular array of gold SRRs with subwavelength x spacing of $d_x = 270$ nm and larger y spacing of $d_y = 800$ nm, which support the existence of the NL-RA, without supporting the linear RA of the FF [Figs. 1(a) and 1(b)]. Each SRR had a 180 nm base length, 180 nm arms length, 40 nm arms width, and thickness of 30 nm [Fig. 1(c)]. The sample was covered by immersion oil ($n = 1.51$), to obtain a symmetric refractive index environment, which enables the SLRs to arise stronger [19], and was placed on a rotational stage. A tunable femtosecond source (~ 140 fs width at 80 MHz) was used as the FF, spanning wavelengths between 1270–1580 nm (see Supplemental Material [45]). Spectral filters blocked residual SH from the OPO, and a half-wave plate and polarizer were used to control the power and polarization of the input FF. The incident beam waist was $\sim 50 \mu\text{m}$ with an average power of ~ 200 mW. The emission from the sample was collected with an X20 objective lens, filtered to remove transmitted FF, and directed to an imaging spectrometer. The SH emission was verified to origin from the array and not from the substrate.

First, we examined the zero-order SH emission spectra from the array [Fig. 2(a)]. The incident light was x polarized and the collected SH light was y polarized. The SH spectra show different magnitudes of collected SH due to different physical phenomena related to $\langle 0, 1 \rangle$ NL-RA, $\langle 0, 1 \rangle$ NL-SLR, and a dark LSP mode.

The $\langle 0, 1 \rangle$ NL-RA, calculated according to Eq. (11), is marked by the black dots in Fig. 2(a). We see two separate regimes for wavelengths longer than ~ 1400 nm, distinguished by the NL-RA condition. The region on the right-hand side of the plot, where $2(k_1)_{\parallel} + G_{0,1} > k_2$, shows about twice as bright SH compared to the region on the left-hand

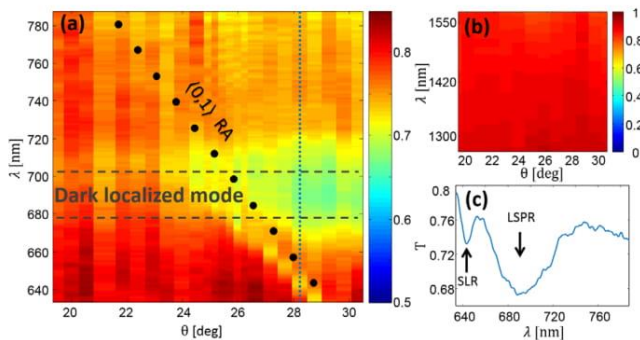


FIG. 3. Linear transmission measurements. Angle and wavelength dependent zero-order transmission of the sample at (a) the SH wavelengths range and y polarization, and (b) the FF wavelengths range and x polarization. The black dots at (a) indicate the $(0, 1)$ RA order calculated according to Eq. (10). (c) A cross section of the transmission at (a) for angle of 28.3 degrees [blue dashed line in (a)].

side. This difference in collected SH can be attributed to rearrangements of energy distribution between the radiating modes as the $(0, 1)$ mode onsets or disappears, in analogy to Wood's linear observation from 1902 [15]. For wavelengths shorter than ~ 1350 nm strong sharp resonance behavior (~ 35 nm full width at half maximum) is shown at the vicinity of the NL-RA condition. We have found that this resonance behavior is the nonlinear analogue to the traditional linear SLR. It can be seen that this NL-SLR deviates from the calculated NL-RA for wavelengths approaching 1350 nm. This is due to the coupling of the nonlinear lattice mode to a nonlinear dark localized mode that exists in the wavelength range of ~ 1350 – 1400 nm. The interaction between the lattice and localized modes leads to enhancement of the collected SH compared to normal incidence that reaches a peak value of 31 around FF wavelength of 1340 nm [Fig. 2(b)].

To demonstrate that the observed phenomena are NL-RA and NL-SLR we measured also the linear interaction at FF and SH wavelength regimes. In Fig. 3(b) we show the linear angle dependent spectral transmittance at the FF wavelength regime for x -polarized light. This transmittance reveals no resonant behavior, with uniform values of $\sim 90\%$ all over the region of interest. The transmission spectra at the SH range [Fig. 3(a)] for y -polarized light reveals two different resonant dips in transmission. One relatively broad appearing around constant wavelengths of ~ 675 – 700 nm, and another narrow dispersive resonance [Fig. 3(c)]. It can be seen that the narrow mode exists slightly below the marked $(0, 1)$ linear RA condition and bends when reaching the broad mode. This optical response is due to coupling between the localized and lattice resonances and existence of a hybrid SLR mode. Here we find that in contrast to most of the previous reports of SLRs [19–23, 26–28], the interacting localized mode is not a bright dipole mode but a dark [24] double-quadropole (DQ) mode on the SRR's arms [Fig. 4(a)]. This dark mode can be accessed only at oblique incidence, as seen in

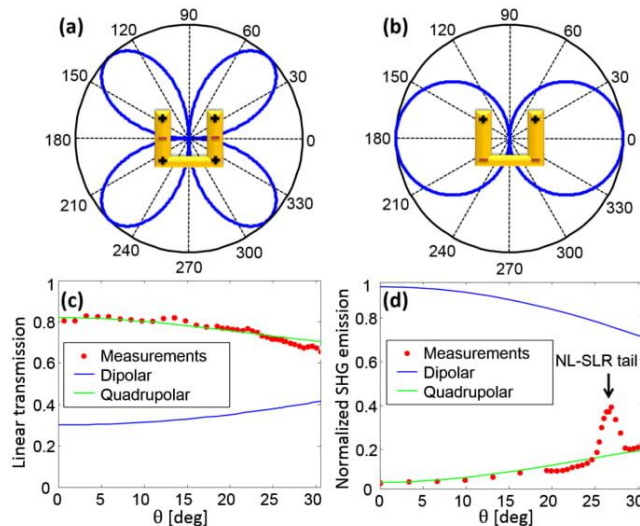


FIG. 4. Schematic charge distribution and calculated far-field radiation patterns of (a) quadrupole and (b) dipole modes, in the x - y plane. These modes exist in our nanostructures in wavelength range of 675–700 and 950–1070 nm, respectively. Angle dependent (c) transmission and (d) SH emission was calculated for quadrupole (green) and dipole (blue) modes. The measured data (red dots) agree with the behavior of a quadrupole mode for both cases. The measured data in (c) and (d) were taken by averaging the response at the wavelengths range of the quadrupole mode.

Fig. 3(a), in agreement with theory. We believe that the participation of the dark mode in the collective surface response is enabled by coupling of the dark mode to z -oriented dipoles in the nanoparticles as discussed in Refs. [46,47].

The dark quadrupole nature of the LSP can be deduced from the measured linear and nonlinear angle dependent behavior of the LSPR. To verify it, we compare the experimental linear and nonlinear measurements to the theoretical far-field dynamics of perfect quadrupole and dipole modes. Figures 4(a) and 4(b) illustrate schematically the charge distribution of the quadrupole and dipole modes on the arms of the SRR, respectively. Far-field radiation patterns of perfect quadrupole and dipole modes are also shown in Figs. 4(a) and 4(b), respectively. These theoretical radiation patterns were used to calculate the expected linear transmission and nonlinear emission as a function of the incidence angle. The comparison between the theoretical calculations and measurements is shown in Figs. 4(c) and 4(d) for the linear and nonlinear cases, respectively. This comparison shows a good agreement with the behavior of a dark quadrupole mode. The deviation of the fitted quadrupole curve from the measurements at the angle range of ~ 25 – 28 degrees in Fig. 4(d) is due to the fact that the mode dependent calculations do not account for the coherent coupling effect.

In addition, we performed finite element simulations (Comsol) to examine numerically the excited modes dynamics. The dielectric permittivity of gold was taken

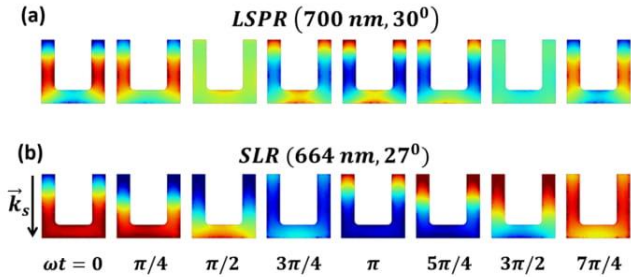


FIG. 5. Simulations of the two different resonance excitations. Surface charge distribution along the SRRs over the full optical cycle is shown in (a) at the quadrupole LSPR and in (b) at the SLR.

from Ref. [48] and for the surrounding medium we used $\epsilon = 2.3$. Periodic boundary conditions and perfectly matched layers were set along the array transverse and longitudinal directions, respectively. Figure 5(a) shows the surface charge distribution along the optical cycle on the SRR for oblique excitation at 30° and wavelength of 700 nm, which supports the excitation of a localized DQ mode. It can be seen that the evolution of the charge distribution along the optical cycle in this case shows a standing wave behavior as expected from a LSP. Figure 5(b) presents the case of excitation in the SLR conditions (angle 27° , wavelength 644 nm) which shows the transition to a propagating wave behavior with wavelength λ/n .

To conclude, we have demonstrated experimentally and theoretically the existence of NL-RA and NL-SLR in arrays of metal nanoparticles. The NL-RA condition is followed by abrupt variation in the brightness of the collinear SHG that agrees with energy rearrangement due to vanishing or onsets of the nonlinear diffraction orders. Furthermore, the NL-SLR leads to very strong and spectrally narrow enhancement of the collinear SHG. Our theoretical derivation shows that the nonlinear polarizability of the nanoparticles in the array takes a form which is similar to Miller's rule and resonantly depends on the collective nonlinear interaction. Finally, we also show that in the current case, the localized mode that hybridizes with the lattice mode to generate the NL-SLR is inherently a dark mode, which is accessible only at oblique incidence. This work reveals new dynamics of nonlinear-nonlocal interactions in arrays of metallic nanoparticles and opens the door to use such nonlocal interactions to strongly modify and enhance the effective nonlinearity of these artificial optical materials. The specific effect studied here of NL-SLR on SHG can be extended to study and enhance TWM processes and higher order nonlinear processes, which may find use in improving nanoscale multiphoton imaging, nonlinear conversion, nonlinear sensing and spectroscopy.

This publication is part of a project that has received funding from the European Research Council (ERC) under the European Union's Horizon 2020 research and

innovation program (Grant Agreement No. 715362), and by the Israel Science Foundation (ISF) through Grants No. 1331/13 and No. 1433/15. S. K. acknowledges support from the Tel-Aviv University Center for Renewable Energy President Scholarship for Outstanding Ph.D. Students and the support from the Israel Ministry of Science, Technology and Space Scholarship for Ph.D. student in the field of applicative sciences.

*liormic1@mail.tau.ac.il

- [1] M. W. Klein, C. Enkrich, M. Wegener, and S. Linden, *Science* **313**, 502 (2006).
- [2] S. Linden, F. B. P. Niesler, J. Förstner, Y. Grynko, T. Meier, and M. Wegener, *Phys. Rev. Lett.* **109**, 015502 (2012).
- [3] J. Butet, P.-F. Brevet, and O. J. F. Martin, *ACS Nano* **9**, 10545 (2015).
- [4] N. Segal, S. Keren-Zur, N. Hendler, and T. Ellenbogen, *Nat. Photonics* **9**, 180 (2015).
- [5] V. K. Valev, X. Zheng, C. G. Biris, A. V. Silhanek, V. Volskiy, B. De Clercq, O. A. Aktsipetrov, M. Ameloot, N. C. Panoiu, G. A. E. Vandenbosch, and V. V. Moshchalkov, *Opt. Mater. Express* **1**, 36 (2011).
- [6] N. I. Zheludev and V. I. Emel'yanov, *J. Opt. A* **6**, 26 (2004).
- [7] S. Campione, A. Benz, M. B. Sinclair, F. Capolino, and I. Brener, *Appl. Phys. Lett.* **104**, 131104 (2014).
- [8] S. Kruk, M. Weismann, A. Y. Bykov, E. A. Mamonov, I. A. Kolmychek, T. Murzina, N. C. Panoiu, D. N. Neshev, and Y. S. Kivshar, *ACS Photonics* **2**, 1007 (2015).
- [9] S. Keren-Zur, O. Avayu, L. Michaeli, and T. Ellenbogen, *ACS Photonics* **3**, 117 (2016).
- [10] A. Rose, D. Huang, and D. R. Smith, *Phys. Rev. Lett.* **107**, 063902 (2011).
- [11] J. B. Pendry, A. J. Holden, D. J. Robbins, and W. J. Stewart, *IEEE Trans. Microwave Theory Tech.* **47**, 2075 (1999).
- [12] C. Ciraci, E. Poutrina, M. Scalora, and D. R. Smith, *Phys. Rev. B* **85**, 201403 (2012).
- [13] K. O'Brien, H. Suchowski, J. Rho, A. Salandrino, B. Kante, X. Yin, and X. Zhang, *Nat. Mater.* **14**, 379 (2015).
- [14] M. Kauranen and A. V. Zayats, *Nat. Photonics* **6**, 737 (2012).
- [15] C. Ciraci, E. Poutrina, M. Scalora, and D. R. Smith, *Phys. Rev. B* **86**, 115451 (2012).
- [16] S. Roke, M. Bonn, and A. V. Petukhov, *Phys. Rev. B* **70**, 115106 (2004).
- [17] H. Husu, R. Siikanen, J. Mäkitalo, J. Lehtolahti, J. Laukkanen, M. Kuittinen, and M. Kauranen, *Nano Lett.* **12**, 673 (2012).
- [18] L. Rayleigh, *Proc. R. Soc. A* **79**, 399 (1907).
- [19] B. Auguié and W. L. Barnes, *Phys. Rev. Lett.* **101**, 143902 (2008).
- [20] Y. Chu, E. Schonbrun, T. Yang, and K. B. Crozier, *Appl. Phys. Lett.* **93**, 181108 (2008).
- [21] V. G. Kravets, F. Schedin, and A. N. Grigorenko, *Phys. Rev. Lett.* **101**, 087403 (2008).
- [22] A. I. Väkeväinen, R. J. Moerland, H. T. Rekola, A. P. Eskelinen, J. P. Martikainen, D. H. Kim, and P. Törmä, *Nano Lett.* **14**, 1721 (2014).

- [23] I. De Leon, M. J. Horton, S. A. Schulz, J. Upham, P. Banzer, and R. W. Boyd, *Sci. Rep.* **5**, 13034 (2015).
- [24] A. D. Humphrey, N. Meinzer, T. A. Starkey, and W. L. Barnes, *ACS Photonics* **3**, 634 (2016).
- [25] Z. Li, S. Butun, and K. Aydin, *ACS Nano* **8**, 8242 (2014).
- [26] A. D. Humphrey and W. L. Barnes, *Phys. Rev. B* **90**, 075404 (2014).
- [27] S. R. K. Rodriguez, A. Abass, B. Maes, O. T. A. Janssen, G. Vecchi, and J. Gómez Rivas, *Phys. Rev. X* **1**, 021019 (2011).
- [28] M. Manjappa, Y. K. Srivastava, and R. Singh, *Phys. Rev. B* **94**, 161103 (2016).
- [29] M. C. Schaafsma, A. Bhattacharya, and J. G. Rivas, *ACS Photonics* **3**, 1596 (2016).
- [30] B. D. Thackray, V. G. Kravets, F. Schedin, G. Auton, P. A. Thomas, and A. N. Grigorenko, *ACS Photonics* **1**, 1116 (2014).
- [31] W. Zhou, M. Dridi, J. Y. Suh, C. H. Kim, D. T. Co, M. R. Wasielewski, G. C. Schatz, and T. W. Odom, *Nat. Nanotechnol.* **8**, 506 (2013).
- [32] N. Maccaferri, X. Inchausti, A. García-Martín, J. C. Cuevas, D. Tripathy, A. O. Adeyeye, and P. Vavassori, *ACS Photonics* **2**, 1769 (2015).
- [33] M. Kataja, T. K. Hakala, A. Julku, M. J. Huttunen, S. van Dijken, and P. Törmä, *Nat. Commun.* **6**, 7072 (2015).
- [34] G. Lozano, D. J. Louwers, S. Rk Rodríguez, S. Murai, O. Ta Jansen, M. A. Verschuuren, and J. Gó Mez Rivas, *Light Sci. Appl.* **22**, e66 (2013).
- [35] G. S. Agarwal and S. S. Jha, *Phys. Rev. B* **26**, 482 (1982).
- [36] A. C. R. Pipino, R. P. Van Duyne, and G. C. Schatz, *Phys. Rev. B* **53**, 4162 (1996).
- [37] M. E. Inchaussandague, M. L. Gigli, K. A. O'Donnell, E. R. Méndez, R. Torre, and C. I. Valencia, *J. Opt. Soc. Am. B* **34**, 27 (2017).
- [38] R. Czaplicki, A. Kiviniemi, J. Laukkanen, J. Lehtolahti, M. Kuittinen, and M. Kauranen, *Opt. Lett.* **41**, 2684 (2016).
- [39] R. W. Wood, *Philos. Mag. Ser. 5* **4**, 396 (1902).
- [40] L. Zhao, K. L. Kelly, and G. C. Schatz, *J. Phys. Chem. B* **107**, 7343 (2003).
- [41] F. J. García de Abajo, *Rev. Mod. Phys.* **79**, 1267 (2007).
- [42] C. Garrett and F. Robinson, *IEEE J. Quantum Electron.* **2**, 328 (1966).
- [43] The nonlinear polarizability-susceptibility relation is discussed in details in: R. W. Boyd, *Nonlinear Optics*, 3rd ed. (Academic Press, New York, 2008).
- [44] Y. Sheng, Q. Kong, W. Wang, K. Kalinowski, and W. Krolikowski, *J. Phys. B* **45**, 055401 (2012).
- [45] See Supplemental Material at <http://link.aps.org/supplemental/10.1103/PhysRevLett.118.243904> for a detailed description of the experimental setup and measurements.
- [46] M. J. Huttunen, K. Dolgaleva, P. Törmä, and R. W. Boyd, *Opt. Express* **24**, 28279 (2016).
- [47] W. Zhou and T. W. Odom, *Nat. Nanotechnol.* **6**, 423 (2011).
- [48] P. B. Johnson and R. W. Christy, *Phys. Rev. B* **6**, 4370 (1972).

Supplemental Material

Nonlinear Surface Lattice Resonance in Plasmonic Nanoparticles Arrays

Lior Michaeli^{1,2}, Shay Keren-Zur¹, Ori Avayu¹, Haim Suchowski^{2,3}, Tal Ellenbogen^{1,3}

¹ Department of Physical Electronics, Faculty of Engineering, Tel-Aviv University, Tel-Aviv 6779801, Israel

² Raymond and Beverly Sackler School of Physics & Astronomy, Tel-Aviv University, Tel-Aviv 6779801, Israel

³ Center for Light-Matter Interaction, Tel-Aviv University, Tel-Aviv 6779801, Israel

Experimental Setup and Measurements

The sample was covered by immersion oil ($n=1.51$), to obtain symmetric refractive index environment and was placed on a motorized rotational stage (Thorlabs PRM1Z8). Figure 1S below provides a detailed description of the experimental setup. A tunable pulsed femtosecond optical parametric oscillator pumped by a Titanium Sapphire laser (Chameleon OPO VIS, pulse width ~ 140 fs, repetition rate 80 MHz) was used as the fundamental frequency (FF) source spanning wavelengths in the range of 1270–1580 nm. Spectral filters blocked residual SH from the OPO, and a half-wave plate and polarizer were used to control the power and polarization of the input FF beam. The beam waist on the sample was ~ 50 μm with a typical average power of 200 mW (averaged and peak power densities of mW/cm^2 and MW/cm^2 respectively). The emission was collected with an objective lens (Mitutoyu NIR X20), filtered to remove transmitted FF beam, and directed to an imaging spectrometer with a cooled back-illuminated EMCCD detector (Andor Shamrock 303i, Newton 970). The SH emission was imaged on the CCD and it was verified that the emission originates from the array and not from the substrate.

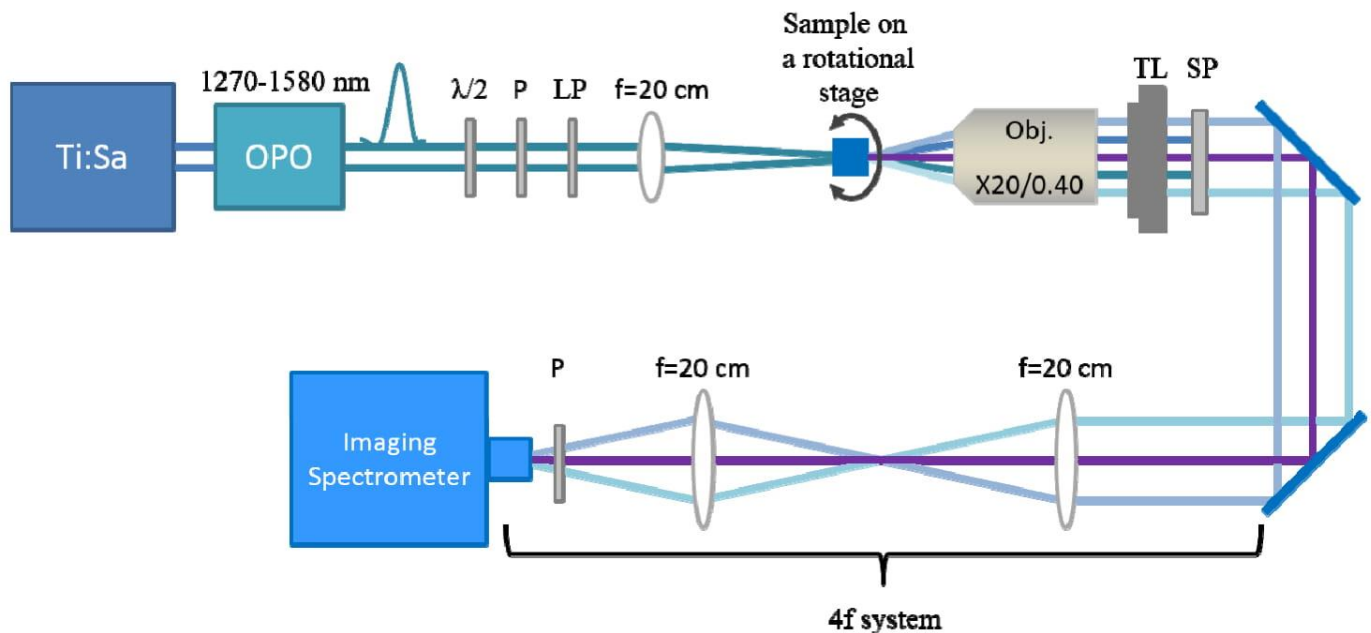


FIG. 1S. The experimental setup. Titanium Sapphire laser (Ti:Sa), optical parametric oscillator (OPO), half-wave plate ($\lambda/2$), polarizer (P), long-pass filter (LP), lens ($f=20$ cm), sample on a rotational stage, objective lens (Obj.), tube lens (TL), short-pass filter (SP), 4f system with $f=20$ cm, polarizer (p) and an imaging spectrometer.

2.2 Near-Infrared Tunable Surface Lattice Induced Transparency in a Plasmonic Metasurface

Near-Infrared Tunable Surface Lattice Induced Transparency in a Plasmonic Metasurface

Lior Michaeli,* Haim Suchowski, and Tal Ellenbogen

Collective coherent scattering at the surface of a plasmonic nanoparticle array is shown to induce tunable transparency windows at the localized plasmon band. Broadband phase measurements show that the enhanced transmission is accompanied by a large anomalous dispersion, which leads to a group delay as large as ~ 8 fs within only 40 nm thick sample. This effect occurs over a wide tunable spectral range of ~ 200 nm, and appears for two distinct counter-propagating surface waves. The experimental observations are in good agreement with calculations based on coupled dipole approximation (CDA) and with finite-difference time-domain (FDTD) simulations. This study opens the door for implementation in the fields of sensing, displays, optical buffering, tunable filtering, and nonlinear optics.

1. Introduction

Coherent scattering of light serves the basis to various optical phenomena, such as openings of optical bandgaps in photonic crystals,^[1] quasi-phase-matching of nonlinear optical processes,^[2] and the century-old Rayleigh anomaly (RA).^[3] Recently it was shown that in ordered arrays of nanoparticles, the coherent buildup of scattered light at the array plane can significantly alter the collective optical response. In the case of metallic nanoparticles, where localized surface plasmon resonances (LSPRs) dictate the absorption and scattering behavior, the simultaneous existence of LSPR with coherently scattered light at the surface of the array can lead to hybridized photonic-plasmonic resonances, known as surface lattice resonances (SLRs).^[4–6] These unique resonances have attracted much attention over the last decade. It was shown that the narrow spectral features that accompany the SLRs, along with their photonic

bandgaps behavior, make them attractive to various potential processes and applications, such as Bose–Einstein condensation at room temperature,^[7] enhanced nonlinearity,^[8] lasing,^[9] and sensing.^[10]

Electromagnetically induced transparency (EIT), which is a quantum coherent effect induced by strong interaction with a three-level resonant atomic media,^[11] has recently found its counterpart in micro- and nanostructured optical materials.^[12–20] This phenomenon, so called EIT-like effect, emerges due to the coupling of superradiant and subradiant modes of the system. The enhanced transmission is accompanied by


enhanced group delay of the light, which altogether may pave the way toward implementation of on-chip optical signal processing in the time domain and enhanced linear and nonlinear light-matter interactions. To date, most of the experimental demonstrations of EIT-like effects in metallic micro- and nanostructures rely on the coexistence of two bright and dark localized modes, which, by near-field coupling, cause drastic reduction of the bright mode extinction.^[12–14,21,22] Alternative approach to obtain EIT-like effect using plasmonics is by introducing delocalized modes into the system and relying on the destructive interference of either distributed-distributed modes or localized-distributed modes. The first mechanism, which resembles the origin of slow light near the band-edge of photonic crystals, was suggested and demonstrated in various schemes at different spectral ranges.^[23–25] Early demonstration of the second mechanism was done by Linden et al.,^[26] who showed suppression of extinction in a system composed of plasmonic array above a dielectric substrate that supports guided modes. Following this demonstration, the approach of relying on coupling between localized resonances and distributed waveguide modes has been proposed in several configurations.^[27–31] Nevertheless, hardly any experiment has studied the interesting effect of slow light induced by surface lattice resonances, nor have shown spectral tunability of the transparency window. Recently two groups have also studied lattice induced transparencies in the THz spectral range,^[32–34] where high transparency values and large group delays were obtained at normal incidence for specific operation frequency. Yet, in the optical range such studies have not been performed to date.

Here we experimentally demonstrate the formation of a near-infrared, spectrally tunable, narrow transparency window within a plasmonic absorptive band of split-ring resonators (SRRs) based metasurface. We experimentally show that the enhanced transmission is accompanied with high anomalous dispersion

L. Michaeli, Prof. T. Ellenbogen
Department of Physical Electronics
Faculty of Engineering
Tel Aviv University
Tel Aviv 6779801, Israel
E-mail: liormic1@mail.tau.ac.il

L. Michaeli, Prof. H. Suchowski
Raymond and Beverly Sackler School of Physics & Astronomy
Tel Aviv University
Tel Aviv 6779801, Israel

L. Michaeli, Prof. H. Suchowski, Prof. T. Ellenbogen
Center for Light-Matter Interaction
Tel Aviv University
Tel Aviv 6779801, Israel

 The ORCID identification number(s) for the author(s) of this article can be found under <https://doi.org/10.1002/lpor.201900204>

DOI: 10.1002/lpor.201900204

which leads to group delay as large as ~ 8 fs within only 40 nm thick sample. These experimental measurements are validated by finite-difference time-domain (FDTD) simulations. Moreover, we use the coupled dipole approximation (CDA) to obtain further insight on the nonlocal coupling dynamics in the system. Our analysis reveals that the intriguing effect of strong absorptionless interaction on the resonant plasmonic metasurface is attributed to a special case of photonic–plasmonic hybridization. We find that exactly when coherent scattering of light at the array plane occurs, that is, at the RA condition, equal magnitudes and opposite phases of the incident and scattered light leads to full electric-field cancelation at the nanoparticles' positions. The observed effects occur for two distinct counter-propagating surface waves and show tunability of the EIT-like behavior over a wide spectral range of ~ 200 nm. Interestingly, these effects occur only for S-polarized light, which therefore may render this phenomenon the complementary metamaterial behavior of the conventional Brewster angle.

2. Results and Discussion

2.1. Absorption-Less Band Predicted by the Coupled Dipole Approximation

To investigate the collective effects that lead to the appearance of SLR induced EIT-like phenomena we use the CDA. This simplified model captures the core physics behind the studied multi-particle coupling mechanism, and is able to predict and reproduce phenomenologically various related observations.^[4,8,10,35–39] The CDA takes into account the inter-particle scattering, and aims to find the effective polarizability, α_{eff} , of each individual particle. The resulting α_{eff} depends on the single particle polarizability α_s , the array geometry, the angular frequency of light ω , the refractive index of the ambient medium $n(\lambda)$, and the angle of incidence θ . In the case of a finite array, a set of linear equations needs to be solved to obtain each particle's effective polarizability,^[35,36] while for infinite array, as we consider here, a simple and insightful expression can be derived^[40]

$$\alpha_{\text{eff}} = \frac{1}{1/\alpha_s - S(\vec{k}_{\parallel})} \quad (1)$$

where $S(\vec{k}_{\parallel}) = \sum_{j \neq i} A_{ij} \cdot e^{-i\vec{k}_{\parallel} \cdot \vec{r}_j}$ is the array's incident angle-dependent structural factor, A_{ij} is the dipole Green function, \vec{k}_{\parallel} is the parallel to the surface component of the incident wavevector $\vec{k} = [2\pi \cdot n(\lambda)/\lambda] \hat{k}$ and \vec{r}_j is the location of the j th particle. The structural factor $S(\vec{k}_{\parallel})$ has peaks in its magnitude when there is a coherent buildup of its terms, that is, at the RAs condition: $\vec{k}_{\parallel} + \vec{G}_{m_1, m_2} = \vec{k}_s$, where $\vec{G}_{m_1, m_2} = m_1 \vec{b}_1 + m_2 \vec{b}_2$ is a general reciprocal lattice vector that is a linear combination of the primitive lattice vectors, and $\vec{k}_s = |\vec{k}| \hat{k}_s$ is the surface scattered wave. The vectors \hat{k} and \hat{k}_s are unity vectors specifying the directions of the incident and scattered surface wavevectors, respectively. From the expression in Equation (1) it can be seen that a

resonant response of α_{eff} , due to the plasmonic and photonic modes reflected by α_s and S respectively, can be determined by $\Delta \equiv \Re\{1/\alpha_s - S\}$, with dissipation determined by $\Gamma \equiv \Im\{1/\alpha_s - S\}$. These resonances of α_{eff} , known as SLRs, occur due to diffractive coupling of the particles at the array. Thackray et al.^[10] have pointed out that two types of SLRs can be distinguished; Type 1: occurs when the minimum of Δ is positive and then a single narrow Fano-type resonance appears at the RA condition. Type 2: occurs when the minimum of Δ is negative, and then the curve of $\Re\{1/\alpha_s\}$ intersects twice the curve of $\Re\{S\}$. At this case two unequal collective resonances of α_{eff} are observed, while in between these resonances, at the RA, reduced extinction gap may form.^[10] It was found that for 1D chains, one of the two resonances is strongly damped,^[4,10] which may affect the quality of the reduced extinction gap. While, as we show here, in 2D arrays this strong damping is significantly diminished. If the gap in-between the two resonances is narrow and deep enough, the Kramers–Kronig relations can be used to show that it is associated with a large negative dispersion and thus enhanced group delay.^[41,42] Therefore, as we show here, type 2 SLRs on 2D arrays have the potential for the realization of EIT-like and slow-light behavior.

To investigate the formation of EIT-like features in the system, we use the CDA and analyze the optical response of the array for four different cases presented in **Figure 1**. For each case we examine the interplay between α_s and S , and its associated influence on the collective optical extinction. We take the single particle polarizability to be a Lorentzian of the form $\alpha_s = A_0/(\omega_0^2 - \omega^2 + i\gamma\omega)$ with amplitude $A_0 = 5.2 \times 10^{14} \text{ cm}^3 \text{ s}^{-2}$, resonance angular frequency $\omega_0 = 2\pi c/\lambda_0$, resonance free space wavelength $\lambda_0 = 868$ nm, angular frequency $\omega = 2\pi c/\lambda$, where c is the speed of light, and damping constant $\gamma = 382 \text{ THz}$. The damping constant here accounts for both radiative and non-radiative losses. The ambient medium refractive index is taken to be $n = 1.51$, and the array x - and y -spacings are $d_x = 270$ nm and $d_y = 800$ nm, respectively. The angle of incidence is set to be $\theta = 26^\circ$, so that the $\langle 0, -2 \rangle$ RA condition will occur at $\lambda_{\langle 0, -2 \rangle}^{\text{RA}} \approx 869$ nm, and therefore will coincide with the LSPR centered around λ_0 .

In **Figure 1a–c**, we use the above parameters to calculate the response of a 1D particle chain arranged along the y -direction (with spacing $d_y = 800$ nm). The extinction cross section of each particle in the array is calculated by $\sigma_{\text{ext}} = 4\pi k \cdot \Im\{\alpha_{\text{eff}}\}$. For convenience we present the normalized extinction $C_{\text{ext}} = \sigma_{\text{ext}}/\sigma_0$ where $\sigma_0 = d_x d_y \cos(\theta)$ is the angle-dependent area of a unit cell, and d_x and d_y are the array x - and y -spacing. We note that for the normalization purposes we take $d_x = 270$ nm also for the 1D chain. In **Figure 1a,b** the real and imaginary parts of S and α_s are plotted, respectively. The difference between these quantities correspond to Δ and Γ defined above. It can be seen that the real part of S has a peak at the $\langle 0, -2 \rangle$ RA. In the vicinity of this RA there is a single intersection of the real parts, that is, $\Delta = 0$, determining the spectral location of the hybridized new resonance, and a step-like shape of the difference of imaginary parts Γ , leading to abrupt enhancement of the extinction at longer wavelengths than the RA point, as seen in **Figure 1c**. Overall, the extinction lineshape for the 1D chain shows very limited reduced extinction gap at the RA.

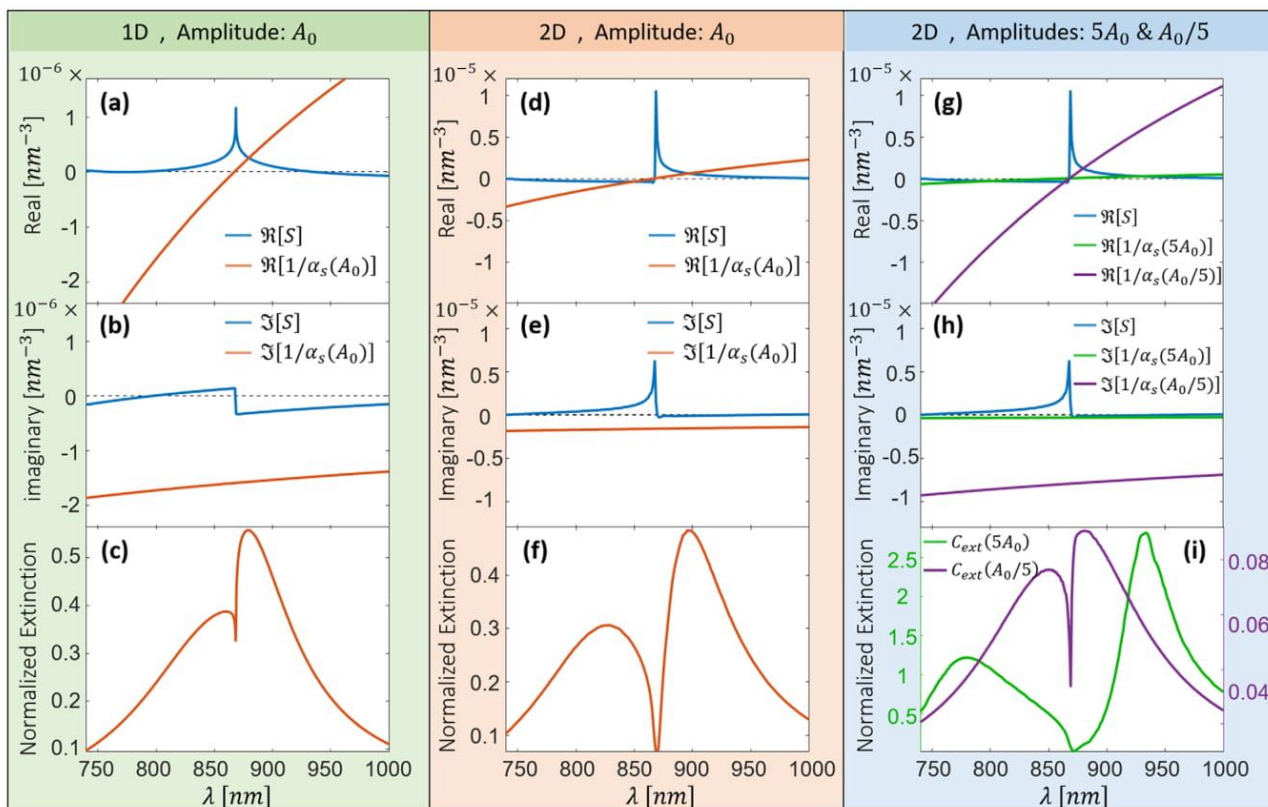


Figure 1. The interplay between the single particle and the whole array response, and their influence on the spectral extinction. The first column a–c) shows the real (a) and imaginary (b) parts of $1/\alpha_s$ and S , and the normalized extinction (c) of a 1D array with parameters given in the text. d–f) show the same quantities as in (a–c), but for a 2D array. The absorption-less band around $\lambda_{(0,-2)}^{RA} \approx 869$ nm shows narrower and deeper lineshape. g–i) show calculations for a 2D array with fivefold enhanced (green) and fivefold reduced (purple) amplitude of α_s . In both cases, the extinction (i) shows deviation from the desired lineshape of EIT, as presented in (f).

In Figure 1d–f we show similar plots to those shown in Figure 1a–c, but for a 2D array with the same periodicity in the y -direction and subwavelength periodicity in the x -direction ($d_x = 270$ nm and $d_y = 800$ nm). In this case, the peak of the real part of S rises much higher due to the addition of particles participating in the coherent scattering (notice the change in the y -axis range), which dictates a larger Δ and therefore reduced extinction at the RA. At both sides of the RA the real parts of S and $1/\alpha_s$ show intersections, which leads to resonative behavior surrounding the reduced extinction at the RA. In addition, from Figure 1e we see that now the imaginary part of S shows more symmetric lineshape around the RA, which leads to two distinct resonances, with a spectral hole burned in-between them. We stress that this absorption-less band appears while taking the entire loss mechanisms into account.

Next, we show that this desired behavior of the extinction that resembles the EIT lineshape, is strongly dependent on the amplitude of the polarizability, which in turn, commonly varies with the nanoparticles volume. Figure 1g–i show calculations for a 2D array with the same parameters as before, for two different amplitudes of α_s : $5A_0$ and $A_0/5$. While S has not changed from the calculations at Figures 1d–f the change in $1/\alpha_s$ is clearly seen: α_s has a constant resonance wavelength of $\lambda_0 = 868$ nm in all the calculated cases, therefore $\Re\{1/\alpha_s\}$ vanishes at this wavelength. The

change in A_0 causes tilt of the curve describing $\Re\{1/\alpha_s\}$, which in turn sets the crossing points with $\Re\{S\}$ at more separated locations as A_0 increases. In addition, the imaginary parts shown in Figure 1h set smaller Γ as A_0 increases. Therefore, the extinction (Figure 1i) reaches greater values as the amplitude A_0 increases, followed also by larger coupling of the plasmonic and photonic modes, that is, larger spectral separation of the resonances. On the other hand, when A_0 decreases reduced extinction along with smaller resonance splitting is observed. To obtain EIT-like behavior we wish to have large extinction values and a sharp dip between two peaks. Thus, Figure 1f shows the desired behavior of the extinction, while the results in Figure 1i for either the reduced or enhanced polarizability amplitude deviate from the desired trend. Hence, in the following we use the parameters used for the extinction calculation in Figure 1f.

2.2. Anomalous Phase Behavior Predicted by the Coupled Dipole Approximation

The spectral features obtained from the simulated array (see Figure 1d–f) were further studied to obtain the spectral phase response, for normal and for oblique incidence. Figure 2a presents the normalized extinction at normal incidence and at

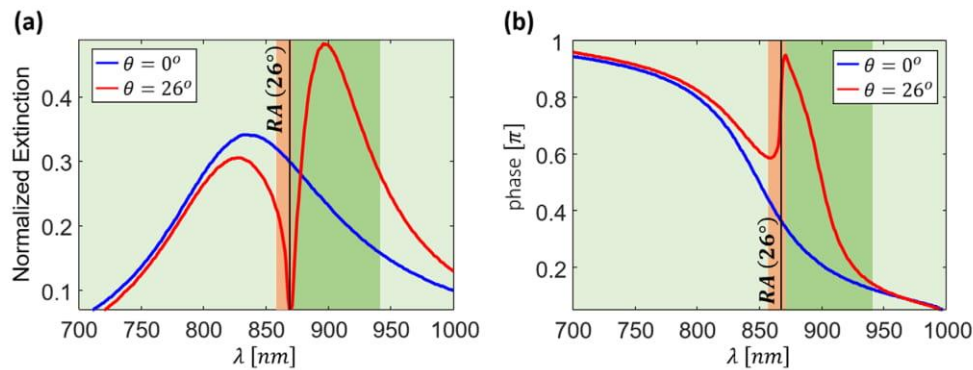


Figure 2. Absorption-less band accompanied by anomalous phase behavior. a) Simulated normalized extinction for two angles of incidence: $\theta = 0^\circ$ (blue line) and $\theta = 26^\circ$ (red line). b) The phase associated with the extinction of (a), calculated by the Kramers–Kronig relations on a finite bandwidth. The bright-green, dark-green, and orange regions in (a) and (b) correspond to regions with small positive, large positive, and large negative $d\phi/d\omega$ values.

oblique incidence of $\theta = 26^\circ$. The extinction of the oblique incidence is equivalent to that shown in Figure 1f and formerly discussed, while the extinction for normal incidence shows broad resonance that originates mainly from each particle's LSPR. The last remark is confirmed by the observations in Figure 1 that $S \approx 0$ far from any RA, which implies using Equation (1) that $\alpha_{\text{eff}} \approx \alpha_s$. By using the Kramers–Kronig relations, the frequency-dependent phase behavior can be calculated from the frequency-dependent absorption. In Figure 2b we show the corresponding phase calculated by the Kramers–Kronig relations on a finite bandwidth. The changing phase slopes shown in Figure 2b, according to $d\phi/d\omega$, can help distinguish between three different regions that are marked with different colors in Figure 2a,b. Bright green, dark green, and orange regions mark small positive, large positive, and large negative $d\phi/d\omega$ values, respectively. As elaborated in Section 2.4, the large negative $d\phi/d\omega$ region, right around the RA and absorption-less band, implies slow-light behavior.

2.3. SLR Induced Transparency—Experiments and Simulations

To experimentally examine the EIT features studied by the CDA we fabricated a corresponding metasurface comprising gold SRRs. These types of metasurfaces were studied extensively during the last two decades, mainly due to their engineered magnetic response,^[43–45] and artificial enhanced and controllable quadratic nonlinearities.^[8,46–50] Therefore, showing EIT-like behavior and slow light effects in SRR based metasurfaces may further allow controlling their associated phenomena. The sample, consisting of a $50 \mu\text{m} \times 50 \mu\text{m}$ rectangular array of gold SRRs, was fabricated by a standard electron-beam lithography. The array x - and y -spacing was $d_x = 270 \text{ nm}$ and $d_y = 800 \text{ nm}$, respectively (Figure 3a), which support the existence of RAs only along the y -direction. Each SRR had 190 nm base-length, 225 nm arms-length, 55 nm arms-width, 95 nm base-width, and thickness of 40 nm (Figure 3b). The sample was covered by immersion oil ($n = 1.51$), to obtain symmetric refractive index environment, and was placed on a rotational stage (Figure 3c,d). A white-light source (SuperK COMPACT, NKT Photonics) spanning wavelengths between 450 and 2400 nm was used (Figure 3d) to shine

x -polarized light on the sample (parallel to the base of the SRRs). Only the zero-order transmitted light was collected by an objective and tube lens and spectrally measured by an imaging spectrometer, allowing also broadband interferometric phase measurements by addition of a double-hole mask (for details see Section S1, Supporting Information).

We present the normalized extinction spectra of the studied sample in Figure 4a for two angles of incidence, $\theta = 0^\circ$ (blue line) and $\theta = 26^\circ$ (red line). These extinctions were calculated from the measured zero-order transmission $T_{(0,0)}$ by $C_{\text{ext}} = 1 - T_{(0,0)}$. The resonance that corresponds to the normal incidence case, originates from the particle's LSPR,^[51] as discussed in Section 2.2 (for full resonance characterization see Section S2, Supporting Information). It can be seen that the experiment supports narrow absorption-less band at the RA location, in agreement with the CDA simulation results in Figure 2a. Therefore, one may expect different regions of phase behavior as shown in Figure 2a,b. The region of large expected negative $d\phi/d\omega$ values is marked in Figure 4a by the orange background color. Furthermore, it is also expected that the spectral location of the LSPR would stay approximately constant with varying angle of incidence, whereas the dispersive RA will follow $\lambda_{(0,m_y)}^{\text{RA}} = \frac{n(\lambda) \cdot d_y}{|m_y|} (1 - \text{sign}(m_y) \cdot \sin(\theta))$, where m_y is an integer indicating the y th spatial diffraction order. Therefore, it is insightful to examine the plasmonic–photonic coupling, responsible for the observed effect, for varying incident angles. To do that we show the measured (Figure 4b) and simulated (Figure 4c) zero-order transmission for $\theta \in [0^\circ, 30^\circ]$ through the array. Figure 4c shows $T_{(0,0)}$ obtained by a FDTD solver (Lumerical). In these simulations the physical dimensions of the SRRs were slightly optimized relative to the fabricated sample to get similar spectral response to the measurements (see Section S3, Supporting Information). In Figure 4d we show the transmission simulated by the CDA, calculated by $1 - C_{\text{ext}}$. It can be seen that the measurements agree well with the FDTD simulation results and with the CDA calculations. The deviation of the CDA calculations in Figure 4d for wavelengths smaller than $\sim 700 \text{ nm}$ occurs due to the existence of higher order LSPR centered at wavelength of $\sim 550 \text{ nm}$ which was not taken into account in our CDA model. The agreement between simulations and measurements over the

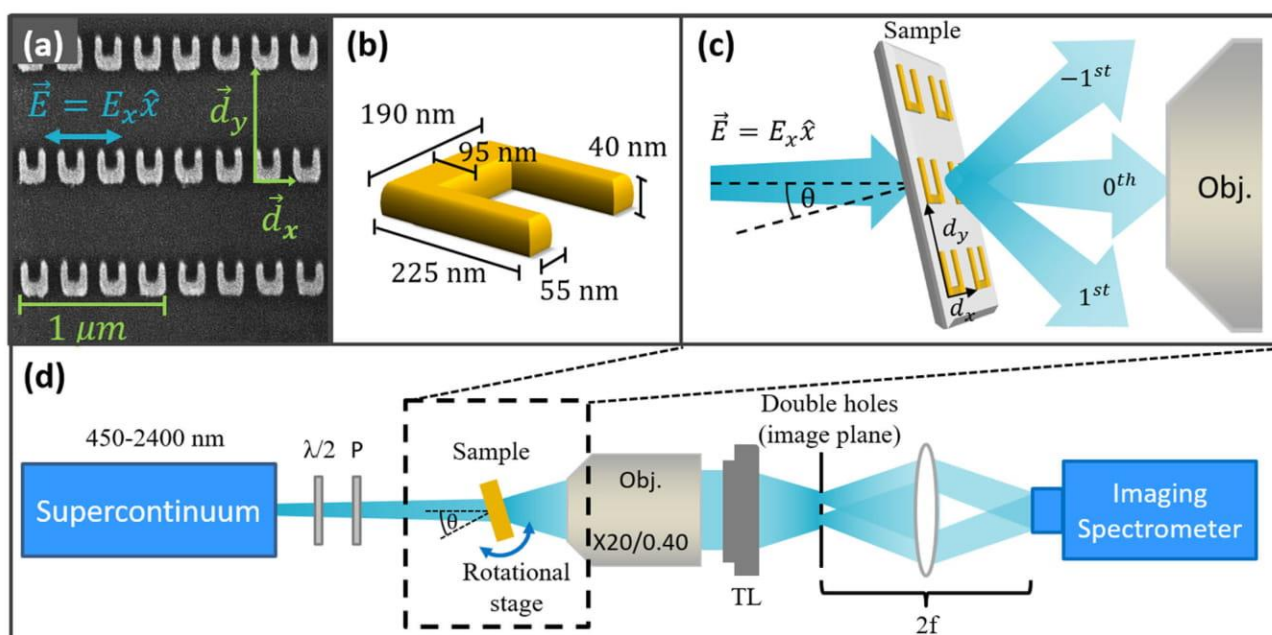


Figure 3. Metasurface information and experimental apparatus. a) Scanning electron microscope image of the fabricated sample. The incident electric field polarization is shown with the blue arrow. b) Illustration of the physical dimensions of each SRR. c) Illustration of the sample illumination and transmitted light collection. The incident light was x -polarized (parallel to the base of the SRRs), at an angle θ pivoting the x -direction. Only the zero-order transmitted light was collected by the objective. d) The experimental setup for the transmission and phase measurements. The setup comprised a supercontinuum source, half-wave plate ($\lambda/2$), polarizer (P), sample on a rotational stage, objective lens (Obj.), tube lens (TL), double-hole mask, $2f$ system, and an imaging spectrometer.

relevant region of interest (above ~ 700 nm) allows us to further investigate the observation with the FDTD and CDA simulations.

In the results, two different RAs, with an opposite slope in the wavelength (x -axis) -angle (y -axis) map can be distinguished. These RAs correspond to coherent buildup of scattered fields along opposite directions on the array. The $\langle 0, 1 \rangle$ (white dots) and the $\langle 0, -2 \rangle$ (black dots) RAs are co-directed and counter-directed with the parallel to the surface component of the incident wavevector, respectively. Narrow transparency windows appear at these two RAs, resulting in the formation of three separate absorption bands: i) A nondispersive band centered at ~ 845 nm for $\theta \in [0^\circ, 15^\circ]$. ii) Concave shaped band centered at ~ 910 nm for $\theta \in [10^\circ, 30^\circ]$. iii) Another nondispersive band centered at ~ 845 nm for $\theta \in [22^\circ, 30^\circ]$. At the crossing region of the two RAs a non-dispersive reduced transmission gap is seen, in agreement with previous observations of bandgap formation at the simultaneous coexistence of two RAs.^[52,53]

2.4. SLR Induced Slow Light—Experiment and Simulations

To investigate the expected slow light associated with the transparency windows we further measured and simulated the spectral phase of the zero-order transmitted light. The interferometric phase measurements were performed in common-path off-axis geometry and allowed us by a single capture to acquire the phase of the entire spectral range of interest, for each angle (for details see Section S1, Supporting Information). In Figure 5a we show the measured spectral phase for varying angles of incidence. Ex-

amining the phase at the array resonances, in accordance to their previous classification, a typical lineshape associated with a phase of Lorentzian is evident for absorption band i) while looking at the two other bands, ii) and iii) more complex phase variations can be seen, indicating the hybridized nature of these resonances. Importantly, we find that at the transparency along the RAs there is an abrupt phase change, as the Kramers–Kronig relations applied to Figure 2a imply. This phase dispersion, $\phi(\omega)$, quantifies the phase accumulated for each frequency component due to the interaction with the metasurface, and can be used directly to calculate the group delay $\tau_g = -\frac{d\phi}{d\omega}$. In Figure 5b,c we show the group delay extracted from the experiment (Figure 5b) and from FDTD simulation (Figure 5c). The experimental measurements and simulations show good agreement. At the RAs, mainly above their cross-point, the light is substantially delayed by the sample, reaching delay values of $\tau \approx 8$ fs, caused by the 40 nm thick sample. This delay occurs, both at the $\langle 0, 1 \rangle$ (white dots) and the $\langle 0, -2 \rangle$ (black dots) RAs, exactly at the transparency windows. In Figure 5d we show a cross section of the group delay (blue line) and the associated transmission (orange line) for $\theta = 26^\circ$. The high transmission peak ($T \approx 92\%$, Q factor ≈ 40) coincides with the high group delay peak (~ 7 fs). To elucidate the values shown for τ_g , which quantifies the delay of a pulse traversing the medium, it is worth comparing it with the time it takes to the pulse to cross the same width of the sample in free space. This time is $\tau \approx 40 \frac{\text{nm}}{c} \approx 0.13$ fs. Their ratio, τ_g/τ , which may be viewed as an effective group index, reaches values on the order of ~ 60 along the RAs. These findings imply that the time the light interacts with the sample is considerably longer than it would cross the same thickness at the speed of light, and yet, among the

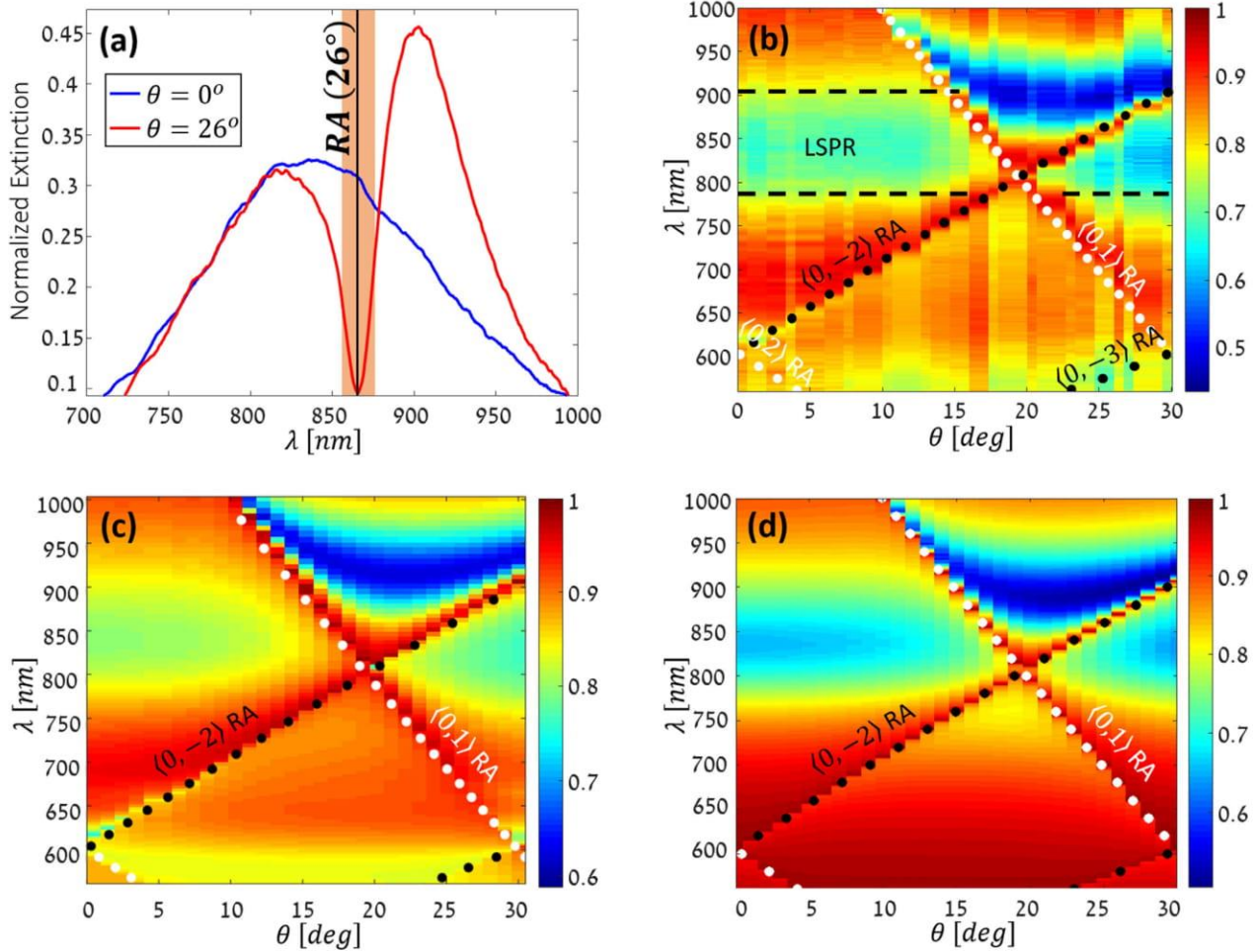


Figure 4. SLRs induced transparency. a) Experimental x-polarized normalized extinction for two angles of incidence: $\theta = 0^\circ$ (blue line) and $\theta = 26^\circ$ (red line). b) Experimental and c) FDTD simulated zero-order transmission for $\theta \in [0^\circ, 30^\circ]$. d) Shows $1 - C_{\text{ext}}$ simulated by the CDA. In (b–d) the (0, 1) and (0 – 2) RAs are marked with the white and black dots, respectively.

different energy routes such as absorption, reflection, and diffraction, it is being directed with very high efficiency ($\sim 92\%$) to the zeroth-order transmission. Another observation from Figure 5d is the coincidence of the transmission dip and group delay dip. This is a typical behavior of resonances, which appears even for a single resonance without the coupling dynamics.^[42] The negative group delay can be attributed to the fast light regions, though the associated high absorption prevents any practical use of it.^[42]

2.5. The Role of the Interplay between Incident and Scattered Fields

To further investigate the origin of the transparency seen along the RAs we use the CDA to examine the electric fields at the array surface, that is, at the near field. The local field at the i th nanoparticle can be written as $E_{\text{loc},i} = E_{\text{inc},i} + E_{\text{sca},i}$, where $E_{\text{inc},i}$ and $E_{\text{sca},i}$ are the incident field on the i th nanoparticle, and scattered fields from all the $j \neq i$ particles, respectively. The polarization of the i th nanoparticle can be written as $P_i = \alpha_s E_{\text{loc},i}$ or alternatively, by

terms of α_{eff} obtained with the CDA as $P_i = \alpha_{\text{eff}} E_{\text{inc},i}$. From the last three equations, the ratio of scattered to incident fields can be obtained

$$\frac{E_{\text{sca},i}}{E_{\text{inc},i}} = \frac{\alpha_{\text{eff},i}}{\alpha_s} - 1 \quad (2)$$

We would expect the scattered field to be influenced mainly by the coherent or incoherent sum of scattered fields from all the nanoparticles at the array, and by the nanoparticles' scattering amplitudes, reflected by α_s . In Figure 6 we show the amplitude (Figure 6a) and phase (Figure 6b) of $E_{\text{sca},i}/E_{\text{inc},i}$. Several observations can be made from these figures. As seen in Figure 6a, along the RAs the scattered fields are substantially increased, reaching values of $|E_{\text{sca},i}| \approx |E_{\text{inc},i}|$ at the transparency regions. These strong scattered fields are the result of the coherent buildup of the scattered fields at the RAs condition. In addition, at the region of absorption bands (i) and (iii), there are also relatively strong incoherently scattered fields (typically $|E_{\text{sca},i}| \approx 0.5|E_{\text{inc},i}|$) getting their contribution from the plasmonic resonance of α_s . Absorption band (ii) shows similar order of

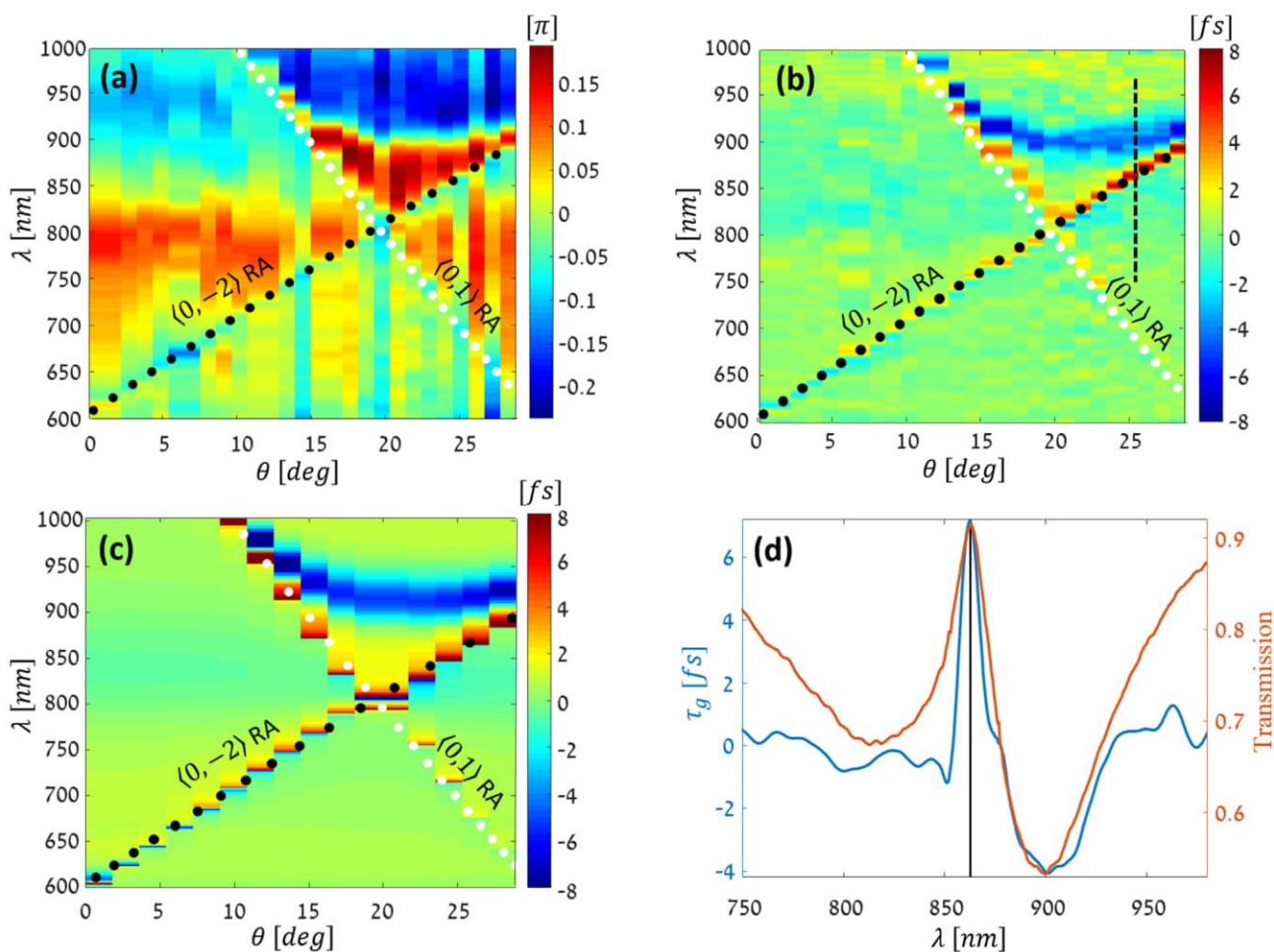


Figure 5. SLRs induced slow light. a) The x-polarized spectral phase for varying incident angles. b) Experimental and c) simulated by FDTD solver group delay calculated by $\tau_g = -\frac{d\phi}{d\omega}$. In (a–c) the (0,1) and (0–2) RAs are marked with the white and black dots, respectively. d) A cross section of the group delay (blue) and the transmission (orange) for angle of 26°. The black vertical line corresponds to the (0–2) RA.

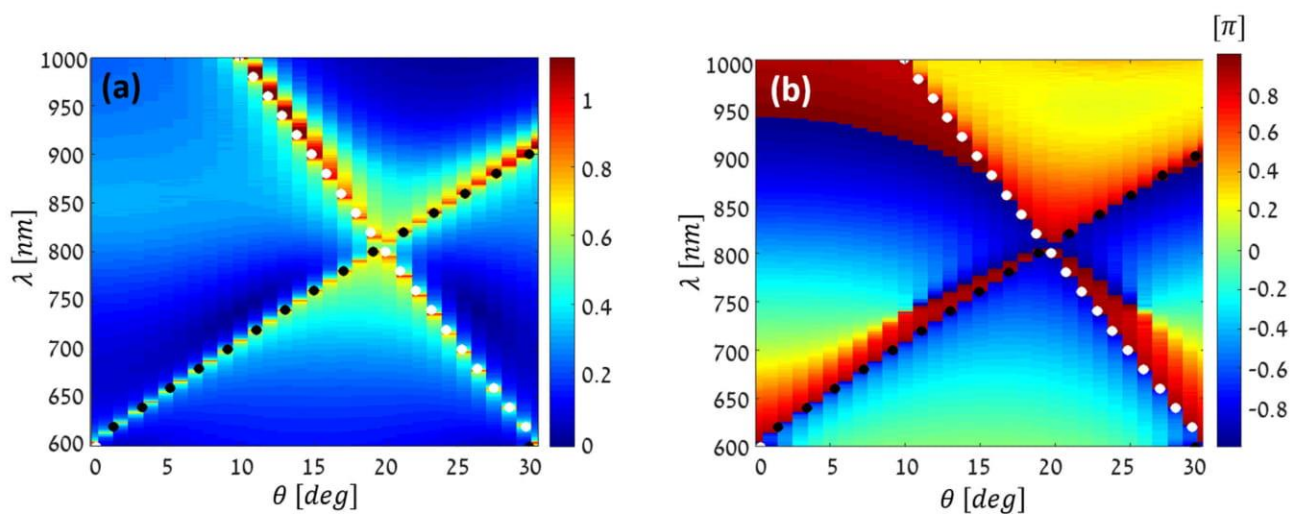


Figure 6. Calculated normalized scattered fields. a) Amplitude and b) phase of $E_{sca,i}/E_{app,i}$.

scattered fields, which in this case arise from the coupling of the plasmonic and photonic modes. From Figure 6b we see that along the RAs' transparency the scattered fields have a π -shifted phase relative to the incident field. Therefore, equal magnitudes and opposite phases of the scattered and incident fields cause complete destructive interference and thus give rise to the narrow transparency windows at the spectral coexistence of the plasmonic and photonic modes. Rearrangement of Equation (2) reflects how this destructive interference eliminates the effective polarizability: $\alpha_{\text{eff}} = \alpha_s \left(\frac{E_{\text{sca},i}}{E_{\text{inc},i}} + 1 \right)$. If we set the condition reflected from Figures 6a,b of $E_{\text{sca},i}/E_{\text{inc},i} \approx -1$ we get $\alpha_{\text{eff}}^{(\text{RAs})} \approx 0$, which agrees well with our experiment and simulations.

3. Conclusions

To conclude, we have demonstrated experimentally the existence of SLR induced transparency in plasmonic metasurfaces and its association with slow-light behavior. The plasmonic and photonic modes of the metasurface, respectively play the role of broad driven superradiant and narrow undriven subradiant coupled modes that are crucial to obtain EIT-like behavior. The effect is angle-dependent and can be tuned over a wide spectral range of ~ 200 nm. At the transparency windows, the group delay of the light reaches values of ~ 8 fs within only 40 nm thick sample. This corresponds to ~ 60 times longer interaction with the sample than in the case of non-resonant interaction. These values, along with the high transmission values, can be further improved by optimizing the controllable parameters in the CDA with a figure of merit of high quality transparency and slow light window. Intriguingly, in the studied case, in a counter-intuitive manner, strong scattering at the LSPR promotes the long-range interaction, while their coherent buildup almost totally eliminates the absorption. The SLR induced transparency and slow-light effects supported by our metasurface occur for S polarization. Examining also the zero-order transmitted light from the sample at P polarization, shows that at the transparency regions no similar effects take place at P polarization (see Section S4, Supporting Information). This reassembles Brewster-angle-like behavior, though for S polarization instead for P polarization. The presented study opens the door for implementation in the fields of sensing, displays, polarizers, optical buffers, tunable filtering, and enhanced nonlinear interaction. In addition, we believe that this work will promote fundamental future studies of nonlocal coherent interaction in metamaterials to facilitate the route toward tunable, integrated, ultra-small slow-light devices with high delaying capabilities.

Supporting Information

Supporting Information is available from the Wiley Online Library or from the author.

Acknowledgements

This publication is part of a project that has received funding from the European Research Council (ERC) under the European Union's Horizon 2020

Research and Innovation Programme (grant agreement No. 715362 and grant agreement No. 639402), and by the Ministry of Science, Technology and Space, Israel (grant agreement No. 3–15614). The authors thank Shay Keren-Zur, Ofer Doron, and Ofer Firstenberg for fruitful discussions.

Conflict of Interest

The authors declare no conflict of interest.

Keywords

coherent interaction, electromagnetic induced transparency, localized surface plasmons, slow light, surface lattice resonance

Received: June 17, 2019

Revised: September 25, 2019

Published online: November 28, 2019

- [1] J. D. Joannopoulos, P. R. Villeneuve, S. Fan, *Nature* **1997**, *386*, 143.
- [2] R. W. Boyd, *Nonlinear Optics*, 3rd ed., Academic Press, New York **2008**.
- [3] L. Rayleigh, *Proc. R. Soc. A* **1907**, *79*, 399.
- [4] V. G. Kravets, A. V. Kabashin, W. L. Barnes, A. N. Grigorenko, *Chem. Rev.* **2018**, *118*, 5912.
- [5] W. Wang, M. Ramezani, A. I. Väkeväinen, P. Törmä, J. G. Rivas, T. W. Odom, *Mater. Today* **2018**, *21*, 303.
- [6] B. B. Rajeeva, L. Lin, Y. Zheng, *Nano Res.* **2018**, *11*, 4423.
- [7] T. K. Hakala, A. J. Moilanen, A. I. Väkeväinen, R. Guo, J.-P. Martikainen, K. S. Daskalakis, H. T. Rekola, A. Julku, P. Törmä, *Nat. Phys.* **2018**, *14*, 739.
- [8] L. Michaeli, S. Keren-Zur, O. Avayu, H. Suchowski, T. Ellenbogen, *Phys. Rev. Lett.* **2017**, *118*, 243904.
- [9] W. Zhou, M. Dridi, J. Y. Suh, C. H. Kim, D. T. Co, M. R. Wasielewski, G. C. Schatz, T. W. Odom, *Nat. Nanotechnol.* **2013**, *8*, 506.
- [10] B. D. Thackray, V. G. Kravets, F. Schedin, G. Auton, P. A. Thomas, A. N. Grigorenko, *ACS Photonics* **2014**, *1*, 1116.
- [11] M. Fleischhauer, A. Imamoglu, J. P. Marangos, *Rev. Mod. Phys.* **2005**, *77*, 633.
- [12] N. Liu, L. Langguth, T. Weiss, J. Kästel, M. Fleischhauer, T. Pfau, H. Giessen, *Nat. Mater.* **2009**, *8*, 758.
- [13] S. Zhang, D. A. Genov, Y. Wang, M. Liu, X. Zhang, *Phys. Rev. Lett.* **2008**, *101*, 47401.
- [14] N. Papisimakis, V. A. Fedotov, N. I. Zheludev, S. L. Prosvirnin, *Phys. Rev. Lett.* **2008**, *101*, 253903.
- [15] Y. Yang, I. I. Kravchenko, D. P. Briggs, J. Valentine, *Nat. Commun.* **2014**, *5*, 5753.
- [16] R. D. Kekatpure, E. S. Barnard, W. Cai, M. L. Brongersma, *Phys. Rev. Lett.* **2010**, *104*, 243902.
- [17] A. H. Safavi-Naeini, T. P. M. Alegre, J. Chan, M. Eichenfield, M. Winger, Q. Lin, J. T. Hill, D. E. Chang, O. Painter, *Nature* **2011**, *472*, 69.
- [18] W. Cao, R. Singh, I. A. I. Al-Naib, M. He, A. J. Taylor, W. Zhang, *Opt. Lett.* **2012**, *37*, 3366.
- [19] R. Singh, I. A. I. Al-Naib, Y. Yang, D. Roy Chowdhury, W. Cao, C. Rockstuhl, T. Ozaki, R. Morandotti, W. Zhang, *Appl. Phys. Lett.* **2011**, *99*, 201107.
- [20] T. C. Tan, E. Plum, R. Singh, *Photonics* **2019**, *6*, 75.
- [21] N. Liu, T. Weiss, M. Mesch, L. Langguth, U. Eigenthaler, M. Hirscher, C. Sönnichsen, H. Giessen, *Nano Lett.* **2010**, *10*, 1103.
- [22] A. Artar, A. A. Yanik, H. Altug, *Nano Lett.* **2011**, *11*, 1685.

- [23] M. Sandtke, L. Kuipers, *Nat. Photonics* **2007**, *1*, 573.
- [24] A. Kocabas, S. S. Senlik, A. Aydinli, *Phys. Rev. Lett.* **2009**, *102*, 63901.
- [25] K. Ooi, T. Okada, K. Tanaka, *Phys. Rev. B* **2011**, *84*, 115405.
- [26] S. Linden, J. Kuhl, H. Giessen, *Phys. Rev. Lett.* **2001**, *86*, 4688.
- [27] Z.-G. Dong, P.-G. Ni, J. Zhu, X. Zhang, *Opt. Express* **2012**, *20*, 7206.
- [28] V. Yannopoulos, E. Paspalakis, N. V. Vitanov, *Phys. Rev. B* **2009**, *80*, 35104.
- [29] B. Tang, L. Dai, C. Jiang, *Phys. Lett. A* **2012**, *376*, 1234.
- [30] X. Xiao, B. Zhou, X. Wang, J. He, B. Hou, Y. Zhang, W. Wen, *Sci. Rep.* **2015**, *5*, 12251.
- [31] T. Zentgraf, S. Zhang, R. F. Oulton, X. Zhang, *Phys. Rev. B* **2009**, *80*, 195415.
- [32] M. Manjappa, Y. K. Srivastava, R. Singh, *Phys. Rev. B* **2016**, *94*, 161103.
- [33] M. C. Schaafsma, A. Bhattacharya, J. G. Rivas, J. Goetz Rivas, *ACS Photonics* **2016**, *3*, 1596.
- [34] T. C. Tan, Y. K. Srivastava, M. Manjappa, E. Plum, R. Singh, *Appl. Phys. Lett.* **2018**, *112*, 201111.
- [35] S. Zou, N. Janel, G. C. Schatz, *J. Chem. Phys.* **2004**, *120*, 10871.
- [36] S. Zou, G. C. Schatz, *J. Chem. Phys.* **2004**, *121*, 12606.
- [37] B. Auguié, W. L. Barnes, *Phys. Rev. Lett.* **2008**, *101*, 143902.
- [38] T. K. Hakala, H. T. Rekola, A. I. Väkeväinen, J.-P. Martikainen, M. Nečada, A. J. Moilanen, P. Törmä, *Nat. Commun.* **2017**, *8*, 13687.
- [39] A. I. Väkeväinen, R. J. Moerland, H. T. Rekola, A. P. Eskelinen, J. P. Martikainen, D. H. Kim, P. Törmä, *Nano Lett.* **2014**, *14*, 1721.
- [40] F. J. García de Abajo, *Rev. Mod. Phys.* **2007**, *79*, 1267.
- [41] J. B. Khurgin, *Adv. Opt. Photonics* **2010**, *2*, 287.
- [42] R. W. Boyd, *J. Mod. Opt.* **2009**, *56*, 1908.
- [43] D. R. Smith, W. J. Padilla, D. C. Vier, S. C. Nemat-Nasser, S. Schultz, *Phys. Rev. Lett.* **2000**, *84*, 4184.
- [44] R. A. Shelby, D. R. Smith, S. Schultz, *Science* **2001**, *292*, 77.
- [45] S. Linden, C. Enkrich, M. Wegener, J. Zhou, T. Koschny, C. M. Soukoulis, *Science* **2004**, *306*, 1351.
- [46] M. W. Klein, C. Enkrich, M. Wegener, S. Linden, *Science* **2006**, *313*, 502.
- [47] N. Segal, S. Keren-Zur, N. Hendler, T. Ellenbogen, *Nat. Photonics* **2015**, *9*, 180.
- [48] K. O'Brien, H. Suchowski, J. Rho, A. Salandrino, B. Kante, X. Yin, X. Zhang, K. O'Brien, H. Suchowski, J. Rho, A. Salandrino, B. Kante, X. Yin, X. Zhang, *Nat. Mater.* **2015**, *14*, 379.
- [49] S. Keren-Zur, O. Avayu, L. Michaeli, T. Ellenbogen, *ACS Photonics* **2016**, *3*, 117.
- [50] S. Keren-Zur, M. Tal, S. Fleischer, D. M. Mittleman, T. Ellenbogen, *Nat. Commun.* **2019**, *10*, 1778.
- [51] I. De Leon, M. J. Horton, S. A. Schulz, J. Upham, P. Banzer, R. W. Boyd, *Sci. Rep.* **2015**, *5*, 13034.
- [52] S. R. K. Rodriguez, A. Abass, B. Maes, O. T. A. Janssen, G. Vecchi, J. Gómez Rivas, *Phys. Rev. X* **2011**, *1*, 021019.
- [53] L. Shi, T. K. Hakala, H. T. Rekola, J.-P. Martikainen, R. J. Moerland, P. Törmä, *Phys. Rev. Lett.* **2014**, *112*, 153002.

Supporting Information

Near-Infrared Tunable Surface Lattice Induced Transparency in Plasmonic Metasurface

Lior Michaeli [1-3] *, Haim Suchowski [1,2], Tal Ellenbogen [1,3]

1. Phase Measurements

The broadband phase measurements were performed relying on common-path off-axis geometry and the use of an imaging spectrometer. At the image plane of the microscope setup we placed a double-hole mask for the generation of two angled plane waves at the Fourier plane of the mask. One wave carried information from the sample and the other from the reference (substrate). The Fourier plane of the double-hole mask was imaged on the entrance slit of the imaging spectrometer. This is shown in **Figure S1** below. The obtained interferogram was analyzed and used to extract the spectral phase as described by Bowlan et al.^[1] for the case of ultrashort pulse characterizations.

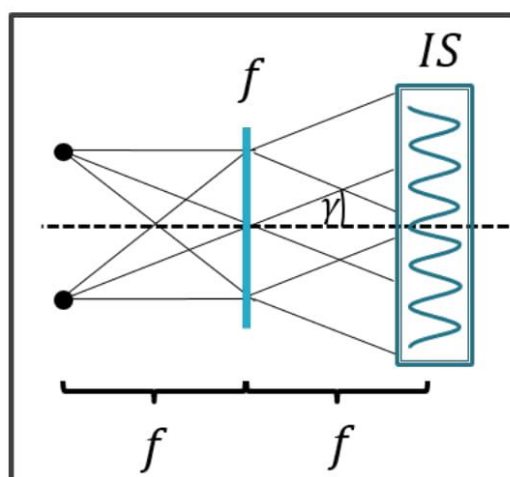


Figure S1. The off axis interferometry geometry. A double-hole mask was placed at the image plane of the microscope. The Fourier plane of the mask was imaged on the entrance slit of an imaging spectrometer (IS).

2. SRRs Resonance Characterization

Figure S2 illustrates the charge distribution and far-field radiation pattern at the x-y plane of the SRRs' localized mode used throughout this paper (red curve). The radiation pattern was obtained by the FDTD simulations for the case of a single isolated particle at normal incidence and at wavelength of $\lambda = 860 \text{ nm}$. The calculated far-field radiation pattern of a dipole mode is shown by the blue curve, for comparison.

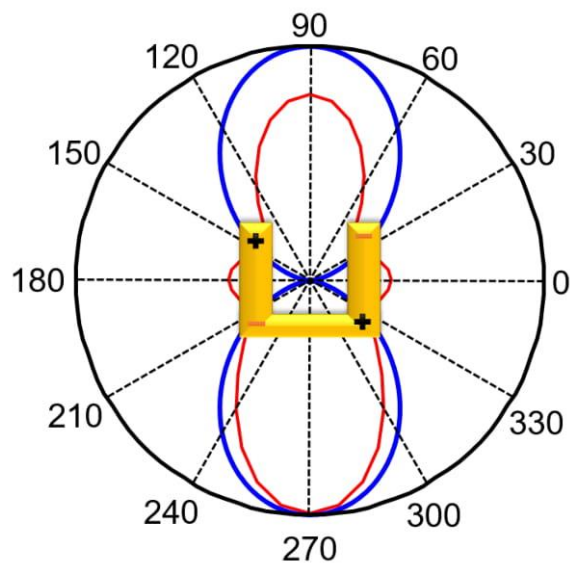


Figure S2 Schematic charge distribution and far-field radiation patterns. The far-field radiation pattern at the x-y plane of the SRRs' localized mode is shown in red and calculated far-field radiation pattern of a dipole mode is shown in blue.

3. SRRs Dimensions in the FDTD Simulation

In the FDTD simulations the physical dimensions of each SRR were slightly optimized relative to the fabricated sample to get similar spectral response to the measurements. The parameters taken were: **170 nm** base-length, **200 nm** arms-length, **50 nm** arms-width, **95 nm** base-width and thickness of 40 nm.

4. Transmission in S and P Polarization

Here we examine the S- and P-polarized transmission of our metasurface which show together Brewster-angle-like behavior. In **Figure S3a** and **b** the zero-order transmission for S- and P-polarized light is presented respectively. Figure S2b shows that at P polarization a bright localized surface plasmon resonance (LSPR) appears for central wavelength of $\lambda \approx 1000 \text{ nm}$ and a dark LSPR which hybridizes with the $\langle 0,1 \rangle$ Rayleigh anomaly (RA) appears around $\sim 700 \text{ nm}$ and $\theta \in [25^\circ, 30^\circ]$. Yet, though the P-polarization measurements exhibit resonative features, the unique plasmonic-photonic coupling mechanism responsible for the transparency and slow light remains only at the S polarization.

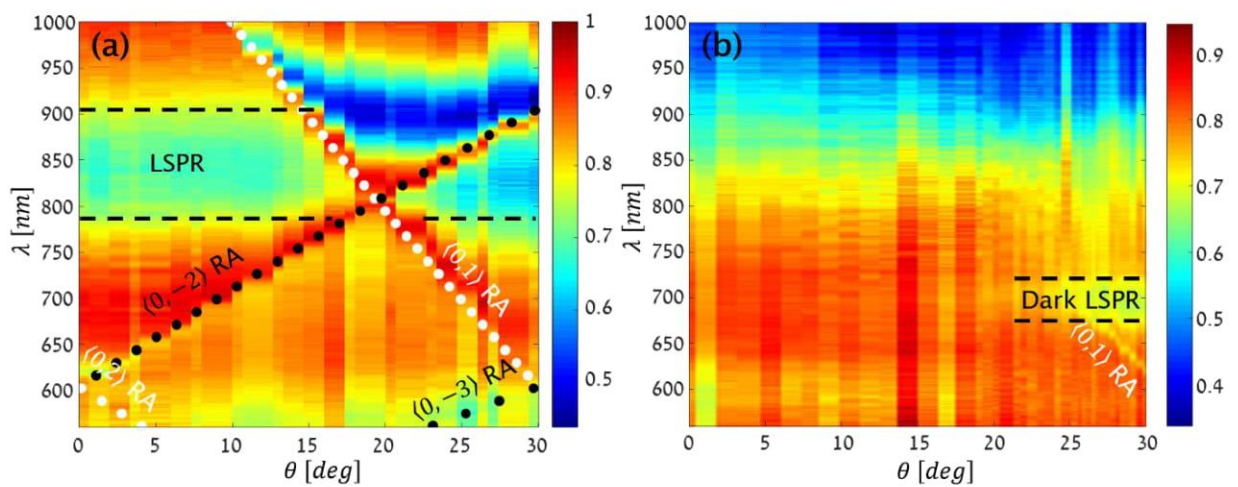


Figure S3 Brewster-angle-like behavior. Zero-order transmission from the sample for (a) S and (b) P polarizations.

Corresponding Author

*E-mail: liormic1@mail.tau.ac.il

References

- [1] P. Bownan, P. Gabolde, A. Shreenath, K. McGresham, R. Trebino, and S. Akturk, *Opt. Express*, **2006**, *14*, 11892.

2.3 Spectral Interferometric Microscopy for Fast and Broadband Phase Characterization

Spectral Interferometric Microscopy for Fast and Broadband Phase Characterization

Lior Michaeli,* Danielle Ben Haim, Mukesh Sharma, Haim Suchowski, and Tal Ellenbogen

The rapid growth in the development of new optical materials such as 2D materials, layered heterostructures, active phase changing materials, optical metasurfaces, and metamaterials, requires new methods which enable accurate, broadband, and real-time microscopic characterization of their optical and physical properties. Here, this necessity is addressed and a novel method is presented to dynamically and accurately obtain the spectral phase of a microscopic sample, either in reflection or transmission. The method is based on a designed optical relay that couples the output port of a typical microscope setup to an imaging spectrometer. By post-processing the acquired images, a stable, accurate, and easy-to-align broadband spectral microscopic interferometer is obtained. This approach is experimentally demonstrated by measuring the spectral phase response of two different types of metasurfaces in reflection and in transmission and also by accurately measuring the dispersion of a thick glass slab in transmission. Moreover, the method's applicability to broadband dynamic measurements is demonstrated by real-time tracking the phase response of optically driven nematic to isotropic and isotropic to nematic phase transitions of a liquid crystal. Altogether this method enables accurate, dynamic, and easy microscopic phase characterization and can become widely used for materials characterization.

characterization of the sample's optical and physical properties. For example, it enables detection and quantification of exotic phenomena such as negative refraction,^[1–5] artificial magnetism,^[6–10] zero refractive index,^[11–13] and electromagnetic-induced transparency (EIT) behavior and its associated slow light.^[14–16] Numerous optical schemes exist for direct broadband interferometric phase measurements. Typically they rely on recording either the time-resolved interferogram (TRI)^[17,18] or spectrally resolved interferogram (SRI)^[17,19] of two interfering light beams. Obtaining the interferogram in these methods can either be done by successive acquisitions, e.g., with the use of a delay stage for TRI or tunable source for SRI, or by simultaneous acquisition where the entire interferogram is obtained in a single shot. For SRI, such simultaneous acquisition merely requires a spectrometer, whereas a more sophisticated method is required for the case of TRI. For example, by mapping the relative delay of the two interfering beams into different spatial positions in an off-axis con-

1. Introduction

Measuring the spectral phase of light reflected or transmitted from a microscopic sample is often required for the full

figuration, and simultaneously recording the intensity with a detector array. In this approach, the spatially resolved interferogram (SRI) is obtained, which is directly mapped into the TRI.

In addition to these widely used methods, the quest for simpler experimental technique, with better spectral resolution and shorter acquisition times, mainly driven by the need for characterization of ultra-short pulses has resulted in development of a new class of interferometers: spatially and spectrally resolved interferometers (SSRIs).^[20–23] In this class, a camera is used to record the interference pattern of two beams in an off-axis configuration, where one axis is devoted to the spatial resolution and the other, by the aid of a diffraction grating, to spectral resolution. These methods, which enable single-shot broadband spectral phase extraction without any moving mechanical parts, have been demonstrated adequate for challenging pulse characterization^[24–26] and have also been improved to show better temporal^[27] or spatial^[28] capabilities. Detailed review and analysis of these methods can be found in Borzsonyi et al.^[29,30]

The integration of the appealing SSRI technique with optical microscopy has been suggested by O'Brien et al.,^[31] where based on Mach–Zehnder reflective interferometer

L. Michaeli, D. Ben Haim, Dr. M. Sharma, Prof. T. Ellenbogen
Department of Physical Electronics
Faculty of Engineering
Tel-Aviv University
Tel-Aviv 6779801, Israel
E-mail: liormic1@mail.tau.ac.il

L. Michaeli, Prof. H. Suchowski
Raymond and Beverly Sackler School of Physics & Astronomy
Tel-Aviv University
Tel-Aviv 6779801, Israel

L. Michaeli, D. Ben Haim, Dr. M. Sharma, Prof. H. Suchowski,
Prof. T. Ellenbogen
Center for Light-Matter Interaction
Tel-Aviv University
Tel-Aviv 6779801, Israel

 The ORCID identification number(s) for the author(s) of this article can be found under <https://doi.org/10.1002/adom.202000326>.

DOI: 10.1002/adom.202000326

they have successfully demonstrated phase characterization of metasurface sustaining plasmonic EIT. One of the challenges in merging microscopy, spectroscopy, and interferometry lies in the dispersive nature of the optics used for the imaging and magnification in addition to the microscope slide, which typically set much larger spectral phase variations to the sample beam than the sample itself. In addition, the difficulty of realizing broadband single-shot phase acquisition of microscopic samples in a common-path configuration sets severe limits on the complexity of such optical setups and on their sensitivity to noise. Gennaro et al. have reported such a configuration, based on SSRI integrated within a microscope, where they successfully realized a common-path configuration, by the use of two objective lenses, for the illumination and collection of light from the sample.^[32] Very recently, a technique using similar concepts, though for only a single wavelength, has been reported.^[33] This technique benefits from relatively stabilized time-dependent noise owing to three-beam interference. These two mentioned methods^[32,33] require tightly focused illumination, and are not suitable for collimated beam illumination schemes, angle-resolved measurements, or for structured beam illumination. Thus, their use is not suited for many applications, e.g., the extraction of consecutive material effective parameters by complex S-parameters measurements,^[34–36] or the characterization of phenomena as surface lattice resonances in plasmonic metasurfaces.^[37,38]

Here, we present a novel approach to overcome these limitations, by implementing an SSRI in a common-path configuration based on a double-hole mask located at the image plane of the microscope. The novel Masked Image-plane Common-path self-Referenced Optical SSRI (MICRO-SSRI) enables flexible sample illumination, stable, accurate, and easy-to-align single-acquisition spectral phase extraction by only slightly modifying a typical spectroscopy microscope setup. We experimentally demonstrate this powerful method by performing a set of challenging phase measurements, which require the following capabilities: microscopic resolution, plane wave illumination, transmission and reflection modes, large dynamic range of phase change (much bigger than 2π), and real-time dynamic characterization. Specifically, our experimental demonstrations include measurements in transmission mode of 170 μm thick glass, which enable extraction of the wavelength-dependent refractive index, and also serve as a spectral phase target for the demonstration of the methods accuracy. Furthermore, to show the applicability of the method to characterize new materials, we also measure the phase response of a plasmonic metasurface sustaining an angle-dependent EIT behavior, and the rich spectral phase response in reflection of a reflective Fabry–Perot metasurface-based element. The experimental results are in good agreement to finite-difference-time-domain (FDTD) simulation results. In addition, to examine the applicability of the method for examination of time varying systems, we performed real-time dynamic broadband phase measurements of a nematic liquid crystal (LC) under optically induced conformation. We identify in our measurements both continuous phase changes, associated with the temperature-

dependent refractive index of the LC, and discontinuities associated with the abrupt change in the order parameter at the isotropic–nematic and nematic–isotropic phase transitions. Finally, we also discuss how further manipulating the image plane of the microscope enables even more accurate and stabilized measurements in only a single shot, based on three-beam interference.

2. Setup Description

In this section, we describe the working principle of our phase measurement technique. **Figure 1a** shows the schematic illustration of the configuration used for the phase characterization. Incoming broadband light is shined on the plane containing the sample and the reference areas, here shown as metasurface on glass and bare glass, respectively. An objective and a tube lens are used to image and magnify the sample-reference plane. A double-hole mask located at the image plane transmits from one hole only light passing through the sample and from the other only light from the reference. A lens images the Fourier plane of the mask, which consists of two slightly angled beams from the reference and the sample, on the imaging spectrometer entrance slit to produce the broadband interferogram on the camera. **Figure 1b** shows the working principle of the two holes assisted off-axis interferometry, where the relative delay between two slightly angled light beams is mapped into different spatial positions. This occurs by the aid of the lens, transforming the light from each hole to a plane wave with well-defined angle. In the case of uncalibrated system, two acquisitions, rather than one, are required to obtain the spectral phase of the sample. These acquisitions are depicted in **Figure 1c**. In the first acquisition, the two holes, H_1 and H_2 , transmit light from the reference area, while in the second the double-hole mask is moved such that H_1 transmits light from the reference and H_2 from the sample.

According to the described scheme and the acquisitions depicted in **Figure 1c**, the two interferograms captured by the 2D-sensor array corresponds to (see full theoretical description in the Supporting Information, Section S2)

$$I_{\text{captured}}^{\text{RR}}(\lambda, \gamma) = |E_{\text{source}}^{(0)}(\lambda)T_{\text{R}}^{(0)}(\lambda)|^2 + |E_{\text{source}}^{(0)}(\lambda)T_{\text{R}}^{(0)}(\lambda)|^2 + |E_{\text{source}}^{(0)}(\lambda)|^2 |T_{\text{R}}^{(0)}(\lambda)|^2 e^{-2ik_y\gamma} + |E_{\text{source}}^{(0)}(\lambda)|^2 |T_{\text{R}}^{(0)}(\lambda)|^2 e^{2ik_y\gamma} \quad (1a)$$

$$I_{\text{captured}}^{\text{RS}}(\lambda, \gamma) = |E_{\text{source}}^{(0)}(\lambda)T_{\text{R}}^{(0)}(\lambda)|^2 + |E_{\text{source}}^{(0)}(\lambda)T_{\text{S}}^{(0)}(\lambda)|^2 + |E_{\text{source}}^{(0)}(\lambda)|^2 |T_{\text{R}}^{(0)}(\lambda)||T_{\text{S}}^{(0)}(\lambda)| e^{i(\phi_{\text{R}}(\lambda) - \phi_{\text{S}}(\lambda))} e^{-2ik_y\gamma} + |E_{\text{source}}^{(0)}(\lambda)|^2 |T_{\text{R}}^{(0)}(\lambda)||T_{\text{S}}^{(0)}(\lambda)| e^{-i(\phi_{\text{R}}(\lambda) - \phi_{\text{S}}(\lambda))} e^{2ik_y\gamma} \quad (1b)$$

where the sub/superscripts “R” and “S” correspond to light passing through the reference and sample areas, respectively. The light intensity $I_{\text{captured}}(\lambda, \gamma)$ on the 2D-sensor array depends on the wavelength λ and spatial position γ , corresponding to the sensor’s horizontal and vertical axes, respectively. $E_{\text{source}}^{(0)}(\lambda)$ is the spectral electric-field amplitude of the source, and the complex transmission amplitude of the

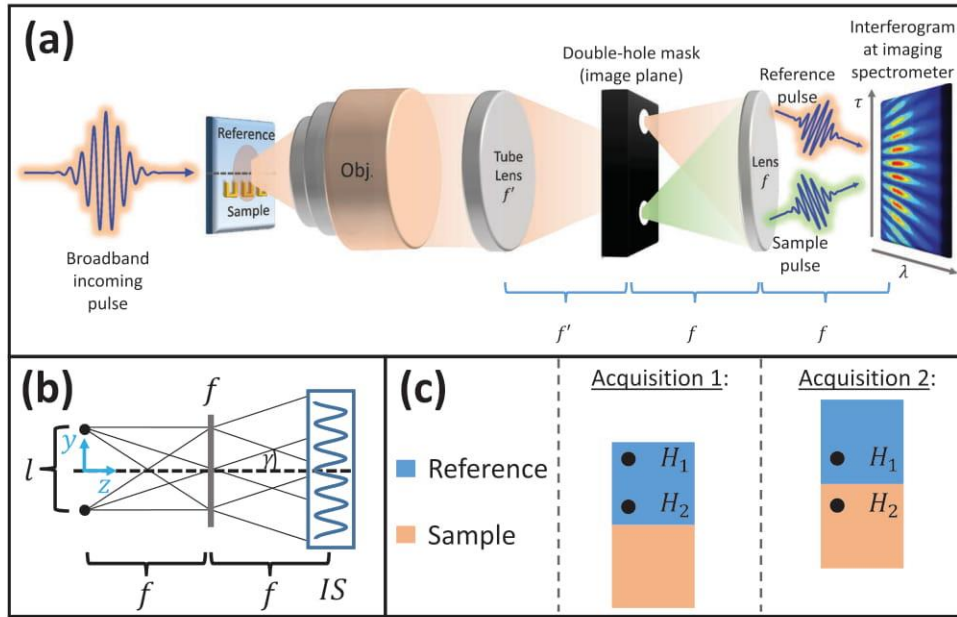


Figure 1. Schematic illustrations of the MICRO-SSRI working principle. a) The broadband interferogram production. Incoming broadband light is shined on the plane containing the sample and the reference, here shown as metasurface and bare glass, respectively. Double-hole mask passes from one hole only light from the sample and from the other only light from the reference. A lens images the Fourier plane of the mask on the imaging spectrometer, to produce the broadband interferogram of the sample. b) Ray optics illustration showing the slightly angled beam generation from two holes by a single lens. The distance between the holes, l , determines the half-angle between the beams $\gamma = \arctan(l/(2f))$. c) For noncalibrated system, two acquisitions need to be taken: 1) The two holes are placed on the reference area. 2) One hole is placed on the sample and the other on the reference area.

sample/reference is divided into amplitude and phase terms according to $T_{S,R}(\lambda) = |T_{S,R}^{(0)}(\lambda)| e^{i\phi_{S,R}(\lambda)}$. The y -component of the wavevector $k = 2\pi/\lambda$ is directly determined from the angle $\gamma = \arctan(l/(2f))$ by $k_y = k \cdot \sin(\gamma)$ (see Figure 1b).

From Equation (1b), we see that the information of interest, $\Delta\phi(\lambda) \equiv \phi_S(\lambda) - \phi_R(\lambda)$, is encoded in the modulation at spatial frequency $2k_y$. To extract this phase difference, we convolve the interferograms from Equations (1) with corresponding spatial band-pass filter $H_{BP}(\gamma)$

$$(I_{\text{captured}}^{\text{RR}}(\lambda) \odot H_{BP})(\gamma) = \pi |E_{\text{source}}^{(0)}(\lambda)|^2 |T_R^{(0)}(\lambda)|^2 e^{2ik_y \gamma} \quad (2a)$$

$$(I_{\text{captured}}^{\text{RS}}(\lambda) \odot H_{BP})(\gamma) = \pi |E_{\text{source}}^{(0)}(\lambda)|^2 |T_R^{(0)}(\lambda)| |T_S^{(0)}(\lambda)| e^{i\Delta\phi(\lambda)} e^{2ik_y \gamma} \quad (2b)$$

Then, by dividing Equation (2b) with Equation (2a), we get their ratio

$$r(\lambda) = \frac{|T_S^{(0)}(\lambda)|}{|T_R^{(0)}(\lambda)|} e^{i\Delta\phi(\lambda)} \quad (3)$$

The absolute value of $r(\lambda)$ is the spectral field transmission (or reflection) and its phase is the wavelength-dependent phase difference $\Delta\phi(\lambda)$ of interest. This way the full complex transmission or reflection spectra is obtained from only two acquisitions. For phase only information, even one acquisition is sufficient. Full setup description for both the transmission and reflection modes can be found in Section S1 of the Supporting Information.

3. Experimental Results

3.1. Measurements of Refractive Index versus Wavelength of a Glass Slab

Here, we demonstrate the accuracy of the MICRO-SSRI method by measuring a glass slab with a specified dispersion. By accounting for the length of the sample, we extract the wavelength-dependent refractive index $n(\lambda)$ of the glass. We show that the fine spectral resolution of the interferograms enables the obtained phase to be unambiguously unwrapped, even for a slab as thick as $L = 170 \mu\text{m}$ as long as the refractive index is known in a single wavelength.

The measured glass slab sample was a high-performance cover slip made from Schott D263 M glass, with manufacturer reported length of $L = 170 \pm 5 \mu\text{m}$. Figure 2a,b shows the reference–reference (Figure 2a) and reference–sample (Figure 2b) interferograms (according to acquisitions 1 and 2 in Figure 1c), each obtained within a single acquisition. The large phase accumulation and dispersion of light passing through the glass sample is visually evident, in the interferogram shown in Figure 2b, by the oblique trend of the fringes. After post-processing these interferograms, as described in detail in Section S2 of the Supporting Information, we obtained the phase difference $\Delta\phi(\lambda) = \frac{2\pi}{\lambda} \Delta n(\lambda)L$, shown in Figure 2c. Here $\Delta n(\lambda) \equiv n_s(\lambda) - n_r(\lambda)$ is the difference between refractive index of the sample $n_s(\lambda)$, and the reference (air in this case) $n_r(\lambda) = n_{\text{air}} \equiv 1$. We note that unwrapping the phase was easily done by requiring continuity of $\Delta\phi(\lambda)$, where the fine spectral resolution guaranteed that no phase jumps bigger

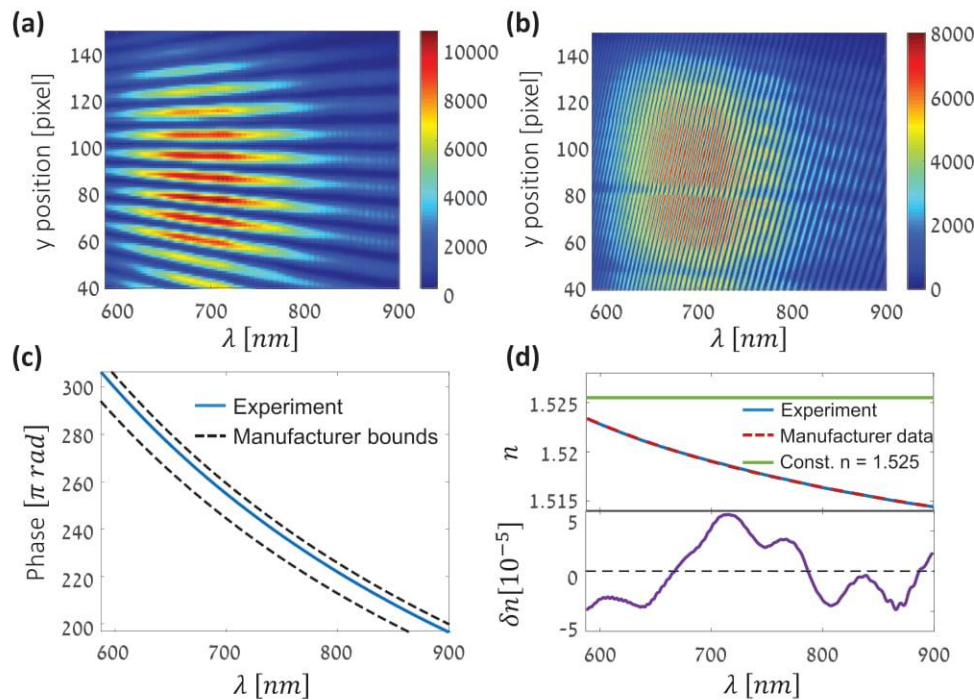


Figure 2. Measured interferograms of the a) reference and b) 170 μm thick glass sample (Schott D263 M). c) The associated extracted phase of the sample is shown by the blue solid line. The black dashed lines are the manufacturer bounds for the accumulated phase. d) The top part shows the refractive index: extracted from the measurements (blue solid line), according to the manufacturer data (red dashed line) and the constant approximation of $n = 1.525$ (green solid line). The bottom part shows the residuals according to the difference between the experimental and reported refractive index.

than 2π were hidden in the data. We also anchored the phase in a single wavelength ($\lambda = 666 \text{ nm}$) to account for the correct wrapping branch. It can be seen that phase accumulation differences of dozens of radians have been successfully recovered. By accounting for the manufacturer reported refractive index of the glass, $n_m(\lambda)$, and for its length,^[39] we calculated the upper and lower bounds of the phase difference, shown by the black dashed lines in Figure 2c. The two bounds correspond to the 5 μm error of the sample length. It can be seen that the measured phase is well situated between these two bounds. By isolating $n_s(\lambda)$ from the phase expression, i.e., $n_s(\lambda) = n_{\text{air}} + \frac{\lambda \Delta \phi(\lambda)}{2\pi L}$, we extracted also the sample's refractive index, shown in the top part of Figure 2d. The length used here was 172 μm , which is in the length range of the glass. Very good agreement with the reported manufacturer data is seen, with clear deviation from the nondispersive approximation for this glass of $n(\lambda) = 1.5255$. The bottom part of Figure 2d shows the residuals plot according to $\delta n(\lambda) = n_s(\lambda) - n_m(\lambda)$. Error smaller than 5×10^{-5} is seen at the entire spectral range of measurements. These measurements demonstrate the accuracy of the method along with its potential to extract unambiguously the refractive index of microscopic samples. We stress that even better accuracy can be achieved by using high-end, aberration-corrected optics in an isolated optical setup.

3.2. Microscopic Phase Measurement of Metasurfaces

Here, we show the applicability of our technique to analysis of microscopic samples with complex phase response. For

this goal, we measure two types of metasurfaces, in reflection and in transmission. Schematic illustration of the first metasurface, that was measured in reflection, is shown in the inset of Figure 3a. The metasurface is composed of three layers: 200 nm of aluminum, 600 nm of SiO_2 , and 40 nm thick squared aluminum nanodisks array of $50 \mu\text{m} \times 50 \mu\text{m}$. In Figure 3a, we present the broadband phase measurements of two samples: sample 1 with radius $r = 73 \text{ nm}$ and periodicity of $d = 270 \text{ nm}$ (blue line) and sample 2 with $r = 48 \text{ nm}$ and $d = 240 \text{ nm}$ (orange line). The reference used for the phase measurement is a similar structure without the nanodisks. Figure 3b shows the corresponding reflection measurements, extracted from the same acquisitions used for the phase characterization. It can be seen from the reflection that there are two dips located around $\approx 560 \text{ nm}$ ($\approx 540 \text{ nm}$) and $\approx 780 \text{ nm}$ ($\approx 770 \text{ nm}$), of the blue (orange) curves. These dips appear due to coupling of localized surface plasmon resonance (LSPR) and a Fabry–Perot mode of the structure.^[40] It can be seen that the phase changes significantly around the resonance dips. At the off-resonance regimes, where the reflection is high, the phase is close to zero, as expected from the inclusions deep subwavelength depth. In Figure 3c,d, we show the phase (Figure 3c) and reflection (Figure 3d) obtained by FDTD simulations (Lumerical). For simulation details, see the Supporting Information, Section S3. The good agreement between measurements and simulation is evident.

Next, we show measurements in transmission mode of a metasurface comprised of gold split-ring resonators. The inset of Figure 4a shows a scanning electron microscope (SEM)

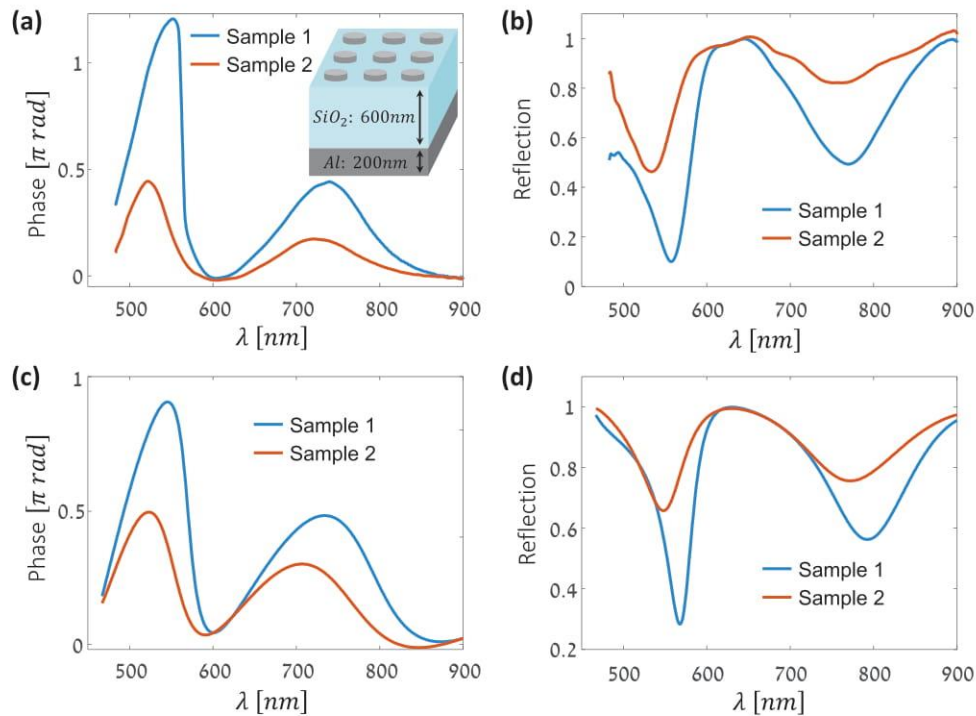


Figure 3. Measurements of a metasurface in reflection mode. a) Phase and b) reflection of the metasurface, for two samples with different geometrical parameters. The inset of (a) shows schematic illustration of the sample. The associated FDTD simulations of the phase and reflection are shown in (c) and (d), respectively.

image of the fabricated sample (for the sample's geometrical parameters, see the Supporting Information, Section S3). In Figure 4a, we present the broadband phase measurements for two angles of incidence: $\theta = 0^\circ$ (blue line) and $\theta = 30^\circ$ (orange line). Figure 4b shows the corresponding transmission measurements. It can be seen from the transmission that for normal incidence broad LSPR centered at ≈ 840 nm appears. The phase shows the associated phase change of the LSPR. The small phase range ($\approx 0.2 \pi$ rad) is due to the transmitted light being a mixture of scattered light and noninteracting light. The measurements for $\theta = 30^\circ$ show two transmission dips centered around the peak at $\lambda \approx 906$ nm. The corresponding phase shows positive $d\phi/d\omega$ values at the two resonances with a sharp feature at the peak location of anomalous phase, i.e., large negative $d\phi/d\omega$ values. This phase trend reveals the existence of slow light that accompanies the high transmission value, an indication for an EIT-like behavior. These EIT-like features arise due to the interaction of the individual plasmonic particles with a lattice mode, as further described in ref. [41]. For comparison, we also simulated the phase (Figure 4c) and transmission (Figure 4d) of the measured metasurface with FDTD solver. Simulation details can be found in the Supporting Information, Section S3. Good agreement between the measurements and simulations can be seen. The deviations can originate from slight differences between simulation geometrical and materials parameters and actual ones in the experiments. The measurements and simulations of this metasurface verify that indeed our method is capable of using collimated light illumination and extract sharp spectral features spanning a small ($<0.25 \pi$ rad) phase range.

3.3. Real-Time Dynamic Phase Measurements of Nematic LC under Optically Induced Conformation

In this section, we demonstrate the MICRO-SSRI method's capability to perform real-time dynamic broadband phase measurements, by tracking an optically induced nematic-isotropic LC transition. Schematic illustration of the optical configuration is shown in Figure 5a. A $L = 12 \mu\text{m}$, thick 4-cyano-4'-pentylbiphenyl (5CB) nematic LC layer oriented with its director horizontally, was pumped by a focused IR laser beam (1420 nm, ≈ 140 fs width at 80 MHz). Using two polarizers and a broadband half-wave plate mounted on a motorized rotational stage in between, the pump beam was set to be horizontally polarized and vary harmonically in intensity, as shown in Figure 5b,c, in accordance to

$$I(t) = \frac{1}{2} I_0 \left(1 + \cos\left(2\pi \frac{t}{T}\right) \right) \quad (4)$$

where t is the time, $I_0 = 67$ mW is the amplitude, and $T = 45$ s is the modulation period. Due to absorption of the laser beam and consequent heating of the LC, the LC can be optically driven to change its conformation between nematic and isotropic.[42] This leads to dynamic changes in the refractive index of the LC sample, which can be used to probe the dynamic material conformation.

The dynamically changing phase of a broadband optical probe beam transmitted through the device (see Figure 5a), was measured with the interferometer, and presented in Figure 5b. The probe beam was spanning the range of 450–1000 nm, with ≈ 2 mm radius on the LC sample. As shown in Figure 5a, the measurements were performed such that at

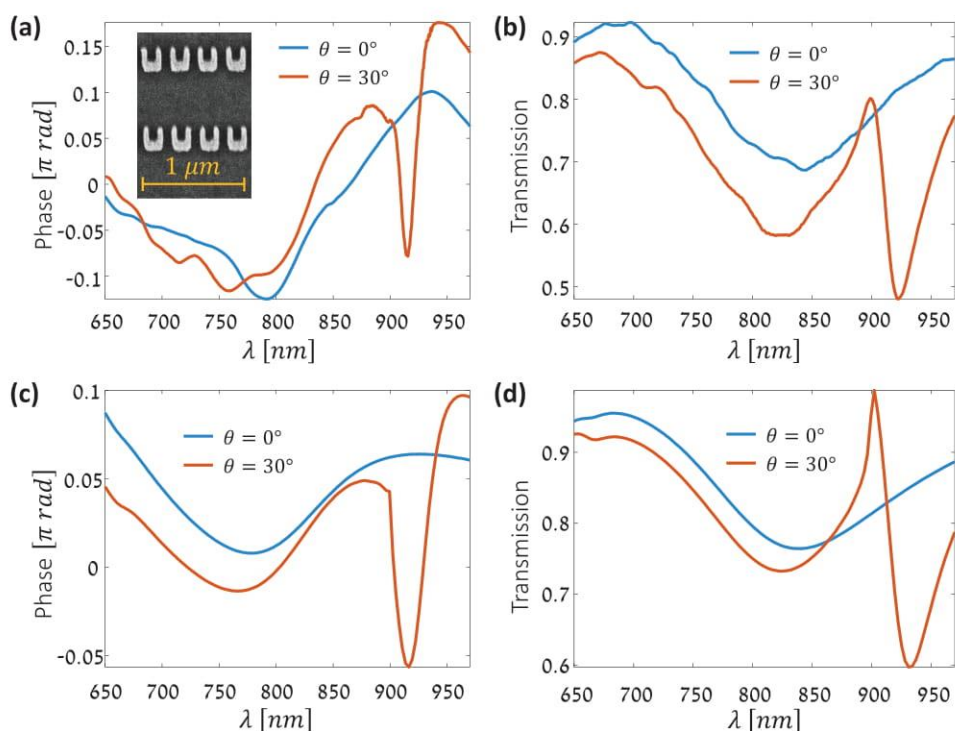


Figure 4. Angle-dependent measurements of a metasurface in transmission mode. The measured phase and transmission of the metasurface are shown in (a) and (b), respectively, for two angles of incidence: $\theta = 0^\circ$ (blue line) and $\theta = 30^\circ$ (orange line). The inset of (a) shows SEM image of the measured sample. The corresponding simulated phase and transmission are shown in (c) and (d), respectively.

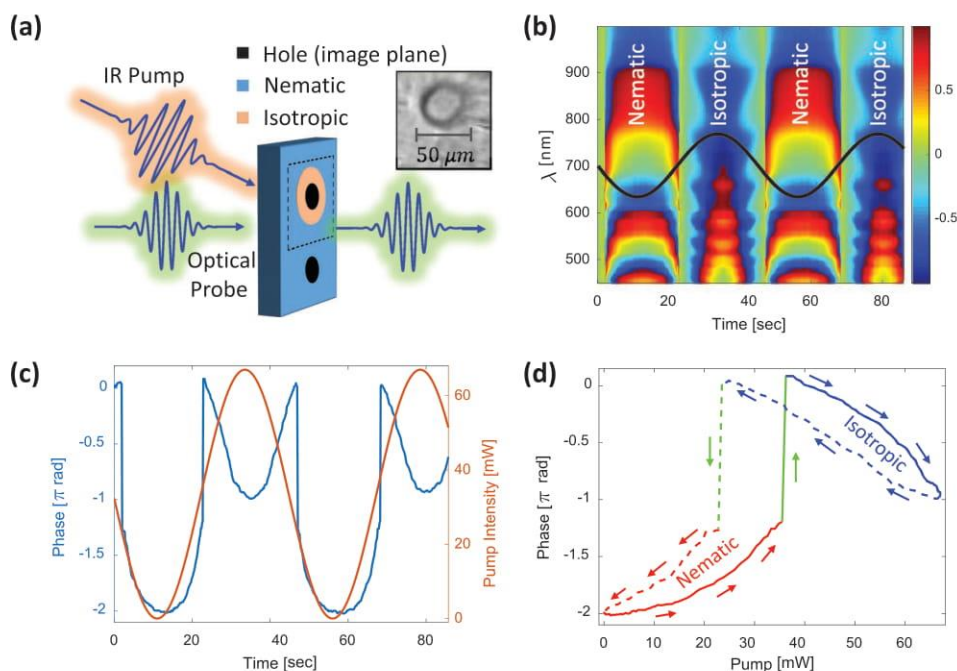


Figure 5. LC dynamics. a) Schematic illustration of the experimental configuration. Focused IR beam pumps the sample, and optical beam is used to probe the broadband time-resolved response. Without the pump beam, the LC is in its nematic state, while strong pump intensities can drive transitions to the isotropic state. The phase is measured at the central position of the focused pump beam. The inset shows an image of isotropic droplet formation of the LC with a circle of $\approx 20 \mu\text{m}$ radius. b) The spectrally and temporally resolved phase response of the LC. c) Cross-section of the phase response at $\lambda = 720 \text{ nm}$ (blue curve) and the pump intensity versus time (orange curve). d) Phase versus pump intensity of the LC for $\lambda = 720 \text{ nm}$. The hysteresis of the LC around the phase transitions is seen.

the image plane of the microscope, the upper hole was collecting light from the position of the incident IR beam while the lower hole was collecting light from a reference position that constantly stayed at the nematic state, $\approx 100 \mu\text{m}$ far from the center of the pump beam. The obtained temporally resolved sequence of interferograms was post-processed such that the initial interferogram was treated as the reference interferogram. Hence, the phase map in Figure 5b shows the phase differences of the LC at the focus of the IR pump, at a given time relative to the initial phase, acquired at $t = 0$ s. When the pump intensity reached a threshold value, the nematic LC abruptly underwent phase transition to the isotropic state. An image of the LC sample after this optically driven transition is shown in the inset of Figure 5a, where by a slightly defocused microscope image, a circle of $\approx 20 \mu\text{m}$ radius of the isotropic state is seen. In Figure 5b, we show the raw wrapped phase, to emphasize the rich physics reflected directly from the measurements, even without the assumptions required for the unwrapping. The obtained phase values correspond to 2π -modulus of

$$\Delta\phi(\lambda, t) = \Delta k(\lambda, t)L = \frac{2\pi}{\lambda} L(n(\lambda, t) - n^{\text{iso}}(\lambda, t=0)) \quad (5)$$

At $t = 0$ the measured area, i.e., the area at the pump location, was at its isotropic phase, thus the reference refractive index is $n^{\text{iso}}(\lambda, t = 0)$. It can be seen from Figure 5b that alternating domains, each with temporal width of ≈ 22.5 s, exist, corresponding to the nematic and isotropic states, as marked in the figure. These domains appear in accordance with the pump intensities, qualitatively showed by the black curve. For low intensities, the LC stays at the nematic state, while for high intensities transition to the isotropic state is driven.

The phase changes versus wavelength can be easily understood. For the nematic state, the relevant index of refraction is $n_o^{\text{nem}}(\lambda, t)$ for ordinary rays, due to the perpendicular orientation of the nematic LC director and the polarization of the probe beam. At the regions in Figure 5b corresponding to the nematic state, we see increasing phase values for increasing wavelength values. By examining Equation (5), we see that this can occur only if $n_o^{\text{nem}}(\lambda, t) < n^{\text{iso}}(\lambda, t = 0)$. Indeed, in accordance with the literature,^[43] $n_o^{\text{nem}}(\lambda, t)$ is smaller than $n^{\text{iso}}(\lambda, t = 0)$ for any temperature. On the other hand, to explain the same phase trend at the isotropic state regions, we must account for the change in the temperature of the LC caused by the pump beam. If we assume that the temperature changes with proportion to the intensity of the pump beam, though with some potential time delay t_d , we can write $T(t) = T_{\text{DC}} + T_0 \cos(2\pi f(t + t_d))$, with T_{DC} being the DC temperature term and T_0 the amplitude of the modulation. Thus, it is now evident that the coolest temperature of LC in the isotropic phase should be in vicinity to the phase transitions. Therefore, as the reference interferogram at $t = 0$ s was taken at the isotropic state just before the isotropic-nematic transition, any further interferogram acquired in the isotropic state corresponds to higher temperature. As expected, the refractive index of the isotropic state descends with temperature.^[43] Thus, $n(\lambda, t) - n^{\text{iso}}(\lambda, t = 0) < 0$ for any interferogram of the isotropic state in the sequence, confirming the observation of the positive phase slope versus wavelength at Figure 5b. The wiggly trend accompanying the

phase versus wavelength at the isotropic states, appears due to diffraction from the circular aperture caused by the isotropic state (see inset of Figure 5a), and may be used to track the spatial evolution of the transition.

To further analyze also the temporal dependence of the phase, in Figure 5c we show a cross-section of the phase versus the time for $\lambda = 720$ nm. The abrupt optical phase jumps that accompany the LC phase transitions are evident, while each state of the LC shows a convex trend of the optical phase. These trends can be understood by the temperature-dependent refractive index of the LC. By examining Equation (5), we see that the only time-dependent term in $\Delta\phi(\lambda, t)$ is $n(\lambda, t)$. By accounting for the time-dependent temperature $T(t)$, for any wavelength λ , we obtain the relation $\Delta\phi(\lambda, t) \propto n(\lambda, T_0 \cos(2\pi f(t + t_d)))$. It is known from the literature^[43] that $n_o^{\text{nem}}(\lambda, T)$ and $n^{\text{iso}}(\lambda, T)$ increase and decrease as a function of the temperature, respectively, i.e., $\frac{\partial n_o^{\text{nem}}(\lambda, T)}{\partial T} > 0$, and $\frac{\partial n^{\text{iso}}(\lambda, T)}{\partial T} < 0$. The conclusion that arises from the last two conditions about the trend of the refractive indices and their derivatives, is that the optical phase should follow a similar trend to the pump trend, though with opposite sign for the isotropic state. This exactly agrees with the observations from Figure 5c.

Finally, in Figure 5d, we also show the measured phase versus the pump intensity, for wavelength of $\lambda = 720$ nm. The arrows are pointing toward the direction of the device temporal evolution. The regions in red and blue correspond to the nematic and isotropic states, respectively, while the green region corresponds to the transition between these states. For any pump intensity, the phase takes one of two values, depending on the direction of the pump change, i.e., whether $\partial I(t)/\partial t$ is positive or negative. This behavior shows the out-of-thermal-equilibrium hysteresis of the LC.

We stress here an important point regarding temporal dynamics measurements attainable with the MICRO-SSRI method. As demonstrated in this section, the method can be used for real-time characterizations. The temporal resolution of these characterizations is limited by the speed of the camera that is used, as the system has no mechanical moving parts. The limiting factor in our case was the readout rate of the imaging spectrometer's camera (Andor Newton 970), which enabled cycle time no shorter than 0.15 s. In cases where higher temporal resolution is required, one can also implement the MICRO-SSRI method within a pump-probe type experiment.^[44] For this, the three-beam interference approach (see the Supporting Information, Section S4) can be particularly suited as it enables to obtain in only a single acquisition stabilized measurements.

The presented example given in this section, for real-time dynamical broadband phase characterization, shows the MICRO-SSRI method's suitability for studies concerned with temporal dynamics, highly relevant for the design of active optically controlled device applications.

4. Noise and Resolution Analysis

For the static and dynamic measurements presented in this paper, there are two types of associated noise. The static measurements, used in Sections 3.1 and 3.2, rely on two successive

acquisitions (see Figure 1c), and the dynamic measurements, used in Section 3.3, are based on acquiring multiple successive interferograms and referring to the first interferogram as a reference. We refer to these two types of measurements as moving reference interferogram (MRI) and a constant reference interferogram (CRI), respectively. To estimate the temporal noise for these two types of measurements, we performed 540 successive acquisitions, equally spaced by 20 s. To calculate the standard deviation (SD) for the case of MRI, we referred to every two successive acquisitions as a couple of reference–reference and reference–sample interferograms, according to the description in Sections 2. To calculate the CRI, we refer in all measurements to the first captured frame as reference–reference interferogram. Even though the environmental conditions of the setup were not ideal including open setup and vicinity to closed-loop air-conditioning engines, we found very good SD values. For both the MRI and CRI, the SD was smaller than 0.01π rad. These values, influenced by various sources of vibrations, can be substantially improved by better isolations of the system. We can further improve the interferometer stability by relying on three-beam interference^[33,45] within only a single acquisition (see the Supporting Information, Section S4). The method's spectral resolution is determined by the imaging spectrometer spectral resolution. In our case, it was ≈ 0.13 nm and can also be improved by using a system with better resolution. The spatial resolution of the method is limited by the resolution of the microscope's objective lens, often defined as $\frac{\lambda}{2 \cdot \text{NA}}$, where NA

is the numerical aperture. To meet this limit, the diameter of the holes at the double-hole mask should be smaller than the multiplication of the objective lens's resolution and magnification. In our implementation of the technique, the holes diameter was $\approx 10 \mu\text{m}$, the NA was 0.4, and the magnification was 20 and 50, for the measurements in transmission and reflection, respectively. Thus, over the entire measured range indeed the spatial resolution was determined by the objective lens.

5. Conclusions

We have presented the MICRO-SSRI method to obtain the spectral phase and amplitude of a microscopic sample, either in reflection or transmission. The MICRO-SSRI overcomes long standing limitations in the field of microscopy interferometry by offering a new approach of spatially filtering the collected light at the image plane of a microscope and imaging the Fourier plane of the filtered image on the entrance slit of an imaging spectrometer. This approach enables flexible sample illumination, stable and easy-to-align single, or double acquisition spectral phase extraction by only slightly modifying a typical spectroscopy microscope setup. We experimentally demonstrated the new method in measuring the phase response of metasurface samples both in reflection and transmission and showed good agreement between the simulated and measured phases. We also demonstrated the method's capability of dynamic measurements by real-time tracking the phase and amplitude of transmitted light through a nematic LC undergoing a phase transition from nematic to isotropic. Additionally, we offer a route to further decrease the noise and enhance the

interferometer stability by referring to a triple-hole mask and in only a single acquisition using the technique of three-beam interference. We believe that the MICRO-SSRI method will be useful for both microscopic and macroscopic optical material characterization. It may show special advantage for characterization of metasurfaces or 2D material. Furthermore, the opportunity to spectrally measure phase of dynamic processes with a stable and easy to align setup will be beneficial for the study of various biological, chemical, and physical processes.

Supporting Information

Supporting Information is available from the Wiley Online Library or from the author.

Acknowledgements

This publication is part of a project that has received funding from the European Research Council (ERC) under the European Union's Horizon 2020 research and innovation programme (grant agreement no. 715362 and grant agreement no. 639402), and by the Ministry of Science, Technology and Space, Israel (grant agreement no. 3-15614).

Conflict of Interest

The authors declare no conflict of interest.

Keywords

interferometers, liquid crystals, metasurfaces, optical characterization, real-time dynamics

Received: February 25, 2020

Revised: April 16, 2020

Published online:

- [1] V. M. Shalaev, W. Cai, U. K. Chettiar, H.-K. Yuan, A. K. Sarychev, V. P. Drachev, A. V. Kildishev, *Opt. Lett.* **2005**, *30*, 3356.
- [2] A. V. Kildishev, W. Cai, U. K. Chettiar, H.-K. Yuan, A. K. Sarychev, V. P. Drachev, V. M. Shalaev, *J. Opt. Soc. Am. B* **2006**, *23*, 423.
- [3] S. Zhang, W. Fan, N. C. Panoiu, K. J. Malloy, R. M. Osgood, S. R. J. Brueck, *Phys. Rev. Lett.* **2005**, *95*, 137404.
- [4] G. Dolling, C. Enkrich, M. Wegener, C. M. Soukoulis, S. Linden, *Science* **2006**, *312*, 892.
- [5] J. B. Pendry, *Phys. Rev. Lett.* **2000**, *85*, 3966.
- [6] S. Linden, C. Enkrich, G. Dolling, M. W. Klein, J. Zhou, T. Koschny, C. M. Soukoulis, S. Burger, F. Schmidt, M. Wegener, *IEEE J. Sel. Top. Quantum Electron.* **2006**, *12*, 1097.
- [7] A. I. Kuznetsov, A. E. Miroshnichenko, M. L. Brongersma, Y. S. Kivshar, B. Luk'yanchuk, *Science* **2016**, *354*, aag2472.
- [8] R. A. Shelby, D. R. Smith, S. Schultz, *Science* **2001**, *292*, 77.
- [9] J. B. Pendry, A. J. Holden, D. J. Robbins, W. J. Stewart, *IEEE Trans. Microwave Theory Tech.* **1999**, *47*, 2075.
- [10] J. Valentine, S. Zhang, T. Zentgraf, E. Ulin-Avila, D. A. Genov, G. Bartal, X. Zhang, *Nature* **2008**, *455*, 376.
- [11] P. Moitra, Y. Yang, Z. Anderson, I. I. Kravchenko, D. P. Briggs, J. Valentine, *Nat. Photonics* **2013**, *7*, 791.

- [12] R. Maas, J. Parsons, N. Engheta, A. Polman, *Nat. Photonics* **2013**, *7*, 907.
- [13] H. Suchowski, K. O'Brien, Z. J. Wong, A. Salandrino, X. Yin, X. Zhang, *Science* **2013**, *342*, 1223.
- [14] N. Liu, L. Langguth, T. Weiss, J. Kästel, M. Fleischhauer, T. Pfau, H. Giessen, *Nat. Mater.* **2009**, *8*, 758.
- [15] S. Zhang, D. A. Genov, Y. Wang, M. Liu, X. Zhang, *Phys. Rev. Lett.* **2008**, *101*, 47401.
- [16] Y. Yang, I. I. Kravchenko, D. P. Briggs, J. Valentine, *Nat. Commun.* **2014**, *5*, 5753.
- [17] L. Lepetit, G. Chériaux, M. Joffre, *J. Opt. Soc. Am. B* **1995**, *12*, 2467.
- [18] M. A. van Dijk, M. Lippitz, M. Orrit, *Phys. Rev. Lett.* **2005**, *95*, 267406.
- [19] D. Birkedal, J. Shah, *Phys. Rev. Lett.* **1998**, *81*, 2372.
- [20] A. P. Kovács, R. Szipöcs, K. Osvay, Z. Bor, *Opt. Lett.* **1995**, *20*, 788.
- [21] D. Meshulach, D. Yelin, Y. Silberberg, *J. Opt. Soc. Am. B* **1997**, *14*, 2095.
- [22] A. P. Kovács, K. Osvay, G. Kurdi, M. Görbe, J. Klebniczki, Z. Bor, *Appl. Phys. B: Lasers Opt.* **2005**, *80*, 165.
- [23] P. Bowlan, P. Gabolde, A. Shreenath, K. McGresham, R. Trebino, S. Akturk, *Opt. Express* **2006**, *14*, 11892.
- [24] P. Bowlan, P. Gabolde, R. Trebino, *Opt. Express* **2007**, *15*, 10219.
- [25] P. Bowlan, U. Fuchs, R. Trebino, U. D. Zeitner, *Opt. Express* **2008**, *16*, 13663.
- [26] H. Valtna-Lukner, P. Bowlan, M. Löhmus, P. Piksarv, R. Trebino, P. Saari, *Opt. Express* **2009**, *17*, 14948.
- [27] J. Cohen, P. Bowlan, V. Chauhan, R. Trebino, *Opt. Express* **2010**, *18*, 6583.
- [28] Z. Guang, M. Rhodes, M. Davis, R. Trebino, *J. Opt. Soc. Am. B* **2014**, *31*, 2736.
- [29] A. Borzsonyi, A. Kovacs, K. Osvay, *Appl. Sci.* **2013**, *3*, 515.
- [30] A. Börzsönyi, A. P. Kovács, M. Görbe, K. Osvay, *Opt. Commun.* **2008**, *281*, 3051.
- [31] K. O'Brien, N. D. Lanzillotti-Kimura, H. Suchowski, B. Kante, Y. Park, X. Yin, X. Zhang, *Opt. Lett.* **2012**, *37*, 4089.
- [32] S. D. Gennaro, Y. Sonnefraud, N. Verellen, P. Van Dorpe, V. V. Moshchalkov, S. A. Maier, R. F. Oulton, *Nat. Commun.* **2014**, *5*, 3748.
- [33] A. J. Ollanik, G. Z. Hartfield, Y. Ji, J. T. Robertson, K. Islam, M. D. Escarra, *Adv. Opt. Mater.* **2019**, *7*, 1901128.
- [34] D. R. Smith, D. C. Vier, T. Koschny, C. M. Soukoulis, *Phys. Rev. E: Stat., Nonlinear, Soft Matter Phys.* **2005**, *71*, 36617.
- [35] S. Arslanagic, T. V. Hansen, N. A. Mortensen, A. H. Gregersen, O. Sigmund, R. W. Ziolkowski, O. Breinbjerg, *IEEE Antennas Propag. Mag.* **2013**, *55*, 91.
- [36] Z. Szabó, G. H. Park, R. Hedge, E. P. Li, *IEEE Trans. Microwave Theory Tech.* **2010**, *58*, 2646.
- [37] V. G. Kravets, A. V. Kabashin, W. L. Barnes, A. N. Grigorenko, *Chem. Rev.* **2018**, *118*, 5912.
- [38] L. Michaeli, S. Keren-Zur, O. Avayu, H. Suchowski, T. Ellenbogen, *Phys. Rev. Lett.* **2017**, *118*, 243904.
- [39] SCHOTT Zemax catalog, https://refractiveindex.info/download/data/2017/schott_2017-01-20b.agf (accessed: May 2020).
- [40] A. Berkhout, A. F. Koenderink, *ACS Photonics* **2019**, *6*, 2917.
- [41] L. Michaeli, H. Suchowski, T. Ellenbogen, *Laser Photonics Rev.* **2020**, *14*, 1900204.
- [42] I. C. Khoo, *Phys. Rep.* **2009**, *471*, 221.
- [43] J. Li, S. Gauza, S. T. Wu, *J. Appl. Phys.* **2004**, *96*, 19.
- [44] M. C. Fischer, J. W. Wilson, F. E. Robles, W. S. Warren, *Rev. Sci. Instrum.* **2016**, *87*, 031101.
- [45] K. Almarzouk, *Appl. Opt.* **1983**, *22*, 1893.

ADVANCED OPTICAL MATERIALS

Supporting Information

for *Adv. Optical Mater.*, DOI: 10.1002/adom.202000326

Spectral Interferometric Microscopy for Fast and Broadband
Phase Characterization

Lior Michaeli, Danielle Ben Haim, Mukesh Sharma, Haim
Suchowski, and Tal Ellenbogen*

Supporting Information

Spectral Interferometric Microscopy for Fast and Broadband Phase Characterization

Lior Michaeli [1-3] *, Danielle Ben Haim [1,3], Mukesh Sharma [1,3], Haim Suchowski [2,3], Tal Ellenbogen [1,3]

S1. Setup description

The elaborated setup description for the measurement of both reflection and transmission amplitude and phase is shown in **Figure S1**.

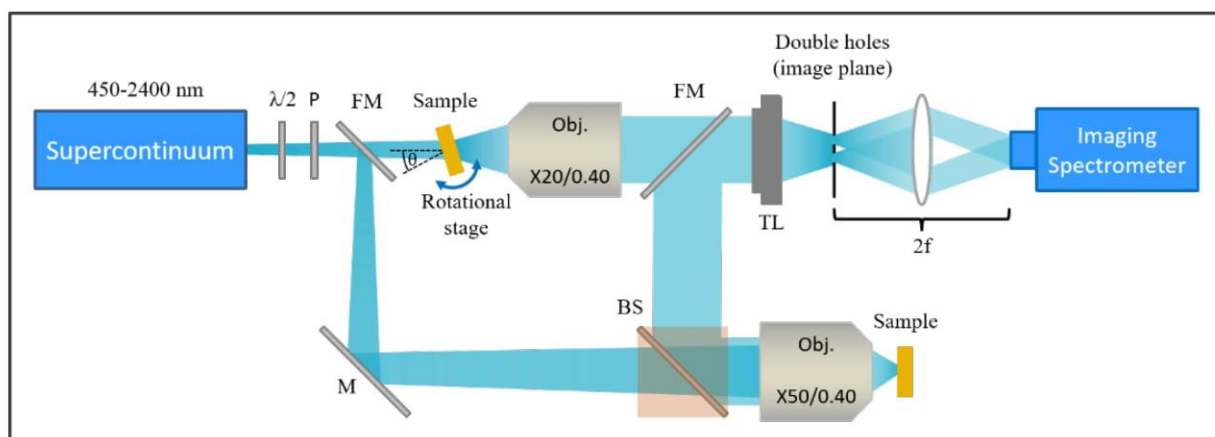


Figure S1. The experimental setup for the reflection and transmission phase and amplitude measurements. The common parts of the transmission and reflection paths of the setup comprised a supercontinuum source, half-wave plate ($\lambda/2$) and a polarizer (P) at its beginning and a double-hole mask, $2f$ system, and an imaging spectrometer at its end. The transmission path included in-between a sample on a rotational stage, and objective lens (Obj.). The switch to the reflection mode was done by the two flip mirrors (FM), while in-between there was a mirror (M) beam splitter (BS), objective lens (Obj.) and a sample.

S2. Theoretical background

S2.1 The broadband interferogram formation

Here we formulate the theoretical background of the broadband interferogram generation. For simplicity, we consider the electric fields as scalars, while generally the vectorial nature of the fields can be accounted for by repeating the acquisition and post-processing for each polarization. According to Figure 1b, the origin of coordinates will be taken on the optical axis at the center between the double holes. The fields are recorded and analyzed at the Fourier plane located at $z = 2f$. Say we want to extract the spectral phase information of the image at a point (x, y) . For brevity we denote this point by S. The phase will be extracted relative to two identical points at the reference area (see Figure 1c), denoted by R. We also denote the upper hole H_1 and the lower hole H_2 . Light emitted from H_1 and H_2 will have at $z = 2f$ the following plane wave form:

$$E_{H_1} = E_{H_1}^{(0)} e^{-i(\vec{k}_{H_1} \cdot \vec{r} - \omega(t-t_0))} \quad (\text{S1a})$$

$$E_{H_2} = E_{H_2}^{(0)} e^{-i(\vec{k}_{H_2} \cdot \vec{r} - \omega(t-t_0))} \quad (\text{S1b})$$

Where $\vec{r} = (x, y, z)$ is the position vector. The times t and t_0 are the time and an arbitrary time reference, accordingly, which as we will see will not play any role in the calculations due to cancelation at the detector. \vec{k}_{H_1} and \vec{k}_{H_2} are the k-vectors describing the slightly tilted planed waves that form due to the $2f$ system:

$$\vec{k}_{H_1} = (0, -k_y, k_z) \quad (\text{S2a})$$

$$\vec{k}_{H_2} = (0, k_y, k_z) \quad (\text{S2b})$$

and:

$$k_y = k \cdot \sin(\gamma) \quad (\text{S3a})$$

$$k_z = k \cdot \cos(\gamma) \quad (\text{S3b})$$

Where $k = \frac{2\pi}{\lambda}$ is the magnitude of the wavevector. The holes spacing denoted by l (see Figure 1b) determines the tilting angle:

$$\gamma = \text{atan}\left(\frac{l/2}{f}\right) \quad (\text{S4})$$

Where f is the focal lens of the lens used to image the Fourier plane of the double-hole mask (see Figure 1b). The fields $E_{H_1}^{(0)}$ and $E_{H_2}^{(0)}$ from Equations (S1) are the complex amplitudes of the electric fields passing through H_1 and H_2 , respectively. The fields get their contributions both from the illumination source E_{source} which is spatially uniform, and from the electric field complex transmission amplitude of the studied sample at H_1 and H_2 . These quantities are $T_{H_1}(\lambda)$ and $T_{H_2}(\lambda)$, respectively. Therefore $E_{H_1}^{(0)}$ and $E_{H_2}^{(0)}$ can be written as:

$$E_{H_1}^{(0)}(\lambda) = E_{source}(\lambda) T_{H_1}(\lambda) = \left| E_{source}^{(0)}(\lambda) T_{H_1}^{(0)}(\lambda) \right| e^{i\phi_{source}(\lambda)} e^{i\phi_{H_1}(\lambda)} \quad (\text{S5a})$$

$$E_{H_2}^{(0)}(\lambda) = E_{source}(\lambda) T_{H_2}(\lambda) = \left| E_{source}^{(0)}(\lambda) T_{H_2}^{(0)}(\lambda) \right| e^{i\phi_{source}(\lambda)} e^{i\phi_{H_2}(\lambda)} \quad (\text{S5b})$$

An imaging spectrometer, with its entrance slit placed at a distance of $z = 2f$ from the double-holes mask, is used to capture the interference pattern of the fields described in Equations (S1)-(S5). The imaging spectrometer is equipped with a diffraction grating that disperses the light along its horizontal axis to the different spectral components followed by a CCD detector. Thus, the x-axis of the imaging spectrometer is devoted to spectral information and the y-axis to spatial information. In the case of uncalibrated system two acquisitions, rather than one, are required. Working by this scheme further relax the need for fine alignment of the optical setup. These two acquisitions are depicted in Figure 1c. In the first

acquisition H_1 and H_2 transmit light from the reference (R) area. In the second acquisition the double-hole mask is moved such that H_1 transmits light from the reference (R) and H_2 from the sample (S). As the counts on the camera sensor are proportional to the light intensity falling on it, for the two above cases we measure:

$$\begin{aligned}
 I_{captured}^{RR}(\lambda, y) &= |E_{H_1,R} + E_{H_2,R}|^2 = (E_{H_1,R} + E_{H_2,R})(E_{H_1,R}^* + E_{H_2,R}^*) \\
 &= |E_{H_1,R}^{(0)}|^2 + |E_{H_2,R}^{(0)}|^2 + E_{H_1,R}E_{H_2,R}^* + E_{H_1,R}^*E_{H_2,R} \\
 &= |E_{H_1,R}^{(0)}|^2 + |E_{H_2,R}^{(0)}|^2 + E_{H_1,R}^{(0)}E_{H_2,R}^{(0)*}e^{-2ik_y y} \\
 &\quad + E_{H_1,R}^{(0)*}E_{H_2,R}^{(0)}e^{2ik_y y}
 \end{aligned} \tag{S6a}$$

$$\begin{aligned}
 I_{captured}^{RS}(\lambda, y) &= |E_{H_1,R} + E_{H_2,S}|^2 = (E_{H_1,R} + E_{H_2,S})(E_{H_1,R}^* + E_{H_2,S}^*) \\
 &= |E_{H_1,R}^{(0)}|^2 + |E_{H_2,S}^{(0)}|^2 + E_{H_2,S}E_{H_1,R}^* + E_{H_1,R}E_{H_2,S}^* \\
 &= |E_{H_1,R}^{(0)}|^2 + |E_{H_2,S}^{(0)}|^2 + E_{H_1,R}^{(0)}E_{H_2,S}^{(0)*}e^{-2ik_y y} \\
 &\quad + E_{H_1,R}^{(0)*}E_{H_2,S}^{(0)}e^{2ik_y y}
 \end{aligned} \tag{S6b}$$

After explicitly writing in Equations (S6) the y -dependent phase according to each hole, for the sake of brevity, we can omit the notations H_1 and H_2 . By substituting Equations (S5) into Equations (S6) we get:

$$\begin{aligned}
 I_{captured}^{RR}(\lambda, y) &= |E_{source}^{(0)}(\lambda) T_R^{(0)}(\lambda)|^2 + |E_{source}^{(0)}(\lambda) T_R^{(0)}(\lambda)|^2 \\
 &\quad + |E_{source}^{(0)}(\lambda)|^2 |T_R^{(0)}(\lambda)|^2 e^{-2ik_y y} \\
 &\quad + |E_{source}^{(0)}(\lambda)|^2 |T_R^{(0)}(\lambda)|^2 e^{2ik_y y}
 \end{aligned} \tag{S7a}$$

$$\begin{aligned}
 I_{captured}^{RS}(\lambda, y) &= \left| E_{source}^{(0)}(\lambda) T_R^{(0)}(\lambda) \right|^2 + \left| E_{source}^{(0)}(\lambda) T_S^{(0)}(\lambda) \right|^2 \\
 &+ \left| E_{source}^{(0)}(\lambda) \right|^2 \left| T_R^{(0)}(\lambda) \right| \left| T_S^{(0)}(\lambda) \right| e^{i(\phi_R(\lambda) - \phi_S(\lambda))} e^{-2ik_y y} \quad (S7b) \\
 &+ \left| E_{source}^{(0)}(\lambda) \right|^2 \left| T_R^{(0)}(\lambda) \right| \left| T_S^{(0)}(\lambda) \right| e^{-i(\phi_R(\lambda) - \phi_S(\lambda))} e^{2ik_y y}
 \end{aligned}$$

These equations for $I_{CCD}^{RR}(\lambda, y)$ and $I_{CCD}^{RS}(\lambda, y)$ describe the data of the obtained interferograms. We see from Equation (S7b) that the information of interest, $\phi_S(\lambda) - \phi_R(\lambda)$, is encoded in the modulation at spatial frequency $2k_y$. The post-processing of these interferograms in order to extract this phase data is described in the following section.

S2.2 The broadband interferogram post processing and spectral phase extraction

In this section we describe the post-processing that is used in this work for the spectral phase extraction from the obtained interferograms according to Equation (S7). To extract the phase difference $\Delta\phi(\lambda)$ we convolve the interferograms from Equations (S7) with band-pass filter $H_{BP}(y)$ to filter the term modulated at spatial frequency $2k_y$:

$$(I_{captured}^{RR}(\lambda) \odot H_{BP})(y) = \pi \left| E_{source}^{(0)}(\lambda) \right|^2 \left| T_R^{(0)}(\lambda) \right|^2 e^{2ik_y y} \quad (S8a)$$

$$(I_{captured}^{RS}(\lambda) \odot H_{BP})(y) = \pi \left| E_{source}^{(0)}(\lambda) \right|^2 \left| T_R^{(0)}(\lambda) \right| \left| T_S^{(0)}(\lambda) \right| e^{i\Delta\phi(\lambda)} e^{2ik_y y} \quad (S8b)$$

Then, by dividing Equation (S8b) with Equation (S8a) we get their ratio:

$$r(\lambda) = \frac{\left| T_S^{(0)}(\lambda) \right|}{\left| T_R^{(0)}(\lambda) \right|} e^{i\Delta\phi(\lambda)} \quad (S9)$$

The absolute value of $r(\lambda)$ is the spectral field transmission (or reflection) and its phase is the wavelength dependent phase difference $\Delta\phi(\lambda)$ of interest.

We stress here that the y coordinate appearing from Equations (S6) to (S8) can directly be mapped to relative time delay τ between the two interfering beams. The relation between y and τ , under the assumption of $f \gg l$, reads:

$$\tau = \frac{yl}{fc} \quad (\text{S10})$$

Where c is the speed of light and f is the focal length of the lens used in the $2f$ system. This relation can either be seen from the interferogram spatial frequency according to the derivation above, or from geometrical optics considerations. Thus, the number of fringes appearing on the camera sensor of vertical length L_y will be:

$$N_{fringes} = \frac{Ll}{f\lambda} \quad (\text{S11})$$

The accuracy of phase extraction increases with $N_{fringes}$.

S2.3 Aliasing and ambiguity in phase determination

The interferograms described in Equations (S7) are captured with a discretized sensor array, e.g. CCD. Therefore, two kind of aliasing can result from this discretization, associated with the two axes of the detector. The first aliasing condition, related to the y -axis of the detector can be derived from the requirement that each interference period along the y direction will be captured by at least two pixels. Writing it in terms of the setup parameters we get:

$$2l_{pix} < \lambda f \quad (\text{S12})$$

While l_{pix} is the pixel length. The second aliasing condition requires that between adjacent columns, i.e. adjacent wavelengths, there will be no more than 2π radians jumps of the phase difference:

$$|\Delta\phi(\lambda_0 + \Delta\lambda) - \Delta\phi(\lambda_0)| < 2\pi \quad (\text{S13})$$

While $\Delta\lambda$ denotes the spectrometer spectral resolution. In a typical interferometric measurement where $\Delta\phi$ is obtained at only a single wavelength, the condition $\Delta\phi < 2\pi$ must be satisfied in order to determine unambiguously the phase difference. In cases where more than 2π phase change is introduced various unwrapping algorithms^[1-4] or brunch determination methods^[5-7] are applied to attempt to uniquely determine $\Delta\phi$. Here we show that using our method, in some cases the phase can directly and unambiguously be obtained even for ranges of $\Delta\phi \gg 2\pi$. If we write explicitly the terms in Equation (S13) we obtain:

$$k_0 \left. \frac{dn(\lambda)}{d\lambda} \right|_{\lambda=\lambda_0} \Delta\lambda L < 2\pi \quad (\text{S14})$$

From here we can see that we gain a factor of $\frac{(n(\lambda)-n_{ref})}{\left. \frac{dn(\lambda)}{d\lambda} \right|_{\lambda=\lambda_0} \Delta\lambda}$ for the phase variation, where n_{ref} is the refractive index in the reference region. To give typical numbers to this value we can consider for example the case of weakly dispersive materials, such as glass, that satisfy $\left. \frac{dn(\lambda)}{d\lambda} \right|_{\lambda=\lambda_0} \Delta\lambda < 10^{-2} \text{ nm}^{-1}$, and take a typical value of $\Delta\lambda = 0.1 \text{ nm}$. For these conditions, when the reference region is in air, we get a factor larger then 10^3 times larger in the detectable phase variation compared to the common case of $\Delta\phi < 2\pi$. If we state it in terms of sample thickness, a layer about 1 mm thick can be measured within the full optical sub-cycle accuracy, directly, without the need for additional phase unwrapping. We demonstrate these striking capabilities in Section 3.1 of the main text.

S3. Sample's geometrical parameters for the reflective and transmissive metasurfaces

In Section 3.2 in the main text we presented measurements and FDTD simulation results of metasurfaces in reflection and in transmission. These metasurfaces, consisting of

$50 \mu\text{m} \times 50 \mu\text{m}$ squared array, were fabricated by a standard electron-beam lithography. The reflective metasurfaces consisted of a 600 nm layer of SiO_2 on top of a 200 nm layer of aluminum. A 40 nm thick aluminum nanodisks array were written on top of the SiO_2 layer. The radius and periodicity of samples 1 and 2 were $r = 73 \text{ nm}$, $d = 270$ and $r = 48 \text{ nm}$, $d = 240$, respectively. In the FDTD simulations the dimensions were $r = 73 \text{ nm}$, $d = 265 \text{ nm}$, and $r = 52 \text{ nm}$, $d = 225 \text{ nm}$, for samples 1 and 2, respectively.

The transmissive metasurfaces were comprised of a squared gold SRRs array. The array x and y-spacing was $d_x = 270 \text{ nm}$ and $d_y = 800 \text{ nm}$, respectively. Each SRR had 190 nm base-length, 225 nm arms-length, 55 nm arms-width, 95 nm base-width, and thickness of 40 nm . The sample was covered by immersion oil ($n = 1.51$), to obtain symmetric refractive index environment. In the FDTD simulations the physical dimensions of the SRRs were: 170 nm base-length, 200 nm arms-length, 50 nm arms-width, 95 nm base-width and thickness of 40 nm .

S4. Three-beam interference for reduction of acquisition noise

The idea is based on using a triple-hole mask with two reference holes and a sample hole. In this way the obtained interferogram will be composed of three different periodicities which enable, by Fourier analysis similar to the described in Section 2 of the main text, the extraction of the relative phase of the light passing through every pair of holes. We can write the phase extracted from every two holes H_i and H_j ($i, j = [1,2,3]$) as a part originating from the sample under inspection, $\Delta\phi_{H_i,H_j}^{wanted}$, plus a residual part $\Delta\phi_{H_i,H_j}^{unwanted}$ that originates from noise associated with small differences in the optical path:

$$\Delta\phi_{H_i,H_j} = \Delta\phi_{H_i,H_j}^{wanted} + \Delta\phi_{H_i,H_j}^{unwanted} \quad (\text{S15})$$

Thus, in the triple-hole case we will extract simultaneously the phases of the reference-sample and the reference-reference such that:

$$\Delta\phi_{R,S} = \Delta\phi_{R,S}^{wanted} + \Delta\phi_{R,S}^{unwanted} \quad (\text{S16a})$$

$$\Delta\phi_{R_1,R_2} = \Delta\phi_{R_1,R_2}^{unwanted} \quad (\text{S16b})$$

Where Equation (S16a) can be obtained by averaging the phase extracted from the sample hole relative to each of the references holes for better accuracy. Equation (S16b) contain only the unwanted phase term because the paths of the two references beams are the same at the object plane. Hence, subtraction of Equation (S16b) from Equation (S16a), gives only the desired phase term with better time stability and reduced noise and drift.

References

- [1] C. Zou, L.Huang, M. Zhang, Q. Chen, and A. Asundi, *Opt. Lasers Eng.* **2016**, 85, 84.
- [2] M. A. Herráez, D. R. Burton, M. J. Lalor, and M. A. Gdeisat, *Appl. Opt.*, **2002**, 41, 7437.
- [3] D. C. Ghiglia, and M. D. Pritt, Two-Dimensional Phase Unwrapping: Theory, Algorithms, and Software, **1998**.
- [4] N. A. Turko, and N. T. Shaked, *Opt. Lett.*, **2017**, 42, 73.
- [5] X. Chen, T. M. Grzegorzcyk, B. I. Wu, J. Pacheco, and J. A. Kong, *Phys. Rev. E*, **2004**, 70, 7.
- [6] Z. Szabó, G. H. Park, R. Hedge, and E. P. Li, *IEEE Trans. Microwave Theory Tech.*, **2010**, 58, 2646.
- [7] S. Arslanagić, T. V. Hansen, N. A. Mortensen, A. H. Gregersen, O. Sigmund, R. W. Ziolkowski, and O. Breinbjerg, *IEEE Antennas Propag. Mag.*, **2013**, 55, 91.

Chapter 3 **SUMMARY AND OUTLOOK**

In this thesis we explored collective coherent interactions of light with metallic nanoparticle arrays. We specifically focused on several aspects: manifestation of the coupling between the constituting nanoparticles on the nonlinear optical response, harnessing the collective interaction to affect the temporal dynamics of short pulses, and development of a corresponding phase characterization tool that was essential for our studies. In the following, we shortly summarize each of the presented works, and then provide an outlook for this thesis.

In section 2.1 we showed that collective interaction of nanoparticles can greatly affect the nonlinear response. Specifically, we demonstrated how coherent interaction at the SH frequency substantially enhance the nonlinear generation efficiency. This enhancement occurs according to a new resonant condition in plasmonic nanoparticle arrays, called nonlinear SLR (NL-SLR). The NL-SLR emerges from nonlinear photonic-plasmonic hybridization, which occurs when these modes spectrally coincide. The nonlinear photonic mode, called nonlinear RA, is a distributed mode associated with coherent diffraction of the nanoparticles along the surface of the array, at the nonlinear harmonic frequency. On the other hand, the plasmonic mode is a localized mode, emerging from the collective oscillations of the free electrons at the nonlinear harmonic frequency in each of the nanoparticles. To theoretically investigate these observations, we introduced a treatment based on extension of the CDA to the nonlinear regime. Specifically, for the case of infinite array we obtained a closed form solution for the second-order polarization of the nanoparticles. The resulting expression generalizes the behavior of the nonlinear response described by Miller's rule [95,102] and predicts the existence of the NL-SLRs. Furthermore, we also showed analogy between our nonlinear results and the historical Wood's anomalies observed in 1902 for linear diffraction from metallic gratings [134]. In addition, the presented theoretical treatment provides a framework to understand variations in the spectral nonlinear response of nanoparticle arrays also due to non-coherent coupling, e.g. near-field coupling, as was previously experimentally observed [100].

Following the publication presented in section 2.1 and the demonstration of nonlinear enhancement by linear SLR [101], numerous works have studied control and enhancement of the optical nonlinear response by of collective interactions [135–142]. For example, in O. Doron et al. [135] we obtained an explicit expression for the third-order polarization in plasmonic nanoparticle arrays and showed that judicious design cause an intriguing interference between the direct and cascaded third-harmonic generation; S. Chen et al. [138] demonstrated strong nonlinear optical activity induced by SLRs; and D. C. Hooper et al. [136] measured 450-fold enhancement of the SHG thanks to collective effects.

The second manuscript presented in this thesis, in section 2.2, deals with generation of tunable transparency and slow light windows in plasmonic nanoparticle arrays, induced by collective coherent interaction. We showed how coupling between the particles' LSPR and the lattice RA

resembles the coupling dynamics of the resonances responsible for the well-known phenomenon of EIT. The corresponding spectral transmission line shape consisted of two transmission dips with a narrow peak in the middle that reaches over 90 percent transmission. Attractively, this peak is associated also with slow light behavior, as theoretically predicted by the CDA and experimentally measured by the interferometric method presented in section 2.3. The slow-down factor that we achieved was ~ 60 over a wide tunable spectral range of ~ 200 nm, in the near-infrared spectral range. The presented mechanism to obtain tunable slow light with nano scale devices, i.e. metasurfaces, may find important realizations for on-chip all-optical signal processing, sensing, displays and tunable filtering.

Finally, in section 2.3, we introduced a novel interferometric method for fast and broadband microscopic phase characterization, based on common-path configuration. We experimentally demonstrated the new method by performing several challenging measurements with high accuracy. Among these, we measured the phase response of metasurfaces both in reflection and transmission. In addition, we showed the method's capability of dynamic measurements by real-time tracking the phase and amplitude of light transmitted through a nematic LC undergoing a phase transition to the isotropic state. The presented method is highly suitable for measuring collective coherent effects in metasurfaces, as it enables collimated illumination conditions, which are essential for the associated spectral features to appear. In addition, the opportunity to spectrally measure phase of dynamic processes with a stable and easy to align setup may be beneficial for the study of various biological, chemical, and physical processes.

As an outlook, we wish to connect the research presented in this work to a broader scientific scope. The interaction of many, well characterized, individuals is the foundation of numerous systems spanning different branches of science, from earthquakes to ecosystems, neurons to neutrinos [143]. The investigation of these systems, typically referred to as networks, has revealed fascinating dynamics. For example, some intriguing phenomena that are being investigated include phase transitions and their temporal analogue [144], synchronization, chaotic dynamics and different stability states [143], pattern formation [145], spontaneous symmetry breaking and chimera states [146–148]. In the case of metasurfaces, there is a high degree of flexibility in the design of both the individual building block's response, and the interaction between them. Therefore, we believe that inspiration from other research fields calls for scientific cross-fertilization and exploration of analogous phenomena in metasurfaces [149]. Specifically, we outline some potentially attractive research directions. First, as networks often become extremely interesting when nonlinear dynamics govern their response, exploration of collective nonlinear interactions in metasurfaces, outside the regime of the undepleted pump approximation, can be highly attractive. This regime can possess nontrivial stability states, chaotic dynamics, and can also be beneficial for supporting mirrorless OPO by distributed

feedback mechanism and generation of entangled photon pairs. Furthermore, the inspiration from other networks, along with scientific curiosity, also motivates the investigation of finite-size effects, temporal dynamics, active control, higher order nonlinear processes, and nontrivial topological states in metasurfaces governed by the collective interactions.

On the technological level, understanding and controlling the complex collective dynamics of metasurfaces can be highly beneficial for a variety of applications, thanks to the associated high-quality factors, spectrally narrow linewidths and enhanced near fields. For example, the collective resonances have proved attractive for lasing [150–153], sensing [83,154–156], photovoltaics [157,158], modulators [159,160] and displays [161,162]. In addition, the associated dynamics has potential for applications in communications [163], optoelectronics [164], data storage [76,165] and all-optical signal processing [166]. Therefore, as more knowledge and control techniques in this thriving research area accumulate, along with improvement in fabrication methods to enable high-quality and large-scale fabrications, real-life devices will potentially emerge, enabling the integration within and improvement of existing state-of-the-art developments.

To summarize, we believe that the research area of collective dynamics in nanostructured materials has a promising future, from both the fundamental scientific and technological applicative aspects. By cross-field fertilization and physical integration with other platforms for nanoscale light manipulation, this research area is expected to further grow, and yield significant discoveries and developments.

LIST OF PUBLICATIONS

This thesis is detailed in several peer-reviewed articles which can be turned to for further reading:

- B.H. Danielle, Michaeli, L., Avayu. O., Ellenbogen, T., "Tuning the phase and amplitude response of plasmonic metasurface etalons". *Optics Express*, 28, 17923, (2020).
- Michaeli, L., B.H. Danielle, S. Mukesh, Suchowski, H., Ellenbogen, T., "Spectral Interferometric Microscopy for Fast and Broadband Phase Characterization". *Advanced Optical Materials*, 2000326, (2020).
- Michaeli, L., Suchowski, H., Ellenbogen, T. "Near-Infrared Tunable Surface Lattice Induced Transparency in Plasmonic Metasurfaces". *Laser & Photonics Reviews*, 14, 1900204, (2019).
- Doron, O., Michaeli, L., and Ellenbogen, T. "Direct and cascaded collective third-harmonic generation in metasurfaces." *JOSA B*, 36.7, E71, (2019).
- Keren-Zur, S, Michaeli, L., Suchowski, H., Ellenbogen, T. "Shaping light with nonlinear metasurfaces". *Advances in Optics and Photonics*, 10, 309, (2018).
- Michaeli, L., Keren-zur, S., Avayu. O., Suchowski, H., Ellenbogen, T. "Nonlinear Surface Lattice Resonance in Plasmonic Nanoparticles Arrays". *Physical Review Letters*, 118, 243904, (2017).
- Keren-Zur, S., Avayu, O., Michaeli, L., & Ellenbogen, T. "Nonlinear beam shaping with plasmonic metasurfaces". *ACS Photonics*, 3, 117, (2016).

REFERENCES

- [1] J. B. Pendry, A. J. Holden, D. J. Robbins, and W. J. Stewart, *Magnetism from Conductors and Enhanced Nonlinear Phenomena*, IEEE Trans. Microw. Theory Tech. **47**, 2075 (1999).
- [2] M. W. Klein, C. Enkrich, M. Wegener, and S. Linden, *Second-Harmonic Generation from Magnetic Metamaterials.*, Science (80-.). **313**, 502 (2006).
- [3] K. O'Brien, H. Suchowski, J. Rho, A. Salandrino, B. Kante, X. Yin, and X. Zhang, *Predicting Nonlinear Properties of Metamaterials from the Linear Response*, Nat. Mater. **14**, 379 (2015).
- [4] N. Segal, S. Keren-Zur, N. Hendler, and T. Ellenbogen, *Controlling Light with Metamaterial-Based Nonlinear Photonic Crystals*, Nat. Photonics **9**, 180 (2015).
- [5] L. Michaeli, S. Keren-Zur, O. Avayu, H. Suchowski, and T. Ellenbogen, *Nonlinear Surface Lattice Resonance in Plasmonic Nanoparticle Arrays*, Phys. Rev. Lett. **118**, 243904 (2017).
- [6] M. T. and A. A. Alexander Krasnok, *Nonlinear Metasurfaces: A Paradigm Shift in Nonlinear Optics*, Mater. Today (2017).
- [7] S. Ayas, H. Güner, B. Türker, O. Ö. Ekiz, F. Dirisaglik, A. K. Okyay, and A. Dâna, *Raman Enhancement on a Broadband Meta-Surface*, ACS Nano (2012).
- [8] N. Zhang, K. Liu, Z. Liu, H. Song, X. Zeng, D. Ji, A. Cheney, S. Jiang, and Q. Gan, *Ultrabroadband Metasurface for Efficient Light Trapping and Localization: A Universal Surface-Enhanced Raman Spectroscopy Substrate for "All" Excitation Wavelengths*, Adv. Mater. Interfaces (2015).
- [9] S. Romano, G. Zito, S. Managò, G. Calafiore, E. Penzo, S. Cabrini, A. C. De Luca, and V. Mocella, *Surface-Enhanced Raman and Fluorescence Spectroscopy with an All-Dielectric Metasurface*, J. Phys. Chem. C (2018).
- [10] P. Anger, P. Bharadwaj, and L. Novotny, *Enhancement and Quenching of Single-Molecule Fluorescence*, Phys. Rev. Lett. (2006).
- [11] A. Rose, T. B. Hoang, F. McGuire, J. J. Mock, C. Ciraci, D. R. Smith, and M. H. Mikkelsen, *Control of Radiative Processes Using Tunable Plasmonic Nanopatch Antennas*, Nano Lett. (2014).
- [12] S. Yuan, X. Qiu, C. Cui, L. Zhu, Y. Wang, Y. Li, J. Song, Q. Huang, and J. Xia, *Strong Photoluminescence Enhancement in All-Dielectric Fano Metasurface with High Quality Factor*, ACS Nano (2017).
- [13] E. Hendry, T. Carpy, J. Johnston, M. Popland, R. V. Mikhaylovskiy, A. J. Laphorn, S. M. Kelly, L. D. Barron, N. Gadegaard, and M. Kadodwala, *Ultrasensitive Detection and*

- Characterization of Biomolecules Using Superchiral Fields*, Nat. Nanotechnol. (2010).
- [14] W. Ma, H. Kuang, L. Xu, L. Ding, C. Xu, L. Wang, and N. A. Kotov, *Attomolar DNA Detection with Chiral Nanorod Assemblies*, Nat. Commun. (2013).
- [15] R. Schreiber, N. Luong, Z. Fan, A. Kuzyk, P. C. Nickels, T. Zhang, D. M. Smith, B. Yurke, W. Kuang, A. O. Govorov, and T. Liedl, *Chiral Plasmonic DNA Nanostructures with Switchable Circular Dichroism*, Nat. Commun. (2013).
- [16] N. Yu, F. Aieta, P. Genevet, M. A. Kats, Z. Gaburro, and F. Capasso, *A Broadband, Background-Free Quarter-Wave Plate Based on Plasmonic Metasurfaces*, Nano Lett. **12**, 6328 (2012).
- [17] F. Ding, Z. Wang, S. He, V. M. Shalaev, and A. V. Kildishev, *Broadband High-Efficiency Half-Wave Plate: A Supercell-Based Plasmonic Metasurface Approach*, ACS Nano **9**, 4111 (2015).
- [18] H. L. Zhu, S. W. Cheung, X. H. Liu, and T. I. Yuk, *Design of Polarization Reconfigurable Antenna Using Metasurface*, IEEE Trans. Antennas Propag. (2014).
- [19] M. X. Ren, W. Wu, W. Cai, B. Pi, X. Z. Zhang, and J. J. Xu, *Reconfigurable Metasurfaces That Enable Light Polarization Control by Light*, Light Sci. Appl. (2017).
- [20] S. M. Kamali, E. Arbabi, A. Arbabi, and A. Faraon, *A Review of Dielectric Optical Metasurfaces for Wavefront Control*, Nanophotonics.
- [21] L. Huang, S. Zhang, and T. Zentgraf, *Metasurface Holography: From Fundamentals to Applications*, Nanophotonics.
- [22] D. Lin, P. Fan, E. Hasman, and M. L. Brongersma, *Dielectric Gradient Metasurface Optical Elements*, Science (80-.). **345**, 298 (2014).
- [23] M. Khorasaninejad, A. Ambrosio, P. Kanhaiya, and F. Capasso, *Broadband and Chiral Binary Dielectric Meta-Holograms*, Sci. Adv. **2**, (2016).
- [24] P.-C. Li, Y. Zhao, A. Alù, and E. T. Yu, *Experimental Realization and Modeling of a Subwavelength Frequency-Selective Plasmonic Metasurface*, Appl. Phys. Lett. **99**, 221106 (2011).
- [25] F. Aieta, P. Genevet, M. A. Kats, N. Yu, R. Blanchard, Z. Gaburro, and F. Capasso, *Aberration-Free Ultrathin Flat Lenses and Axicons at Telecom Wavelengths Based on Plasmonic Metasurfaces*, Nano Lett. **12**, 4932 (2012).
- [26] X. Chen, L. Huang, H. Mühlenbernd, G. Li, B. Bai, Q. Tan, G. Jin, C.-W. Qiu, S. Zhang, and T. Zentgraf, *Dual-Polarity Plasmonic Metalens for Visible Light.*, Nat. Commun. **3**, 1198 (2012).
- [27] P. R. West, J. L. Stewart, A. V. Kildishev, V. M. Shalaev, V. V. Shkunov, F. Strohkendl, Y. A. Zakharenkov, R. K. Dodds, and R. Byren, *All-Dielectric Subwavelength Metasurface Focusing Lens*, Opt. Express **22**, 26212 (2014).

- [28] P. Törmä and W. L. Barnes, *Strong Coupling between Surface Plasmon Polaritons and Emitters: A Review*, Reports Prog. Phys. **78**, 013901 (2015).
- [29] E. Eizner, O. Avayu, R. Ditcovski, and T. Ellenbogen, *Aluminum Nanoantenna Complexes for Strong Coupling between Excitons and Localized Surface Plasmons*, Nano Lett. **15**, 6215 (2015).
- [30] G. Hajisalem, M. S. Nezami, and R. Gordon, *Probing the Quantum Tunneling Limit of Plasmonic Enhancement by Third Harmonic Generation*, Nano Lett. **14**, 6651 (2014).
- [31] W. Zhu, R. Esteban, A. G. Borisov, J. J. Baumberg, P. Nordlander, H. J. Lezec, J. Aizpurua, and K. B. Crozier, *Quantum Mechanical Effects in Plasmonic Structures with Subnanometre Gaps*, Nat. Commun. **7**, (2016).
- [32] P. Roelli, C. Galland, N. Piro, and T. J. Kippenberg, *Molecular Cavity Optomechanics as a Theory of Plasmon-Enhanced Raman Scattering*, (2016).
- [33] R. Chikkaraddy, B. De Nijs, F. Benz, S. J. Barrow, O. A. Scherman, E. Rosta, A. Demetriadou, P. Fox, O. Hess, and J. J. Baumberg, *Single-Molecule Strong Coupling at Room Temperature in Plasmonic Nanocavities*, Nature **535**, (2016).
- [34] R. A. Shelby, D. R. Smith, and S. Schultz, *Experimental Verification of a Negative Index of Refraction*, Science (80-.). **292**, 77 (2001).
- [35] T. K. Hakala, A. J. Moilanen, A. I. Väkeväinen, R. Guo, J.-P. Martikainen, K. S. Daskalakis, H. T. Rekola, A. Julku, and P. Törmä, *Bose–Einstein Condensation in a Plasmonic Lattice*, Nat. Phys. **14**, 739 (2018).
- [36] D. Smirnova, S. Kruk, D. Leykam, E. Melik-Gaykazyan, D. Y. Choi, and Y. Kivshar, *Third-Harmonic Generation in Photonic Topological Metasurfaces*, Phys. Rev. Lett. **123**, (2019).
- [37] S. Zanotto, G. Mazzamuto, F. Riboli, G. Biasiol, G. C. La Rocca, A. Tredicucci, and A. Pitanti, *Photonic Bands, Superchirality, and Inverse Design of a Chiral Minimal Metasurface*, Nanophotonics (2019).
- [38] S. R. K. Rodriguez, A. Abass, B. Maes, O. T. A. Janssen, G. Vecchi, and J. Gómez Rivas, *Coupling Bright and Dark Plasmonic Lattice Resonances*, Phys. Rev. X **1**, 1 (2011).
- [39] Y. Lahini, A. Avidan, F. Pozzi, M. Sorel, R. Morandotti, D. N. Christodoulides, and Y. Silberberg, *Anderson Localization and Nonlinearity in One-Dimensional Disordered Photonic Lattices*, Phys. Rev. Lett. **100**, (2008).
- [40] H. H. Sheinfux, Y. Lumer, G. Ankonina, A. Z. Genack, G. Bartal, and M. Segev, *Observation of Anderson Localization in Disordered Nanophotonic Structures*, Science (80-.). **356**, 953 (2017).
- [41] M. A. Gorlach, X. Ni, D. A. Smirnova, D. Korobkin, D. Zhirihin, A. P. Slobozhanyuk,

- P. A. Belov, A. Alù, and A. B. Khanikaev, *Far-Field Probing of Leaky Topological States in All-Dielectric Metasurfaces*, Nat. Commun. **9**, (2018).
- [42] E. Karimi, S. A. Schulz, I. De Leon, H. Qassim, J. Upham, and R. W. Boyd, *Generating Optical Orbital Angular Momentum at Visible Wavelengths Using a Plasmonic Metasurface*, Light Sci. Appl. **3**, (2014).
- [43] N. Yu and F. Capasso, *Flat Optics with Designer Metasurfaces*, Nat. Mater. **13**, 139 (2014).
- [44] P. Biagioni, J.-S. Huang, and B. Hecht, *Nanoantennas for Visible and Infrared Radiation.*, Rep. Prog. Phys. **75**, 024402 (2012).
- [45] N. Meinzer, W. L. Barnes, and I. R. Hooper, *Plasmonic Meta-Atoms and Metasurfaces*, Nat. Photonics **8**, 889 (2014).
- [46] S. Kruk and Y. Kivshar, *Functional Meta-Optics and Nanophotonics Govern by Mie Resonances*, ACS Photonics **4**, 2638 (2017).
- [47] P. Genevet and F. Capasso, *Holographic Optical Metasurfaces: A Review of Current Progress*, Reports Prog. Phys. **78**, 024401 (2015).
- [48] A. E. Minovich, A. E. Miroshnichenko, A. Y. Bykov, T. V. Murzina, D. N. Neshev, and Y. S. Kivshar, *Functional and Nonlinear Optical Metasurfaces*, Laser Photon. Rev. **9**, 195 (2015).
- [49] A. V Kildishev, A. Boltasseva, and V. M. Shalaev, *Planar Photonics with Metasurfaces*, Science **339**, 1232009 (2013).
- [50] A. Y. Zhu, A. I. Kuznetsov, B. Luk'yanchuk, N. Engheta, and P. Genevet, *Traditional and Emerging Materials for Optical Metasurfaces*, Nanophotonics **6**, 452 (2017).
- [51] J. Scheuer, *Metasurfaces-Based Holography and Beam Shaping: Engineering the Phase Profile of Light*, Nanophotonics.
- [52] H.-T. Chen, A. J. Taylor, and N. Yu, *A Review of Metasurfaces: Physics and Applications*, Reports Prog. Phys. **79**, 076401 (2016).
- [53] J. Wang and J. Du, *Plasmonic and Dielectric Metasurfaces: Design, Fabrication and Applications*, Appl. Sci. **6**, 239 (2016).
- [54] N. I. Zheludev and Y. S. Kivshar, *From Metamaterials to Metadevices*, Nat. Mater. **11**, 917 (2012).
- [55] S. B. Glybovski, S. A. Tretyakov, P. A. Belov, Y. S. Kivshar, and C. R. Simovski, *Metasurfaces: From Microwaves to Visible*, Physics Reports.
- [56] S. A. Maier, *Plasmonics : Fundamentals and Applications* (Springer, 2007).
- [57] S. Keren-Zur, L. Michaeli, H. Suchowski, and T. Ellenbogen, *Shaping Light with Nonlinear Metasurfaces*, Adv. Opt. Photonics **10**, 309 (2018).
- [58] G. Mie, *Beiträge Zur Optik Trüber Medien, Speziell Kolloidaler Metallösungen*, Ann.

- Phys. **330**, 377 (1908).
- [59] S. Asano and G. Yamamoto, *Light Scattering by a Spheroidal Particle*, Appl. Opt. **14**, 29 (1975).
- [60] C. F. Bohren and D. R. Huffman, *Absorption and Scattering of Light by Small Particles* (Wiley, 2004).
- [61] V. Myroshnychenko, J. Rodríguez-Fernández, I. Pastoriza-Santos, A. M. Funston, C. Novo, P. Mulvaney, L. M. Liz-Marzán, and F. J. García de Abajo, *Modelling the Optical Response of Gold Nanoparticles*, Chem. Soc. Rev. **37**, 1792 (2008).
- [62] T. Jensen, L. Kelly, A. Lazarides, and G. C. Schatz, *Electrodynamics of Noble Metal Nanoparticles and Nanoparticle Clusters*, J. Clust. Sci. **10**, 295 (1999).
- [63] L. Novotny, *Effective Wavelength Scaling for Optical Antennas.*, Phys. Rev. Lett. **98**, 266802 (2007).
- [64] B. Lamprecht, J. R. Krenn, A. Leitner, and F. R. Aussenegg, *Resonant and Off-Resonant Light-Driven Plasmons in Metal Nanoparticles Studied by Femtosecond-Resolution Third-Harmonic Generation*, Phys. Rev. Lett. **83**, 4421 (1999).
- [65] M. W. Knight, N. S. King, L. Liu, H. O. Everitt, P. Nordlander, and N. J. Halas, *Aluminum for Plasmonics.*, ACS Nano **8**, 834 (2014).
- [66] K. B. Crozier, A. Sundaramurthy, G. S. Kino, and C. F. Quate, *Optical Antennas: Resonators for Local Field Enhancement*, J. Appl. Phys. **94**, 4632 (2003).
- [67] Y. Chu, E. Schonbrun, T. Yang, and K. B. Crozier, *Experimental Observation of Narrow Surface Plasmon Resonances in Gold Nanoparticle Arrays*, Appl. Phys. Lett. **93**, 181108 (2008).
- [68] J. R. Krenn, G. Schider, W. Rechberger, B. Lamprecht, A. Leitner, F. R. Aussenegg, J. C. Weeber, and) G Schider, *Design of Multipolar Plasmon Excitations in Silver Nanoparticles*, **77**, (2000).
- [69] S. Link and M. A. El-Sayed, *Spectral Properties and Relaxation Dynamics of Surface Plasmon Electronic Oscillations in Gold and Silver Nanodots and Nanorods*, J. Phys. Chem. B **103**, 8410 (2002).
- [70] C. Rockstuhl, T. Zentgraf, H. Guo, N. Liu, C. Etrich, I. Loa, K. Syassen, J. Kuhl, F. Lederer, and H. Giessen, *Resonances of Split-Ring Resonator Metamaterials in the near Infrared*, Appl. Phys. B **84**, 219 (2006).
- [71] C. Rockstuhl, F. Lederer, C. Etrich, T. Zentgraf, J. Kuhl, and H. Giessen, *On the Reinterpretation of Resonances in Split-Ring-Resonators at Normal Incidence.*, Opt. Express **14**, 8827 (2006).
- [72] N. Yu, P. Genevet, M. A. Kats, F. Aieta, J.-P. Tetienne, F. Capasso, and Z. Gaburro, *Light Propagation with Phase Discontinuities: Generalized Laws of Reflection and*

- Refraction*, Science (80-.). **334**, 333 (2011).
- [73] H. Husu, J. Mäkitalo, J. Laukkanen, M. Kuittinen, and M. Kauranen, *Particle Plasmon Resonances in L-Shaped Gold Nanoparticles*, Opt. Express **18**, 16601 (2010).
- [74] B. Lamprecht, A. Leitner, and F. R. Aussenegg, *SHG Studies of Plasmon Dephasing in Nanoparticles*, Appl. Phys. B Lasers Opt. **68**, 419 (1999).
- [75] V. G. Kravets, A. V. Kabashin, W. L. Barnes, and A. N. Grigorenko, *Plasmonic Surface Lattice Resonances: A Review of Properties and Applications*, Chemical Reviews.
- [76] L. Michaeli, H. Suchowski, and T. Ellenbogen, *Near-Infrared Tunable Surface Lattice Induced Transparency in a Plasmonic Metasurface*, Laser Photon. Rev. **14**, 1900204 (2020).
- [77] L. Zhao, K. L. Kelly, and G. C. Schatz, *The Extinction Spectra of Silver Nanoparticle Arrays: Influence of Array Structure on Plasmon Resonance Wavelength and Width †*, J. Phys. Chem. B **107**, 7343 (2003).
- [78] F. J. García de Abajo, *Colloquium: Light Scattering by Particle and Hole Arrays*, Rev. Mod. Phys. **79**, 1267 (2007).
- [79] J. Götte, *Principles of Nano-Optics, 2nd Edn., by Lukas Novotny and Bert Hecht*, Contemp. Phys. **54**, 123 (2013).
- [80] E. Hao, S. Li, R. C. Bailey, S. Zou, G. C. Schatz, and J. T. Hupp, *Optical Properties of Metal Nanoshells*, J. Phys. Chem. B **108**, 1224 (2004).
- [81] S. Keren-Zur, O. Avayu, L. Michaeli, and T. Ellenbogen, *Nonlinear Beam Shaping with Plasmonic Metasurfaces*, ACS Photonics **3**, 117 (2016).
- [82] Lord Rayleigh, *On the Dynamical Theory of Gratings*, Proc. R. Soc. A Math. Phys. Eng. Sci. **79**, 399 (1907).
- [83] B. D. Thackray, V. G. Kravets, F. Schedin, G. Auton, P. A. Thomas, and A. N. Grigorenko, *Narrow Collective Plasmon Resonances in Nanostructure Arrays Observed at Normal Light Incidence for Simplified Sensing in Asymmetric Air and Water Environments*, ACS Photonics **1**, 1116 (2014).
- [84] J. A. Armstrong, N. Bloembergen, J. Ducuing, and P. S. Pershan, *Interactions between Light Waves in a Nonlinear Dielectric*, Phys. Rev. **127**, 1918 (1962).
- [85] O. Avayu, E. Almeida, Y. Prior, and T. Ellenbogen, *Composite Functional Metasurfaces for Multispectral Achromatic Optics*, Nat. Commun. **8**, 14992 (2017).
- [86] A. I. Kuznetsov, A. E. Miroshnichenko, M. L. Brongersma, Y. S. Kivshar, and B. Luk'yanchuk, *Optically Resonant Dielectric Nanostructures*, Science (80-.). **354**, aag2472 (2016).
- [87] A. Arbabi, Y. Horie, M. Bagheri, and A. Faraon, *Dielectric Metasurfaces for Complete Control of Phase and Polarization with Subwavelength Spatial Resolution and High*

- Transmission*, Nat. Nanotechnol. **10**, 937 (2015).
- [88] K. O'Brien, H. Suchowski, J. Rho, A. Salandrino, B. Kante, X. Yin, X. Zhang, K. O'Brien, H. Suchowski, J. Rho, A. Salandrino, B. Kante, X. Yin, X. Zhang, K. O'Brien, H. Suchowski, J. Rho, A. Salandrino, B. Kante, X. Yin, and X. Zhang, *Predicting Nonlinear Properties of Metamaterials from the Linear Response*, Nat. Mater. **14**, 379 (2015).
- [89] C. Ciracì, E. Poutrina, M. Scalora, and D. R. Smith, *Origin of Second-Harmonic Generation Enhancement in Optical Split-Ring Resonators*, Phys. Rev. B **85**, 201403 (2012).
- [90] T. Utikal, T. Zentgraf, T. Paul, C. Rockstuhl, F. Lederer, M. Lippitz, and H. Giessen, *Towards the Origin of the Nonlinear Response in Hybrid Plasmonic Systems*, Phys. Rev. Lett. **106**, 1 (2011).
- [91] E. Almeida, O. Bitton, Y. Prior, Y. Fainman, and V. M. Shalaev, *Nonlinear Metamaterials for Holography*, Nat. Commun. **7**, 12533 (2016).
- [92] F. Walter, G. Li, C. Meier, S. Zhang, and T. Zentgraf, *Ultrathin Nonlinear Metasurface for Optical Image Encoding*, Nano Lett. **17**, 3171 (2017).
- [93] G. Li, L. Wu, K. F. Li, S. Chen, C. Schlickriede, Z. Xu, S. Huang, W. Li, Y. Liu, E. Y. B. Pun, T. Zentgraf, K. W. Cheah, Y. Luo, and S. Zhang, *Nonlinear Metasurface for Simultaneous Control of Spin and Orbital Angular Momentum in Second Harmonic Generation*, Nano Lett. **17**, 7974 (2017).
- [94] J. Lee, M. Tymchenko, C. Argyropoulos, P.-Y. Chen, F. Lu, F. Demmerle, G. Boehm, M.-C. Amann, A. Alù, and M. A. Belkin, *Giant Nonlinear Response from Plasmonic Metasurfaces Coupled to Intersubband Transitions*, Nature **511**, 65 (2014).
- [95] R. W. Boyd, *Nonlinear Optics*, 3rd Editio (Academic Press, 2008).
- [96] M. Scalora, M. a. Vincenti, D. de Ceglia, V. Roppo, M. Centini, N. Akozbek, and M. J. Bloemer, *Second- and Third-Harmonic Generation in Metal-Based Structures*, Phys. Rev. A **82**, 043828 (2010).
- [97] J. Butet and O. J. F. Martin, *Evaluation of the Nonlinear Response of Plasmonic Metasurfaces: Miller's Rule, Nonlinear Effective Susceptibility Method, and Full-Wave Computation*, J. Opt. Soc. Am. B **33**, A8 (2016).
- [98] G. Bachelier, J. Butet, I. Russier-Antoine, C. Jonin, E. Benichou, and P.-F. Brevet, *Origin of Optical Second-Harmonic Generation in Spherical Gold Nanoparticles: Local Surface and Nonlocal Bulk Contributions*, Phys. Rev. B **82**, 235403 (2010).
- [99] J. Butet, S. Dutta-Gupta, and O. J. F. Martin, *Surface Second-Harmonic Generation from Coupled Spherical Plasmonic Nanoparticles: Eigenmode Analysis and Symmetry Properties*, Phys. Rev. B **89**, 245449 (2014).

- [100] S. Linden, F. B. P. Niesler, J. Förstner, Y. Grynko, T. Meier, and M. Wegener, *Collective Effects in Second-Harmonic Generation from Split-Ring-Resonator Arrays*, Phys. Rev. Lett. **109**, 015502 (2012).
- [101] R. Czaplicki, A. Kiviniemi, J. Laukkanen, J. Lehtolahti, M. Kuittinen, and M. Kauranen, *Surface Lattice Resonances in Second-Harmonic Generation from Metasurfaces*, Opt. Lett. **41**, 2684 (2016).
- [102] C. Garrett and F. Robinson, *Miller's Phenomenological Rule for Computing Nonlinear Susceptibilities*, IEEE J. Quantum Electron. **2**, 328 (1966).
- [103] Y. Sheng, Q. Kong, W. Wang, K. Kalinowski, and W. Krolikowski, *Theoretical Investigations of Nonlinear Raman–Nath Diffraction in the Frequency Doubling Process*, J. Phys. B At. Mol. Opt. Phys. **45**, 055401 (2012).
- [104] L. V. Hau, *Optical Information Processing in Bose-Einstein Condensates*, Nature Photonics.
- [105] *Slow Light Now and Then*, (n.d.).
- [106] T. F. Krauss, *Why Do We Need Slow Light?*, Nature Photonics.
- [107] L. Thévenaz, *Slow and Fast Light in Optical Fibres*, Nature Photonics.
- [108] T. Baba, *Slow Light in Photonic Crystals*, Nat. Photonics **2**, 465 (2008).
- [109] J. B. Khurgin, *Slow Light in Various Media: A Tutorial*, Adv. Opt. Photonics **2**, 287 (2010).
- [110] M. Fleischhauer, A. Imamoglu, and J. P. Marangos, *Electromagnetically Induced Transparency: Optics in Coherent Media*, Rev. Mod. Phys. **77**, 633 (2005).
- [111] S. Zhang, D. A. Genov, Y. Wang, M. Liu, and X. Zhang, *Plasmon-Induced Transparency in Metamaterials*, Phys. Rev. Lett. **101**, 047401 (2008).
- [112] N. Papasimakis, V. A. Fedotov, N. I. Zheludev, and S. L. Prosvirnin, *Metamaterial Analog of Electromagnetically Induced Transparency*, Phys. Rev. Lett. **101**, 253903 (2008).
- [113] N. Liu, L. Langguth, T. Weiss, J. Kästel, M. Fleischhauer, T. Pfau, and H. Giessen, *Plasmonic Analogue of Electromagnetically Induced Transparency at the Drude Damping Limit*, Nat. Mater. **8**, 758 (2009).
- [114] S. Weis, R. Rivière, S. Deléglise, E. Gavartin, O. Arcizet, A. Schliesser, and T. J. Kippenberg, *Optomechanically Induced Transparency*, Science (80-.). **330**, (2010).
- [115] M. Karuza, C. Biancofiore, M. Bawaj, C. Molinelli, M. Galassi, R. Natali, P. Tombesi, G. Di Giuseppe, and D. Vitali, *Optomechanically Induced Transparency in a Membrane-in-the-Middle Setup at Room Temperature*, Phys. Rev. A - At. Mol. Opt. Phys. **88**, (2013).
- [116] A. H. Safavi-Naeini, T. P. M. Alegre, J. Chan, M. Eichenfield, M. Winger, Q. Lin, J. T.

- Hill, D. E. Chang, and O. Painter, *Electromagnetically Induced Transparency and Slow Light with Optomechanics*, *Nature* **472**, 69 (2011).
- [117] H. Schmidt, K. L. Campman, A. C. Gossard, and A. Imamoğlu, *Tunneling Induced Transparency: Fano Interference in Intersubband Transitions*, *Appl. Phys. Lett.* **70**, 3455 (1997).
- [118] C. J. Chang-Hasnain, K. U. Pei-Cheng, J. Kim, and S. L. Chuang, *Variable Optical Buffer Using Slow Light in Semiconductor Nanostructures*, in *Proceedings of the IEEE*, Vol. 91 (2003), pp. 1884–1896.
- [119] X. Wang, A. A. Belyanin, S. A. Crooker, D. M. Mittleman, and J. Kono, *Interference-Induced Terahertz Transparency in a Semiconductor Magneto-Plasma*, *Nat. Phys.* **6**, 126 (2010).
- [120] J. Schmit, *INTERFEROMETRY | White Light Interferometry*, in *Encyclopedia of Modern Optics* (Elsevier, 2005), pp. 375–387.
- [121] P. Hariharan, *Basics of Interferometry* (2012).
- [122] P. Hariharan, *Optical Interferometry: Second Edition* (2003).
- [123] L. Lepetit, G. Chériaux, and M. Joffre, *Linear Techniques of Phase Measurement by Femtosecond Spectral Interferometry for Applications in Spectroscopy*, *J. Opt. Soc. Am. B* **12**, 2467 (1995).
- [124] A. Borzsonyi, A. Kovacs, and K. Osvay, *What We Can Learn about Ultrashort Pulses by Linear Optical Methods*, *Appl. Sci.* **3**, 515 (2013).
- [125] B. Barrett, R. Geiger, I. Dutta, M. Meunier, B. Canuel, A. Gauguier, P. Bouyer, and A. Landragin, *The Sagnac Effect: 20 Years of Development in Matter-Wave Interferometry | L'effet Sagnac: 20 Ans de Développements Des Interféromètres à Ondes de Matière*, *Comptes Rendus Phys.* **15**, (2014).
- [126] F. Zernike, *Phase Contrast, a New Method for the Microscopic Observation of Transparent Objects*, *Physica* **9**, 686 (1942).
- [127] R. N. Smartt and W. H. Steel, *Theory and Application of Point-Diffraction Interferometers*, *Jpn. J. Appl. Phys.* **14**, 351 (1975).
- [128] Y. K. Park, C. Depeursinge, and G. Popescu, *Quantitative Phase Imaging in Biomedicine*, *Nature Photonics*.
- [129] D. M. Sullivan, *Electromagnetic Simulation Using the FDTD Method* (2010).
- [130] J. Schneider, *Understanding the Finite-Difference Time-Domain Method*, Artech House Antennas Propag. Libr. **2010**, 1006 (2005).
- [131] X. Q. Sheng and W. Song, *Essentials of Computational Electromagnetics* (2012).
- [132] K. S. Yee, *Numerical Solution of Initial Boundary Value Problems Involving Maxwell's Equations in Isotropic Media*, *IEEE Transactions on Antennas and Propagation*.

- [133] S. Keren-Zur, *Nonlinear Interactions in Plasmonic Metasurfaces*, PhD Thesis, Tel Aviv University, 2019.
- [134] R. W. Wood, *On a Remarkable Case of Uneven Distribution of Light in a Diffraction Grating Spectrum*, *Philos. Mag. Ser. 6* **4**, 396 (1902).
- [135] O. Doron, L. Michaeli, and T. Ellenbogen, *Direct and Cascaded Collective Third-Harmonic Generation in Metasurfaces*, *J. Opt. Soc. Am. B* (2019).
- [136] D. C. Hooper, C. Kuppe, D. Wang, W. Wang, J. Guan, T. W. Odom, and V. K. Valev, *Second Harmonic Spectroscopy of Surface Lattice Resonances*, *Nano Lett.* (2019).
- [137] M. J. Huttunen, P. Rasekh, R. W. Boyd, and K. Dolgaleva, *Using Surface Lattice Resonances to Engineer Nonlinear Optical Processes in Metal Nanoparticle Arrays*, *Phys. Rev. A* (2018).
- [138] S. Chen, B. Reineke, G. Li, T. Zentgraf, and S. Zhang, *Strong Nonlinear Optical Activity Induced by Lattice Surface Modes on Plasmonic Metasurface*, *Nano Lett.* (2019).
- [139] R. Czaplicki, A. Kiviniemi, M. J. Huttunen, X. Zang, T. Stolt, I. Vartiainen, J. Butet, M. Kuittinen, O. J. F. Martin, and M. Kauranen, *Less Is More: Enhancement of Second-Harmonic Generation from Metasurfaces by Reduced Nanoparticle Density*, *Nano Lett.* (2018).
- [140] M. J. Huttunen, O. Reshef, T. Stolt, K. Dolgaleva, R. W. Boyd, and M. Kauranen, *Efficient Nonlinear Metasurfaces Using Multiresonant High-Q Plasmonic Arrays*, in *2019 Conference on Lasers and Electro-Optics Europe and European Quantum Electronics Conference, CLEO/Europe-EQEC 2019*, Vol. Part F143- (OSA - The Optical Society, 2019), pp. E30–E35.
- [141] N. M. Tran, I. A. Chioar, A. Stein, A. Alekhin, V. Juvé, G. Vaudel, I. Razdolski, V. Kapaklis, and V. Temnov, *Observation of the Nonlinear Wood's Anomaly on Periodic Arrays of Nickel Nanodimers*, *Phys. Rev. B* (2018).
- [142] M. J. Huttunen, S. Bin-Alam, O. Reshef, Y. Mamchur, T. Stolt, J. M. Menard, K. Dolgaleva, R. W. Boyd, and M. Kauranen, *Non-Local Field Effects in Nonlinear Plasmonic Metasurfaces*, in *International Conference on Transparent Optical Networks*, Vols. 2020-July (IEEE Computer Society, 2020).
- [143] S. H. Strogatz, *Exploring Complex Networks*, *Nature*.
- [144] A. T. Winfree, *Biological Rhythms and the Behavior of Populations of Coupled Oscillators*, *J. Theor. Biol.* (1967).
- [145] M. C. Cross and P. C. Hohenberg, *Pattern Formation Outside of Equilibrium*, *Rev. Mod. Phys.* (1993).
- [146] M. H. Matheny, J. Emenheiser, W. Fon, A. Chapman, A. Salova, M. Rohden, J. Li, M. H. de Badyn, M. Pósfai, L. Duenas-Osorio, M. Mesbahi, J. P. Crutchfield, M. C. Cross,

- R. M. D'Souza, and M. L. Roukes, *Exotic States in a Simple Network of Nanoelectromechanical Oscillators*, *Science* (80-.). (2019).
- [147] M. J. Panaggio and D. M. Abrams, *Chimera States: Coexistence of Coherence and Incoherence in Networks of Coupled Oscillators*, *Nonlinearity* (2015).
- [148] Y. S. Cho, T. Nishikawa, and A. E. Motter, *Stable Chimeras and Independently Synchronizable Clusters*, *Phys. Rev. Lett.* (2017).
- [149] M. Parto, W. Hayenga, A. Marandi, D. N. Christodoulides, and M. Khajavikhan, *Realizing Spin Hamiltonians in Nanoscale Active Photonic Lattices*, *Nat. Mater.* (2020).
- [150] W. Zhou, M. Dridi, J. Y. Suh, C. H. Kim, D. T. Co, M. R. Wasielewski, G. C. Schatz, and T. W. Odom, *Lasing Action in Strongly Coupled Plasmonic Nanocavity Arrays*, *Nat. Nanotechnol.* **8**, 506 (2013).
- [151] A. Yang, T. B. Hoang, M. Dridi, C. Deeb, M. H. Mikkelsen, G. C. Schatz, and T. W. Odom, *Real-Time Tunable Lasing from Plasmonic Nanocavity Arrays*, *Nat. Commun.* (2015).
- [152] T. K. Hakala, H. T. Rekola, A. I. Väkeväinen, J.-P. Martikainen, M. Nečada, A. J. Moilanen, and P. Törmä, *Lasing in Dark and Bright Modes of a Finite-Sized Plasmonic Lattice*, *Nat. Commun.* **8**, 13687 (2017).
- [153] D. Wang, A. Yang, W. Wang, Y. Hua, R. D. Schaller, G. C. Schatz, and T. W. Odom, *Band-Edge Engineering for Controlled Multi-Modal Nanolasing in Plasmonic Superlattices*, *Nat. Nanotechnol.* (2017).
- [154] R. R. Gutha, S. M. Sadeghi, C. Sharp, and W. J. Wing, *Biological Sensing Using Hybridization Phase of Plasmonic Resonances with Photonic Lattice Modes in Arrays of Gold Nanoantennas*, *Nanotechnology* (2017).
- [155] A. A. Yanik, A. E. Cetin, M. Huang, A. Artar, S. H. Mousavi, A. Khanikaev, J. H. Connor, G. Shvets, and H. Altug, *Seeing Protein Monolayers with Naked Eye through Plasmonic Fano Resonances*, *Proc. Natl. Acad. Sci. U. S. A.* (2011).
- [156] K.-H. Chang, J.-S. Cheng, T.-W. Lu, and P.-T. Lee, *Engineering Surface Lattice Resonance of Elliptical Gold Nanodisk Array for Enhanced Strain Sensing*, *Opt. Express* (2018).
- [157] S. V. Zhukovsky, V. E. Babicheva, A. V. Uskov, I. E. Protsenko, and A. V. Lavrinenko, *Enhanced Electron Photoemission by Collective Lattice Resonances in Plasmonic Nanoparticle-Array Photodetectors and Solar Cells*, *Plasmonics* (2014).
- [158] S. V. Zhukovsky, V. E. Babicheva, A. V. Uskov, I. E. Protsenko, and A. V. Lavrinenko, *Electron Photoemission in Plasmonic Nanoparticle Arrays: Analysis of Collective Resonances and Embedding Effects*, *Appl. Phys. A Mater. Sci. Process.* (2014).
- [159] B. D. Thackray, P. A. Thomas, G. H. Auton, F. J. Rodriguez, O. P. Marshall, V. G.

- Kravets, and A. N. Grigorenko, *Super-Narrow, Extremely High Quality Collective Plasmon Resonances at Telecom Wavelengths and Their Application in a Hybrid Graphene-Plasmonic Modulator*, Nano Lett. (2015).
- [160] K. Nogajewski, J. Usakowski, W. Knap, V. V. Popov, F. Teppe, S. L. Rumyantsev, and M. S. Shur, *Localized and Collective Magnetoplasmon Excitations in AlGaIn/GaN-Based Grating-Gate Terahertz Modulators*, Appl. Phys. Lett. **99**, 213501 (2011).
- [161] J. H. Yang, V. E. Babicheva, M. W. Yu, T. C. Lu, T. R. Lin, and K. P. Chen, *Structural Colors Enabled by Lattice Resonance on Silicon Nitride Metasurfaces*, ACS Nano (2020).
- [162] J. Jang, T. Badloe, Y. Yang, T. Lee, J. Mun, and J. Rho, *Spectral Modulation through the Hybridization of Mie-Scatterers and Quasi-Guided Mode Resonances: Realizing Full and Gradients of Structural Color*, ACS Nano (2020).
- [163] T. Xu, E. C. Walter, A. Agrawal, C. Bohn, J. Velmurugan, W. Zhu, H. J. Lezec, and A. A. Talin, *High-Contrast and Fast Electrochromic Switching Enabled by Plasmonics*, Nat. Commun. (2016).
- [164] Z. Liang, J. Sun, Y. Jiang, L. Jiang, and X. Chen, *Plasmonic Enhanced Optoelectronic Devices*, Plasmonics.
- [165] M. Gu, Q. Zhang, and S. Lamon, *Nanomaterials for Optical Data Storage*, Nature Reviews Materials.
- [166] K. Wu, C. Soci, P. P. Shum, and N. I. Zheludev, *Computing Matrix Inversion with Optical Networks*, Opt. Express (2014).
- [167] R. Kolkowski and A. Femius Koenderink, *Lattice Resonances in Optical Metasurfaces with Gain and Loss*, Proc. IEEE (2020).
- [168] I. Sersic, C. Tuambilangana, T. Kampfrath, and A. F. Koenderink, *Magnetolectric Point Scattering Theory for Metamaterial Scatterers*, Phys. Rev. B - Condens. Matter Mater. Phys. (2011).

תקציר

במהלך העשורים האחרונים התחוללה התקדמות אדירה ביכולת שלנו לשלוט ולעצב אור באמצעות חומרים מלאכותיים דו-ממדיים, המכונים מטא-משטחים. החומרים האלו לרוב בנויים ממערכים של חלקיקים מתכתיים או דיאלקטרים, הקטנים מאורך הגל של האור. באמצעות תכנון שקול של צורת החלקיקים, החומר ממנו הם עשויים ומיקומם במערך, ניתן להשיג שליטה מקומית במשרעת, מופע וקיטוב האור. לכן, מטא-משטחים מאפשרים מזעור של רכיבים אופטיים קיימים ואף מימוש של יישומים חדשים. בנוסף, מידת החופש הגדולה בעיצוב התגובה האופטית של החלקיקים, מאפשרת לבצע מחקר מקיף על מגוון רחב של תופעות פיזיקליות.

התגובה האופטית של מטא-משטחים נקבעת על פי התגובה של כל אחד מהחלקיקים המרכיבים את המערך, בנוסף להידודים ביניהם. בשנים האחרונות, מחקרים הראו שהידודים קוהרנטיים כוללניים של החלקיקים במערך יכולים לשחק תפקיד חשוב בקביעת התגובה האופטית של המערך כולו. הדבר גורם לתופעות פיזיקליות רבות ומעניינות עם פוטנציאל יישומי גבוה.

בתזה זו, אנו חוקרים הן באופן תיאורטי והן באופן ניסיוני היבטים בסיסיים של ההידודים הקוהרנטיים הכוללניים במערכים של ננו-חלקיקים מתכתיים. ספציפית, אנו מתמקדים בשלושה היבטים חדשניים של הידודים אלו: 1. הרחבה לתחום הלא-לינארי. 2. שליטה זמנית ותופעות של אור איטי. 3. האפיון רחב הסרט של המשרעת והמופע הקשורים בתופעות אלו.

אנו מתחילים בהקדמה נרחבת בפרק 1, אשר משמשת כבסיס למחקר המקורי המוצג בתזה זו. ההקדמה מציגה את הנושאים של מטא-משטחים לינאריים (חלק 1.1) ולא-לינאריים (חלק 1.2), תופעות של אור איטי (חלק 1.3), אינטרפרומטריה ספקטרלית (חלק 1.4), והשיטות הניסיוניות, נומריות ושיטות הייצור בהן נעשה שימוש עבור המחקר המוצג (חלק 1.5). בפרק Chapter 2, חלק הארי של תזה זו, אנו מציגים שלושה מאמרים שפורסמו בכתבי עת מדעיים. כל אחד מהמאמרים מתמקד בתופעות שונות הנובעות מהאינטראקציה הכוללנית של החלקיקים. תחילה, בחלק 2.1, אנו מציגים מחקר של ההידודים הכוללניים במערכים של ננו-חלקיקים, בתחום הלא-לינארי. אנו מדגימים תנאי תהודה חדש להגברת האפקטים הלא-לינאריים, אשר נובע מצימוד של מצבים מקומיים ומצבים ממושטים על גבי המערך. מקורם של המצבים המקומיים הוא בתנודות קוהרנטיות של האלקטרונים בכל חלקיק, הידועות כפלזמונים, בעוד המצבים הממושטים קשורים בגלים משטחיים הנתמכים על ידי פיזור אור קוהרנטי. יתר על כן, אנו מציגים טיפול תיאורטי המאפשר לתאר את השפעת ההידודים של החלקיקים על התגובה הלא-לינארית של מערכים באופן כללי, ובפרט מאפשר לחזות ולנתח את התופעות המודגמות ניסיונית. בהמשך, בחלק 2.2 של התזה, אנו מראים כיצד פיזור אור קוהרנטי במערכים של חלקיקים יכול להשרות שקיפות ברת כיוונון ואזורים בספקטרום בעלי תכונות של אור איטי. לבסוף, בחלק 2.3, אנו מציגים שיטת אפיון מקורית המאפשרת לקבוע באופן מדויק וכתלות בזמן את המופע לאורך הספקטרום, של אור המוחזר או מועבר מדגמים מיקרוסקופיים. השיטה מאפשרת תנאי הארה גמישים, ולכן מתאימה במיוחד לאפיון של מטא-משטחים אשר תומכים בתופעות קוהרנטיות כוללניות. הממצאים והפיתוחים המובאים בתזה זו יכולים לאפשר שימושים חדשים בתחום של ננו-פוטוניקה ולתרום רבות ליישומים כגון לייזרים, מאפננים, מסכים, תקשורת אופטית ואף לעיבוד אותות המבוסס על פוטונים.

עבודה זו נעשתה בהדרכת
פרופ' טל אלנבוגן ופרופ' חיים סוכובסקי



School of Physics and Astronomy בית הספר לפיזיקה ולאסטרונומיה
The Raymond and Beverly Sackler הפקולטה למדעים מדויקים
Faculty of Exact Sciences ע"ש ריימונד ובברלי סאקלר
Tel Aviv University אוניברסיטת תל אביב

חיבור לשם קבלת התואר "דוקטור לפילוסופיה"

אינטראקציה קוהרנטית קולקטיבית לינארית ולא-לינארית במערכים של ננו-חלקיקים פלזמוניים

הוגש לסנאט של אוניברסיטת תל-אביב

ליאור מיכאלי

עבודה זו נעשתה בהדרכת

פרופ' טל אלנבוגן ופרופ' חיים סוכובסקי

טבת תשפ"א, ינואר 2021